EXPERIMENTAL INVESTIGATION OF TURBULENT WAKE STRUCTURES AND DYNAMIC COUPLING OF TANDEM LIFTING BODIES IN A HYDRODYNAMIC CHANNEL

by

Samuel Elliott Hellman

A dissertation submitted to the faculty of
The University of North Carolina at Charlotte
in partial fulfillment of the requirements
for the degree of Doctor of Philosophy in
Mechanical Engineering

Charlotte

2012

Approved by:

Dr. Peter Tkacik

Dr. Mesbah Uddin

Dr. Scott Kelly

Dr. Yuri Godin

Dr. Lynn Ahlgrim-Delzell

© 2012
Samuel Elliott Hellman
ALL RIGHTS RESERVED

ABSTRACT

SAMUEL ELLIOTT HELLMAN. Experimental investigation of turbulent wake
structures and dynamic coupling of tandem lifting bodies in a hydrodynamic
channel. (Under the direction of DR. PETER TKACIK)

Two experimental studies are carried out on interacting tandem bodies in incompressible, turbulent flow and the design of a hydrodynamic water channel in which the studies are conducted is discussed. The water channel has a 1 m^2 test section, and a flow velocity up to 1 m/s. The constant cross-section design consists of a recirculating channel in a horizontal plane and a submerged blade pump (propeller) similar to the design of a wind tunnel which allows much lower power consumption than typical water channel design.

The first study examined is the dynamic coupling between oscillating hydrofoils in uniform, flow. Experiments are carried out on a single, finite-span, oscillating foil, as well two and three oscillating foils in tandem. Wake modes and structures of a single oscillating foil are described and found to agree well with results from previous infinite-span foil studies. The interaction between oscillating foils is described qualitatively and it is found that the response of the downstream foils is directly related to the wake modes of the upstream foil. Furthermore, it is found that low-order, locally-linear models can approximate the coupling between two and three foils and these models should hold for a large, multi-agent system or flock of such interacting bodies.

The second is a case study examining the performance and safety of aerodynamic downforce devices employed on NASCAR's Car of Tomorrow (COT) racecar. The wake interactions of a deck-mounted wing is compared to that of a spoiler and the role these interactions play in flipping and aerodynamic performance is examined using 10% scale models and particle image velocimetry to educe flow topology. It is found that the smaller time and length scale of structures in the wake of a winged car should yield more predictable handling characteristics for closely following vehicles during typical race conditions. It is also shown that, under extreme yaw (180°), the winged car may be more likely to create lift due to reattached flow failing to deploy roof flaps (aerodynamic safety devices) consistently.

ACKNOWLEDGMENTS

I would like to thank all of the people who helped make this dissertation possible. First, I wish to thank my advisor, Dr. Peter Tkacik for all his guidance, encouragement, support, and patience. Also, I would like to thank my committee members Dr. Scott Kelly, Dr. Mesbah Uddin, and Dr. Yuri Godin for their very helpful input, comments and suggestions as well as Dr. Stuart Smith for his insightful conversations. Additionally, I would like to acknowledge all of those people who provided support and assistance with constructing and setting up the water channel; Luke Woroniecki, Aaron Rineheimer, William Kerlin, and Michael D'Elia.

A special thanks to Mike Clem at Clemsoft for providing a servo motor and programming for the hydrofoil experiment.

I gratefully acknowledge the funding sources that made my PhD work possible. I have been supported by the Graduate Assistant Support Plan for my entire time as a PhD stdent. My first year I was given a teaching assistanship by the Mechanical Engineering and Engineering Science Department while the National Science Foundation has supported me for the last three years.

Lastly, I would like to thank my family for all their love and encouragement. For my parents who supported me in all my pursuits. For the presence of my brother David here in Charlotte for the last year. And most of all for my loving, supportive, encouraging, and patient wife Christine whose faithful support during the final stages of this PhD is so appreciated. Thank you.

TABLE OF CONTENTS

LIST OF TABLES ix
LIST OF FIGURES x
LIST OF SYMBOLS xiii
CHAPTER 1: INTRODUCTION 1
CHAPTER 2: HYDRODYNAMIC WATER CHANNEL 3
  2.1 Background 3
    2.1.1 Channel Operation 3
  2.2 Channel Layout 6
    2.2.1 Pump 7
    2.2.2 Test Section 10
    2.2.3 Channel 14
    2.2.4 Turning Vanes 15
    2.2.5 Flow Straightening 17
    2.2.6 Nozzle 18
  2.3 Summary 20
CHAPTER 3: DYNAMIC COUPLING OF OSCILLATING FOILS IN TANDEM 21
  3.1 Background 21
    3.1.1 Drag and Thrust of Oscillating Foils 23
    3.1.2 Wake Structures of Oscillating Foils 24
    3.1.3 Oscillating Bodies in Tandem 28
  3.2 Experimental Setup and Parameters 31
    3.2.1 Angular Position Control 32
    3.2.2 Angular Position Measurement and Spectral Analysis 34
    3.2.3 Parameter Domain 35
    3.2.4 Wake Visualization 36

3.3 Wake Modes and Transitions 39

3.3.1 Wakes at Low Amplitude 39

3.3.2 Wakes at High Amplitude 42

3.3.3 Reynolds Number Effects 45

3.4 Frequency Response Models 47

3.4.1 Requirements for System Linearity 47

3.4.2 System Response 48

3.4.3 FRF Approximation 55

3.4.4 Model Fitting using MATLAB's Robust Control Toolbox 62

3.5 Three Foil System 64

3.6 Summary 67

3.6.1 Future Work 69

CHAPTER 4: NASCAR COT CASE STUDY 70

4.1 Background 70

4.2 Experimental Methods 74

4.2.1 Reynolds Number Dependence of Wake Structure 78

4.3 Zero Yaw 79

4.4 Extreme Yaw 83

4.4.1 Roof-Flap Interaction with Wake at Extreme Yaw 83

4.4.2 Flow Characterization and Reynolds Number Scaling 85

4.5 Summary 91

REFERENCES 92

APPENDIX A: FREQUENCY RESPONSE DATA 101

A.1 Frequency Response Magnitude 101

A.2 Frequency Response Phase Shift 106

APPENDIX B: PROGRAMS AND CODE 111

B.1 LabView Data Aquisition Program Block 111

B.2 Unwrap Function for Periodic Data 117
B.3 Frequency Response Function Code 118
B.4 Frequency Response Function Fitting Code 118

LIST OF TABLES

TABLE 3.1: PID Control Parameters 34

TABLE 3.2: Velocity and Reynolds numbers tested for oscillating foils 35

TABLE 3.3: Frequency and amplitude input parameters 36

TABLE 4.1: Reynolds Number Values for COT 74

LIST OF FIGURES

FIGURE 2.1: Recirculating water channel schematic. 5

FIGURE 2.2: Commercially available Rolling Hills model 1520[1]. 7

FIGURE 2.3: Recirculating water channel rendering. Flow is counterclockwise. 8

FIGURE 2.4: Submerged recirculation pump for water channe. 9

FIGURE 2.5: Test frame for a rolling-road-surface setup. 11

FIGURE 2.6: Test frame for race car drafting study. 12

FIGURE 2.7: Test frame for robotic fish. 12

FIGURE 2.8: Actual test frame used in flow visualization experiment. 13

FIGURE 2.9: Car mounted (upside down) from above using slotted tracks. 13

FIGURE 2.10: Towing experiment for a torpedo using a servo drive. 14

FIGURE 2.11: Flow over a) protruding lip b) smooth panel joint. 16

FIGURE 2.12: View of turning vanes entering the nozzle section of the channel. 17

FIGURE 2.13: PVC flow straightener immediately downstream of pump. 18

FIGURE 2.14: Nozzle and stainless steel honeycomb flow straightener. 19

FIGURE 2.15: Closeup view stainless steel honeycomb flow straightener. 19

FIGURE 3.1: Selected wake modes of oscillating foils. 25

FIGURE 3.2: Phase diagram of wake modes. 27

FIGURE 3.3: Schematic of experimental layout. 31

FIGURE 3.4: Laboratory realization of foil experiment. 32

FIGURE 3.5: Supports used to cantilever foils into water channel. 33

FIGURE 3.6: Range of reduced frequencys and normalized amplitudes tested. 37

FIGURE 3.7: BvK street seen behind static foil. 40

FIGURE 3.8: Wake transitions as a function of frequency for low amplitudes. 41

FIGURE 3.9: 2C wake. 42

FIGURE 3.10: 2P wake 42

FIGURE 3.11: Wake Transitions as function of frequency for high amplitudes. 43

FIGURE 3.12: Flow separation wake. 44

FIGURE 3.13: 2P + 2S hybrid wake. 44

FIGURE 3.14: Reynolds number independence of wake topology. 46

FIGURE 3.15: Frequency response for system linearity system. 50

FIGURE 3.16: Frequency response for system discretely linear system. 51

FIGURE 3.17: 2P wake coupling. 52

FIGURE 3.18: 2S wake coupling. 52

FIGURE 3.19: Sytem attenuation as a function of reduced frequency. 56

FIGURE 3.20: Schematic of foil system model for FRF approximation. 57

FIGURE 3.21: Absolute phase shift and phase delay for a system. 61

FIGURE 3.22: Linear approximation of system using physical FRF model. 63

FIGURE 3.23: Transfer functions obtained using MATLAB's `fitfrd` command. 64

FIGURE 3.24: Schematic of three-foil experimental layout. 64

FIGURE 3.25: System response with and without a middle foil present. 66

FIGURE 4.1: Illustration of roof flap function. 71

FIGURE 4.2: COT fitted with a spoiler and wing. 72

FIGURE 4.3: 10% scale models of COT with wing and spoiler. 75

FIGURE 4.4: Schematic of 2-D PIV experimental setup. Not to scale. 77

FIGURE 4.5: Streamlines showing mean flow past SC and WC at zero yaw. 80

FIGURE 4.6: Velocity maps of wake region for SC and WC at zero yaw. 80

FIGURE 4.7: Instantaneous velocity field in wake of SC and WC at zero yaw. 82

FIGURE 4.8: Gallilean filtered field in wake of SC and WC at zero yaw. 82

FIGURE 4.9: Streamwise velocity profiles for SC and WC at 180° yaw. 84

FIGURE 4.10: Velocity maps for SC and WC at 180° yaw. 85

FIGURE 4.11: Instantaneous velocity maps for SC and WC at 180° yaw. 86

FIGURE 4.12: Streamlines showing mean flow past SC at 180° yaw. 87

FIGURE 4.13: Streamlines showing mean flow past WC at 180° yaw. 88

FIGURE 4.14: Local Reynolds number scales for flow modes at extreme yaw. 90

FIGURE A.1: Frequency response in dB for all x/c at u=0.30m/s. 102

FIGURE A.2: Frequency response in dB for all x/c at u=0.40m/s. 103

FIGURE A.3: Frequency response in dB for all x/c at u=0.50m/s. 104

FIGURE A.4: Frequency response in dB for all x/c at u=0.60m/s. 105

FIGURE A.5: Absolute phase shift in degrees for all x/c at u=0.30m/s. 107

FIGURE A.6: Absolute phase shift in degrees for all x/c at u=0.40m/s. 108

FIGURE A.7: Absolute phase shift in degrees for all x/c at u=0.50m/s. 109

FIGURE A.8: Absolute phase shift in degrees for all x/c at u=0.60m/s. 110

FIGURE B.1: Block diagram used to acquire encoder data. 111

FIGURE B.2: Detailed view from block diagram in Figure B.1. 112

FIGURE B.3: Detailed view from block diagram in Figure B.1. 113

FIGURE B.4: Detailed view from block diagram in Figure B.1. 114

FIGURE B.5: Detailed view from block diagram in Figure B.1. 115

FIGURE B.6: Detailed view from block diagram in Figure B.1. 116

FIGURE B.7: Detailed view from block diagram in Figure B.1. 117

List of Symbols

U_∞	Mean Streamwise Flow Velocity
Re	Reynolds Number
Re_h	Vehicle Height Reynolds Number
Re_w	Wheelbase Reynolds Number
Re_L	Length Reynolds Number
Re_c	Chord Reynolds Number
Re_d	Width (Diameter) Reynolds Number
D_L	Local Length Scale
U_L	Local Velocity Scale
c	Chord
s	Span
A_R	Aspect Ratio
x	Foil Spacing
d	Foil Width
f	Frequency of Oscillation (Hz)
ω	Angular Frequency of Oscialltion (rad/s)
ω_n	Natural Frequency of Oscialltion (rad/s)
ω_d	Damped Natural Frequency of Oscialltion (rad/s)
θ	Incidence Angle of Forced Foil
θ_2	Incidence Angle of Passive Foil (Foil 2)
A	Amplitude of Pitching Forced Foil
A_2	Amplitude of Pitching Passive Foil (Foil 2)
A_3	Amplitude of Pitching Passive Foil (Foil 3)
A_D	Normalized Amplitude
St_D	Reduced Frequency
St_A	Amplitude-Based Strouhal Number

ϕ	Phase Shift
m	Mass
C	Damping Coefficient
k	Spring Rate
F_v	Vorticity-Mediated Force acting on Foil
G	Constitutive Force-Displacement Function
UW	Undulating Wake
BvK	Bérnard-von-Kármán Street

CHAPTER 1: INTRODUCTION

The study of tandem bodies in fluid dynamics is both complex and far-reaching and a great number of applications require a body to operate within the influence of another's wake. Some examples include: (a) an airplane taking off and landing in another aircraft's turbulent wake[2], (b) flocking, schooling, and swarming of birds, fish, and insects[3], (c) drafting of racecars[4], (d) insect wing interaction[5], (e) interaction of multiple sails on a boat[6], and (f) groups of wind turbines in close proximity[7]. The stability, controllability, and efficiency of interacting bodies can differ quite drastically from the behavior of the individual members of such a group acting in isolation.

This dissertation experimentally examines two specific cases of wake-structure interaction between bodies and discusses the design of a hydrodynamic water channel used to carry out the studies. It is organized in three chapters with the background and relevent framework for each topic given at the begining of the chapter.

Chapter 2 describes the design of a hydrodynamic water channel which is used for the experiments described in the subsequent chapters. The water channel is one of the largest in the United States (by flow rate) with a 1 m^2 cross section, and a test velocity up to 1 m/s. The constant cross-section design consists of a recirculating channel in a horizontal plane and a submerged blade pump (propeller) similar to the design of a wind tunnel. This design approach allows the pump to maintain maximum test velocity using apporoximately $1kW$ of power; this is much lower than the $\sim 50kW$ which would be required employing standard water channel design consisting of a piped, vertical-plane circulation layout. Multiple options are incorporated for mounting test bodies and measurement equipment, and the glass panels surrounding the sides and bottom of the test section allow optical measurements and visualzation studies.

Chapter 3 describes a fundamental case of oscillating foils in tandem. The flocking, schooling and swarming of large, multiagent systems is a topic of great importance, and the understanding of such systems must start with a description of the coupled dynamics between adjacent members. Here, the simplest configuration is considered; consisting of oscillating hydrofoils in tandem which are subject to a uniform flow. An experiment is carried out on a single, finite-span, oscillating foil, as well two and three oscillating foils in tandem. The various wake modes and structures of a single oscillating foil as well as the interaction between oscillating foils is described qualitatively. Furthermore, low-order, locally-linear models are explored which approximate the dynamic coupling between two and three foils.

Chapter 4 is a case study examining the performance and safety of aerodynamic downforce devices employed on NASCAR's Car of Tomorrow (COT) racecar. Two types of wake interactions are explored in this chapter. The first involves the study of wake structures relevant to drafting of race cars under normal racing conditions. Here the focus is on the difference in wake topology between a COT with a wing and a COT with a spoiler (details in chapter). The second interaction occurs when the vehicle is under extreme yaw (near 180°) as it might be during a crash. Under these circumstances, the interaction of the wing/spoiler with roof flaps (aerodynamic safety devices located on the roof of the car) is examined and a particular tendency for the winged car to flip is explored.

CHAPTER 2: HYDRODYNAMIC WATER CHANNEL

2.1 Background

In order to serve a need for aero and fluid dynamics research, a test facility was designed and constructed in the North Caroloina Motorsports and Automotive Research Center on the campus of the University of North Carolina at Charlotte (UNCC). This facility is a recirculating water channel with a one meter square test section that is three meters long and has a maximum flux of one cubic meter per second; allowing a useable Reynolds number up to 10^6(based on a characteristic length of 1 meter). While the impetus for building this facility was the study of tandem lifting bodies described in Chapters 3 and 4, the expense and time required to build it necessitated a robust design capable of efficiently accomodating many different types of experiments.

When compared to wind tunnels, water channels can provide better qualitative flow analysis. Enhanced visualization allows deeper understanding of phenomena such as vortices, eddies, wakes, separation, and dissipation. This facility is used in a variety of research projects including the study of schooling interactions of robotic fish, the drafting behavior of NASCAR racing vehicles, oscillating energy-generating wings and even vortex-induced-vibration energy. The focus of this chapter is on the design and construction details that provide the required high flow rate, minimal turbulence, boundary layers, velocity gradients, and features that add versatility to the function of the channel.

2.1.1 Channel Operation

The recirculating water channel is an open channel design of relatively constant cross-section with all water flowing on the same horizontal plane. The frame is constructed from A-36 steel and the panels which line the channel are either powder coated steel (soon to be replaced with stainless steel) or fully tempered glass. A diagram is shown in Figure 2.1 and a rendering is shown in Figure 2.3. Water flow from the submerged pump travels first through a PVC pipe flow straightener, through two sets of turning vanes and through a honeycomb flow straightener. Water exiting the flow honeycomb straightener then passes through a nozzle and into the test section. The water completes the circuit through two more sets of turning vanes and returns to the pump.

The channels constant cross-section and submerged pump layout yield high efficiency while the flow straightener, nozzle, and smooth wall/floor panels help provide laminar flow, flat velocity profiles and low turbulence intensity. The channel is capable of exceeding the $1m/s$ target flow velocity and is fully adjustable down to $0.1m/s$. Design features such as universal test frame mounts and slotted tracks/rails above the test section allow a variety of experimental setups without modification and refilling of the channel. Considering that the channel holds 28,800 Liters of water, not only does this save time but also reduces the consumption of water.

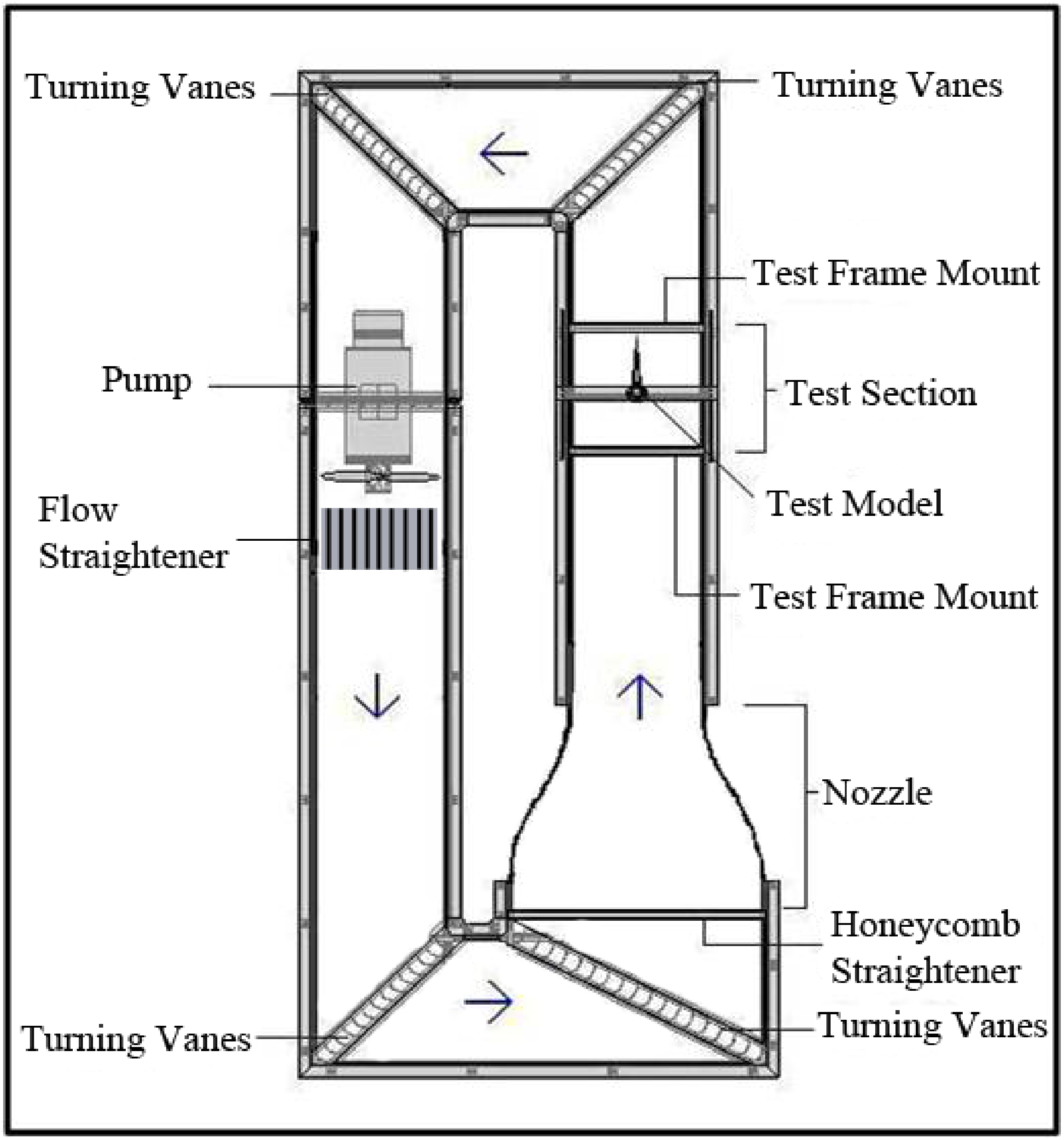

Figure 2.1: Recirculating water channel schematic.

2.2 Channel Layout

In the initial design of the channel, two layouts were considered: 1) ducted layout using a centrifugal pump and 2) constant cross-section (CCS) layout using a submerged pump. The CCS layout was ultimately chosen for the water channel for flow efficiency reasons. Subsequent design elements were based on this decision.

The less efficient ducted layout is more commonly used in water channel design both in commercial and independent applications. A typical example of this layout is shown in Figure 2.2. In this type of channel, water flows through the test section and is discharged into a pipe which directs water underneath the main channel and into a centrifugal pump. The water is pumped back to the main channel via pipe.

Alternatively, the CCS layout uses a channel of relatively constant area rather than flowing through pipes. Our channel, shown in Figure 2.1 and Figure 2.3, is an example of CCS design. This type of layout is commonly used in wind tunnel design but is not typically seen for water channel applications. This is presumably due to the extra weight and size when compared to ducted layouts as well as the common availability of centrifugal pumps. The CCS layout weighs almost twice as much as a ducted design and can require twice as much floor space when oriented horizontally (i.e. all water flow is on the same horizontal plane). Although the CCS layout significantly increases size and weight, it is a much more efficient and less costly design.

Using conservation of energy and mass equations, and assuming steady-state conditions, and appropriate friction and pressure loss coefficients for each layout[8], head-loss and power consumption were estimated for both designs. It was calculated that a ducted layout would create a head-loss of $5.45m$ and require $53kW$ to maintain flow. The CCS layout, on the other hand, creates a head-loss of approximately $0.1m$ and requires only $1kW$. This large disparity is due to the increased velocity in the pipe sections of the ducted layout. To maintain constant flow, conservation of mass

Figure 2.2: Commercially available Rolling Hills model 1520[1].

dictates increased velocity for the pipes due to their smaller cross-sectional area. Because pressure loss is a function of the velocity squared, the ducted layout yields much higher head-loss and therefore power consumption, than does the CCS layout. The energy savings are significant when conducting long experiments and the lower power requirement makes facility preparation easier.

2.2.1 Pump

To facilitate the CCS layout, a submerged recirculation pump (SRP) (shown in Figure 2.4) is required. This type of pump is analogous to the fan in a wind tunnel. As opposed to a centrifugal pump which has a housing through which water flows, the SRP is located in the channel's streamline and water flows around it. Figure 2.3 shows the water channel with the SRP on the left side. This type of pump is most commonly used in European municipal wastewater systems to pump water from one reservoir to another and is designed for high-flow/low-head applications. The water channel uses an ABS model RCP 800 pump capable of flowing 65,000 liters/minute at $0.3m$ head[9]. It is supported by a frame which is isolated from the channel's main frame by a thick rubber mount to reduce vibration and resonance.

Figure 2.3: Recirculating water channel rendering. Flow is counterclockwise.

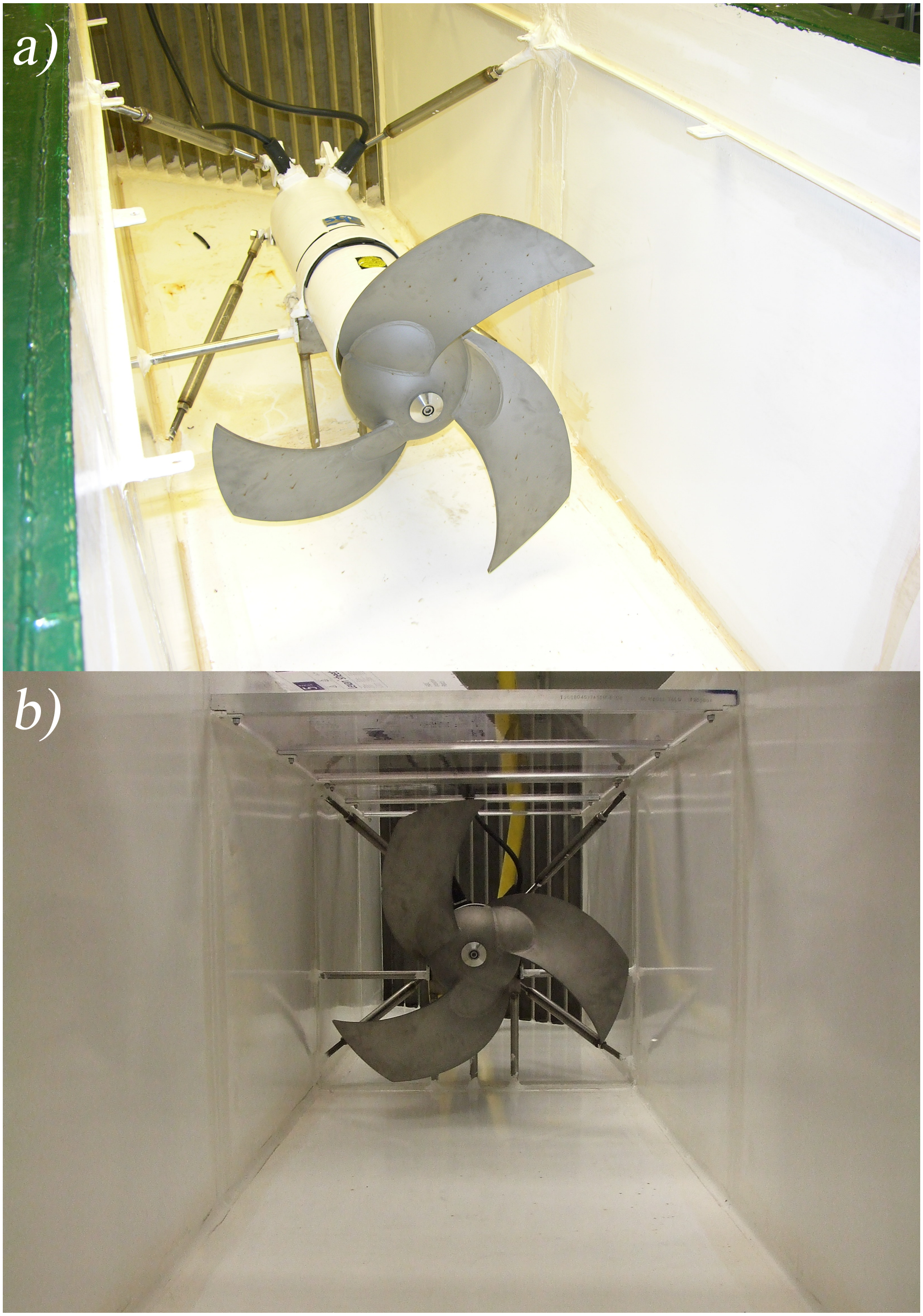

Figure 2.4: a) View of pump and mount from above. b) View of pump from downstream.

The SRP has several crucial advantages over a centrifugal pump. The primary advantage is the ability to use the CCS layout. A centrifugal pump requires piping at the inlet and outlet while the SRP sits directly in the channel. The SRP also adds work to the system in-line with the flow which generates less head-loss than a centrifugal pump that changes the direction of water flow through many degrees of rotation in a relatively narrow housing. Another advantage is that the SRP allows the water to flow out of the pump at the same velocity as it has coming in and with minimal pressure rise. The increased efficiency of the SRP over a centrifugal pump minimizes heat entering the system. Added heat can cause the water temperature to fluctuate, making fluid calculations from experimental data more cumbersome.

Other advantages are size and weight. Because the centrifugal pump's housing must contain the motor and propeller along with the water flow, it requires a massive amount of metal. The SRP only houses a motor while the propeller and water are external. As a result, the SRP weighs $295kg$[9] while a centrifugal pump capable of this flux can weigh up to $10,000kg$. The final (and non-trivial) advantage is cost. For this application, the SRP cost is around $30,000 US, while a centrifugal pump would cost in excess of $150,000 US.

The pump operates on 3-phase, $460V$ power and is controlled by a variable frequency drive. This allows for gradual acceleration and variable velocity for the water.

2.2.2 Test Section

The test section is located downstream of the nozzle and designed to be used for a variety of different experiments accommodating many types of test bodies. As a result, a single mount could not be used as in the case of a wind tunnel designed solely for automobiles or a water channel designed for testing hydrofoils. To allow this flexibility, two features are employed in the recirculating water chanel: 1) Universal test frame mounts and 2) Slotted tracks and/or t-rails at the top of the channel.

The universal test frame mounts consist of two recessed grooves $1m$ apart which

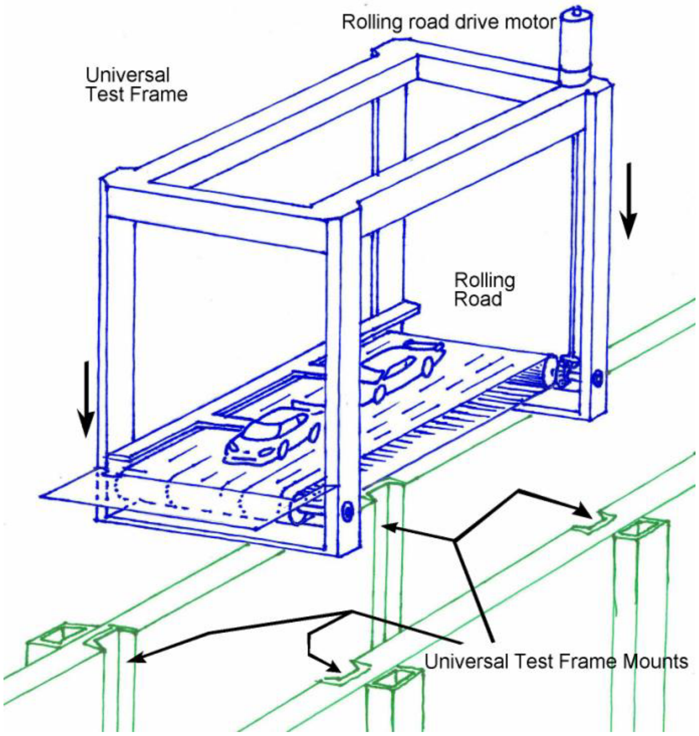

Figure 2.5: Test frame for a rolling-road-surface setup.

are 2.5cm deep and 7.5cm wide. Each groove runs down one side, across the bottom, and up the other side of the channel. This allows different frames to be constructed which simply slide down into the mounts. Examples are shown in Figures 2.5–2.8. The frame mounts make it easy to install almost any body or test apparatus that will fit in the test section without modifying the channel itself. Frames can be built to suit new applications, and existing frames will be saved for future use. The ultimate goal is to have a collection of useful frames which can be quickly swapped and easily adapted to any experiment. If a test frame is not being used, stainless steel blanks can be inserted into the mounts making the test section walls smooth. These blanks also have several threaded holes which can be used for attachment or can be filled with plugs when not in use.

The slotted tracks at the top of the channel allow further mounting options and can be used by themselves or in conjunction with the frame mounts. They can be used to suspend a test body from above (Figure 2.9) or to attach instrumentation

Figure 2.6: Test frame for race car drafting study.

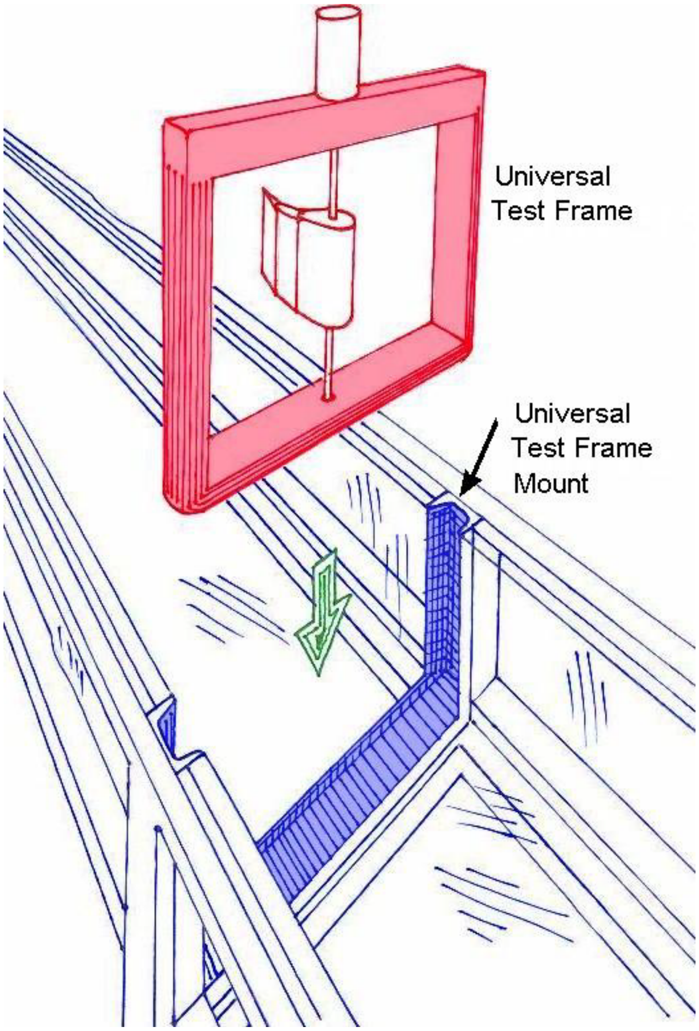

Figure 2.7: Test frame for robotic fish.

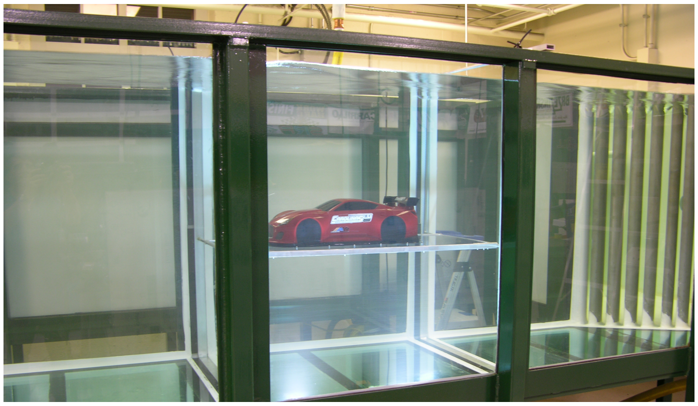

Figure 2.8: Actual test frame used in flow visualization experiment.

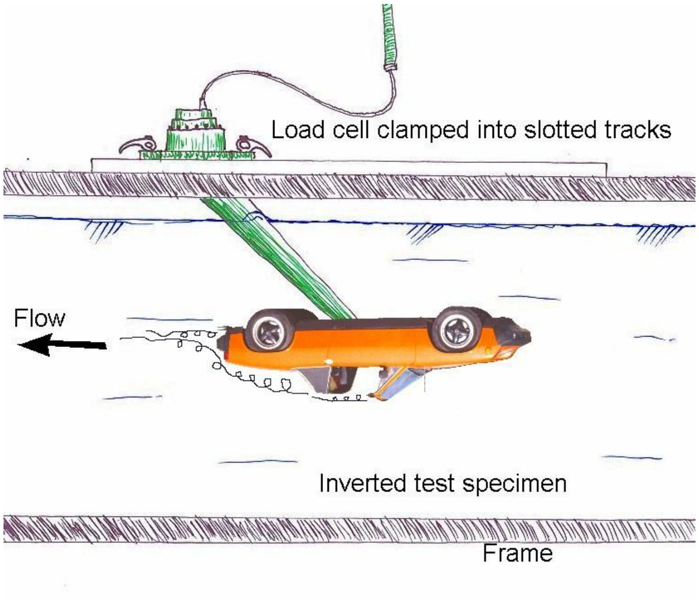

Figure 2.9: Car mounted (upside down) from above using slotted tracks.

such as load cells or laser velocimetry equipment. Aluminum t-rails can be affixed to the slots in order to mount equipment on sliding pillow blocks above the tunnel. Currently, these rails are being employed with both a servo-controlled traverse to position test bodies and a movable laser mount for a particle imaging system. For some experiments, using the slots/rails instead of the frame mounts may allow an installation scheme that places less material in the streamline. For others, it may make more sense to use the frame mounts. Together, these features make the test section extremely versatile.

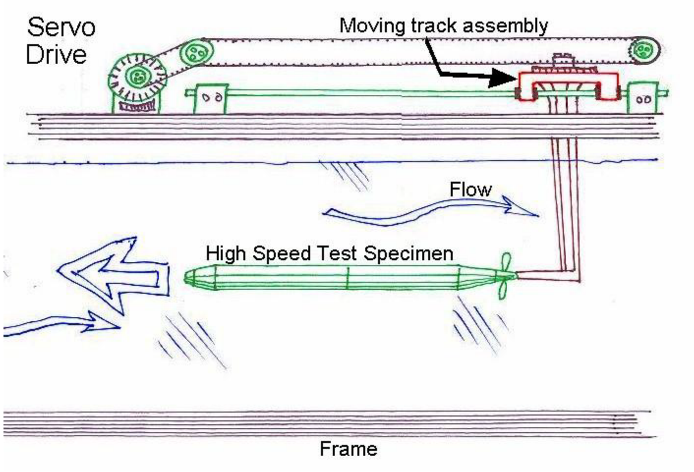

Figure 2.10: Towing experiment for a torpedo using a servo drive.

2.2.3 Channel

OPEN TOP The open top (Figure 2.3) design is employed to allow easy channel access and to enable fluid experimentation while towing. Towing can be employed for various fields of fluid dynamics research by allowing experiments at higher velocities, including exploration of vortex-dominated and cavitating flows. The open top feature provides the flexibility for a number of different layouts, and the long test section allows a reasonable distance along which short acceleration/deceleration runs can occur. It is expected that static models will use only $1m$ of the test section. For towing applications, up to $3m$ can be used effectively. An example of a towing setup is shown in Figure 2.10.

The walls of the channel are supported by vertical steel columns which are designed to deflect no more than 0.9 mm due to hydrostatic bending and moment forces in the long sections and impulse forces in the corners. Rigidity is further increased by steel plates which connect the walls at every corner as well as bracing supplied by the turning vane assemblies which are shown in each corner of the channel in Figure 2.3.

SMOOTH PANELS The design of the channel walls allows for any panel (wall or floor) to be changed easily from glass to steel or vice-versa and transition smoothly from one to the other on the fluid contact surface. Because glass must be much thicker than steel to support the same load, the panels would not meet evenly if they were set in the same frame (from the inside) and the thicker panels would create a lip which protrudes into the streamline (see Figure 2.11). Some water channels are designed with panels bolted from the outside to deal with this issue, however, this leaves a frame profile and fasteners (either bolts or rivets) in the streamline, which increases the roughness of the surface. This roughness can affect the boundary layer and flow conditions through the channel in much the same way the aforementioned lips would.

The channel is designed with a frame of constant cross section using spacers of varying thickness placed in-between the panels and the frame as shown in Figure 2.11. There are four different panel sizes, which vary in thickness from a steel sidewall that is $3mm$ thick to a glass floor panel that is $20mm$ thick. The space between the frame and the fluid contact surface is a constant width of $25mm$, and an appropriate spacer is used according to the thickness of the panel (i.e. $20mm$ panel + $5mm$ spacer or $3mm$ panel + $22mm$ spacer). The low carbon steel panels are MIG-welded in place and the stainless steel panels are TIG-welded. The glass panels are supported by rubber spacers and held in place by DOW 732 adhesive, although hydrostatic forces keep the panels in place when the tunnel is filled. The joints where the panels meet are filled with a specialty under-water sealant made by Sika^{TM}[10].

2.2.4 Turning Vanes

Located at each corner of the channel are a set of 90° radiused vanes (shown in 2.12) which help to smoothly turn the flow. This is a technique often employed in closed circuit wind tunnels[11] and air handling ductwork[12, 13] for multiple industries. Each vane consists of a quarter-circle with a $10cm$ radius and a straight $5cm$ fin on exit. The leading edge is rounded and the trailing edge terminates in a near-razor tip to minimze flow separation. The chord to gap ratio–defined as the ratio of chord length to spacing between the vanes—employed is 0.5. This configuration was chosen

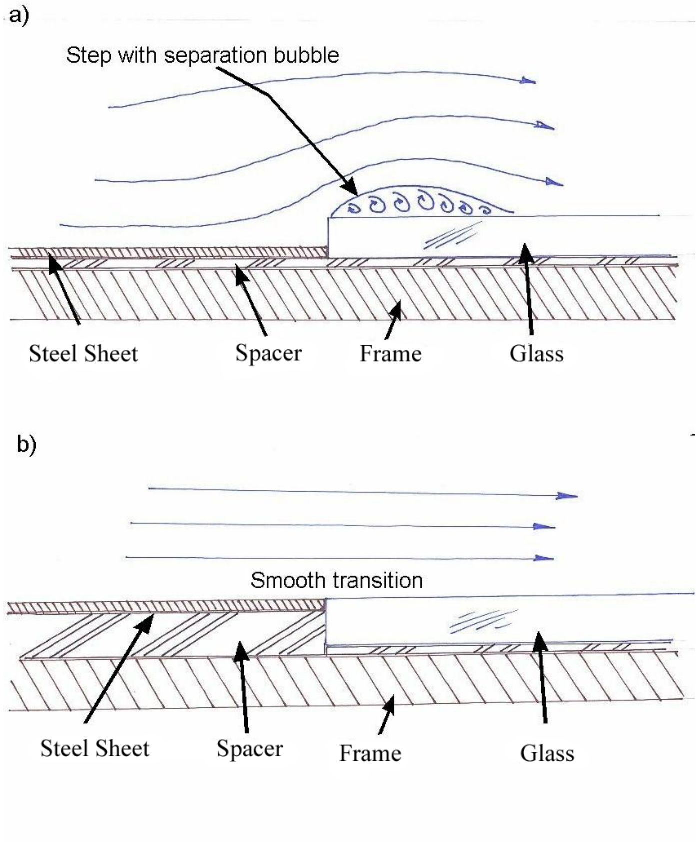

Figure 2.11: Flow over a) protruding lip b) smooth panel joint.

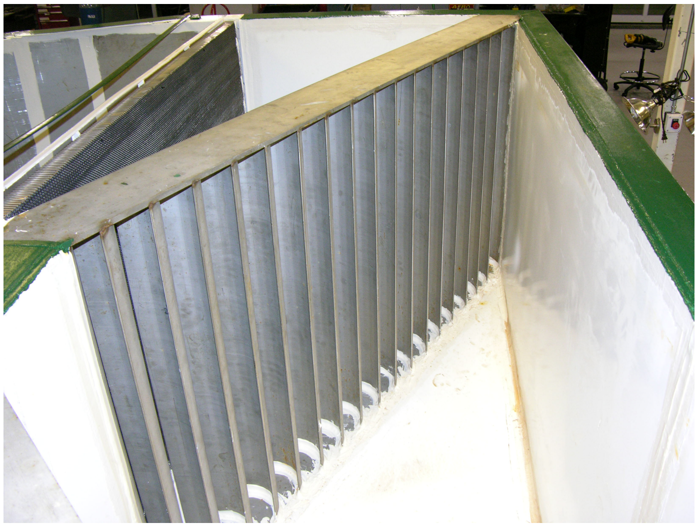

Figure 2.12: View of turning vanes entering the nozzle section of the channel.

based on experimental[11, 14] and computational[13] results which show that chord-gap ratios in the range of 0.2-1 are optimal for minimizing pressure loss in subsonic flows.

2.2.5 Flow Straightening

In order to produce more uniform flow in the test section, the spanwise fluid motions imparted by a) the rotation of the pump and b) the conservation of momentum around corners, two “flow straightening” features are employed. The first is a grid of PVC pipe sections placed in the flow immediately downstream of the SRP as shown in Figure 2.13. The pipe sections are $.6m$ long and $10cm$ in diameter. This grid serves to eliminate the large scale vortical structures created by the rotating propeller of the SRP. The second feature is a honeycomb matrix used to condition and straighten the water flow before it enters the nozzle and test section as shown in Figures 2.14 and 2.15. The honeycomb helps to create a more even velocity profile and increased laminarity (decreased turbulence) by forcing the water into pipe flow conditions (each cell acts like a small pipe in the direction of flow)[15] and eliminating smaller scale structures[14, 16, 17]. The honeycomb is constructed from $0.127mm$ T304 stainless steel foil. To achieve pipe flow conditions, a honeycomb depth to diameter ratio be-

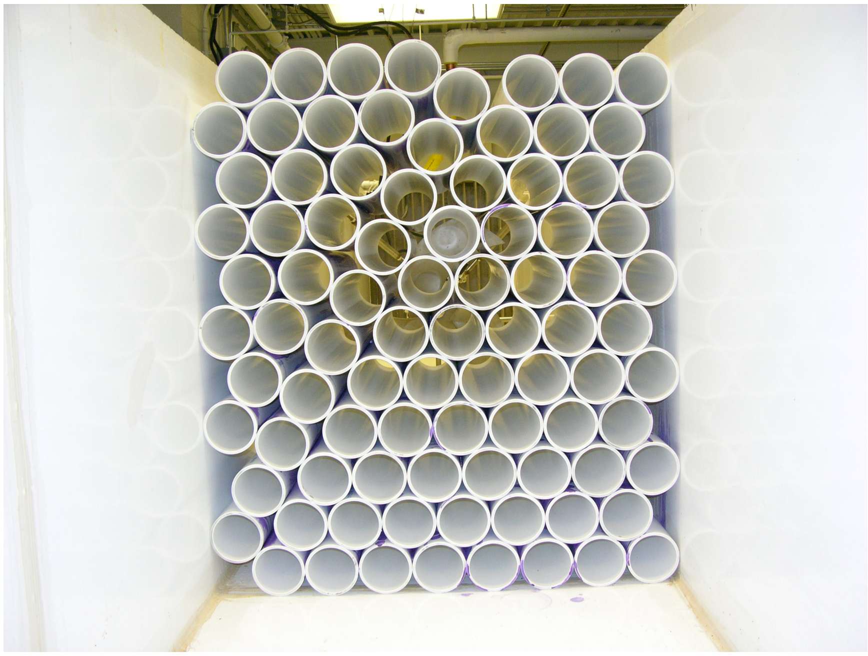

Figure 2.13: PVC flow straightener immediately downstream of pump.

tween 6 and 8 is sufficient[15]. The honeycomb is 5 cm thick and has a cell diameter of $6.4mm$. This yields a ratio slightly less than 8.

For minimum pressure loss, the honeycomb is placed in the widest part of the channel directly before the nozzle. The channel has a cross sectional area of $2m^2$ at this point, which reduces the velocity to half the test-section velocity. This yields the lowest possible pressure loss, which can be quite large for flow straighteners. It is, in fact, the static pressure drop mechanism that creates a more even velocity gradient[15]. The honeycomb is supported by a thin frame on the downstream side and can be removed easily to enable modification of flow conditioning. Different flow conditioners can be put in place of the honeycomb to create a plethora of experimental conditions. Additionally, mesh screens can be easily placed in the frame if velocity gradients are found to be too large.

2.2.6 Nozzle

The nozzle is located directly after the flow straightening honeycomb and further helps to reduce velocity variations and turbulence intensity before entering the test

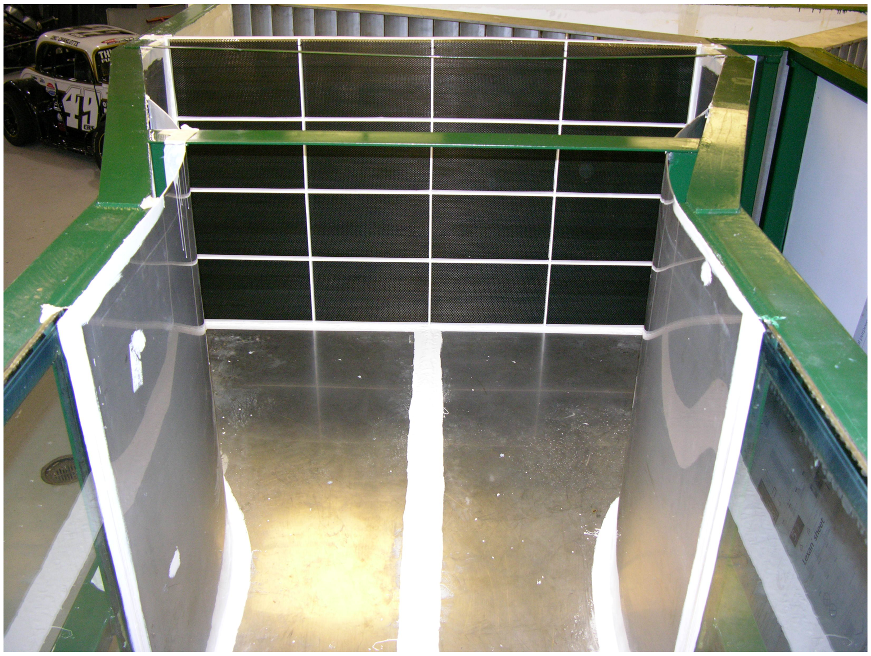

Figure 2.14: View of nozzle and stainless steel honeycomb flow straightener from downstrem.

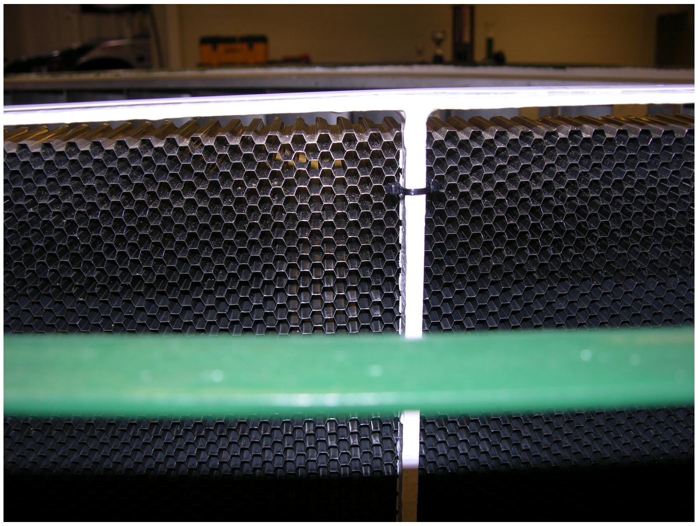

Figure 2.15: Closeup view stainless steel honeycomb flow straightener.

section. This also reduces small eddies and vortices created by flow separation in the honeycomb[18]. The honeycomb is located at the entrance of the nozzle and is twice as wide as the test section. The nozzle accelerates the fluid from the straightener to recover velocity heading into the test section. The nozzle is constructed of T304 stainless steel sheet rolled with a press and tig-welded into one large assembly. The nozzle has a contraction ratio of 2:1 which is somewhat low as a result of size, weight and cost considerations. It is $2m$ wide at the entrance, $1m$ wide at exit, and is $2m$ in length. It contracts to half-width at half its length (it is $1.5m$ wide after $1m$ in length). The entrance and exit are tangential to the side walls, and the inflection point is located at the center of its length. The radius is gradual enough to prevent flow separation and minimize the boundary layer heading into the test section.

2.3 Summary

A new water channel for fluid dynamics research has been constructed at the University of North Carolina at Charlotte. It is currently the fourth largest (by flow rate) in the United States. The primary design goal of this test facility was to provide an extraordinary volume of water through a large test section at a minimal turbulence level and with a flat velocity profile. The channel accommodates hydrodynamic experimental setups using a variety of mounting options including, universal test frame mounts and slotted rails/tracks. The constant cross section layout using a submerged recirculation pump requires much lower power consumption to maintain the same test velocity than a typical vertical-plane water channel design.

CHAPTER 3: DYNAMIC COUPLING OF OSCILLATING FOILS IN TANDEM

3.1 Background

The flocking, schooling, and swarming of large, multiagent systems have enjoyed extensive study in recent years[3, 19–24]. Applications range from fluid dynamics such as the schooling behavior of various animals or the design and placement of wind turbines in energy-producing "farms" to mechanical-electric systems such as sensing or self-assembling mobile networks. While there are a great number of scientific fields studying these systems, the central theme is that of a large group of interacting agents with a common goal or purpose. Whether the system expends energy or creates it, the coupled dynamics of the group play an important role in optimization and control. Dynamic analyses of such systems frequently invoke models governing localized interactions among small numbers of agents, viewing large-scale collective behavior as an emergent consequence of homogeneously distributed localized dynamics. From this perspective, the decentralized control of large multi-agent systems amounts to the determination of rules for local interaction that engender desired behaviors in the large.

Although such models are frequently claimed to represent, however simplistically, the dynamics within systems of aerial or aquatic organisms or vehicles, such models generally focus on the deliberate coupling of neighboring agents behavior through control assuming full authority over the motion of individual agents while neglecting fluid-dynamic coupling that might alter localized dynamics in spatially varying or time-varying ways. In reality, the exposure of an individual aquatic or aerial vehicle to the unsteady wake of a near neighbor can substantially alter the formers dynamics and even controllability. Fluid-dynamic coupling isn't necessarily an obstacle to the execution of purposeful maneuvers by a multi-agent system—indeed, such coupling can be exploited to achieve improved collective energy-efficiency [25, 26],—but its contribution to the dynamics of engineered systems that mimic flocks of birds or schools of fish is undeniable. The failure of many flocking and schooling models to explicitly acknowledge such coupling reflects not a skepticism of its relevance, but rather an awareness that the relevant physics is complex, presumably demanding high-dimensional models for accurate representation. Consequently, control algorithms rely on the ability of inputs to overcome and compensate for fluid-interaction effects rather than working with them to improve efficiency.

Although recent computational work[27] has focused on illuminating the subtleties of the dynamic interactions within fluid-bound multi-body systems of the simplest kind—comprising small numbers of linked planar members—a model for the fluid-dynamic coupling between active and passive bodies is largely unexplored. This study examines one of the most fundamental of such couplings: that between periodically-oscillating, rigidly-pivoting hydrofoils in tandem. The interaction of these rigid-body single degree of freedom (SDOF) foils represents a basis for the genereation of a model which describes the dynamics of the large system or network. In order to completely describe the vorticity-mediated dynamic coupling between two oscillating hydrofoils in a viscous flow, all possible system configurations must be examined. The present study examines the dynamics of several of these configurations and the efffect of the parameters which deifine the system. Here, the focus is on foils in tandem—that is, aligned with one another and parallel to the mean, uniform flow when unperturbed. The purpose is to explore the possibility of a set of locally-linear response models which can be combined to represent the fluid coupling in the large and allow integration of these effects into more robust and efficient control system designs.

3.1.1 Drag and Thrust of Oscillating Foils

One of the first examinations of oscillating foils was done by Katzmayr[28] in 1922 in which forces acting on various airfoils either undergoing oscillation or subject to varying incidences of oncoming flow in a wind tunnel were measured. The classical aerodynamic theory of oscillating airfoils originally arose from the problem of flutter in aircrafts and was pioneered by Theodorsen[29] in 1935. Subsequently, Von Karman and Sears[30] developed much of the analytical and qualitative theory on which a great deal of work has been done up to this point. Their analysis included two-dimensional potential flow and assumed planar vortices, small oscillation angles/frequencies, and linearized boundary conditions. This analysis was verified experimentally by Silverstein and Joyner[31] in 1939, and was used primarily for aircraft wing analysis throughout the next decade.

Inspired by nature, much attention has been given to the use of oscillating foils as propulsive devices, both experimentally[32–38] as well as numerically, theoretically and computationally[39–48]. The study of oscillating foils as propulsive devices and the understanding of aqutic/aerial locomotion in nature appear to be inextricably linked. In fact, a number of biomimetic studies have been carried out on live animals [49–54] in an attempt to describe the mechanics of natural swimming and flight. The majority of these studies seek to find efficient modes of operation; requiring the least amount of energy input to the system while generating as much thrust as possible. Interestingly, Triantafyllou et al.[55, 56] and Taylor et al.[57] compiled a wealth of data which show that observed cruising range for a wide variety of cruising species falls between $0.2 < St_A < 0.4$, where $St_A = fA/U_\infty$. Experimental studies[36, 38] on oscillating foils found that, indeed, propulsive efficiency peaks in that range, suggesting that animals swim and fly efficiently due to natural selection. The lessons learned from nature are intended to translate to, and improve the designs of, man-made propulsive deveices (see [55, 58, 59] for excellent reviews).

An experimental PIV study on oscillating foils by Godoy-Diana et al.[35] showed that the transition from drag to thrust is a function of St_A and lies within the above mentioned peak efficiency range. It has previously been shown[30, 60, 61], that the transition is associated with the wake transition from a Bérnard-von-Kármán street (BvK or commonly referred to simply as von-Kármán street) to a reverse BvK in which the signs of the vortices are opposite from their usual configuration (see Figure 3.1 for examples). At the transition, the wake consists of an aligned vortex street with vortices of alternating sign along the centerline of the wake[60]. While these phenomena are commonly observed, the physical reasons for them remain unclear.

3.1.2 Wake Structures of Oscillating Foils

While much of the historical focus on oscillating foils has been aimed at determining the drag/thrust forces associated with varoius modes of operation, visualization and analysis of the wake structure has also been examined. One of the earliest studies of the wake structure was done by Bratt[62] in 1953. A wind channel smoke visualization experiment was employed to observe various wake patterns while the effect of amplitude, reduced frequency (also called diameter-based Strouhal number, $St_D = fd/U_\infty$) and Reynolds number (Re) were examined. The study also included theoretical calculations of vortex patterns using two-dimensional potentional flow theory along with the assumption of infinite, discrete vortex sheets. Katz and Weihs[63] studied these wakes and observed a transition (present but not noted in[62]) at which the wake rolls up into a discrete concentration of vortices. Thomas and Whiffen[64] later studied this transition in more detail and several numerical treatments[65, 66] have attempted to describe it. Koochesfahani[60] studied this transition and further described a number of unique vortex patterns under different forcing conditions. Freymuth[67] used a flow visualization experiment to show that these spacially-periodic patterns are complex interactions between leading and trailing edge vortices.

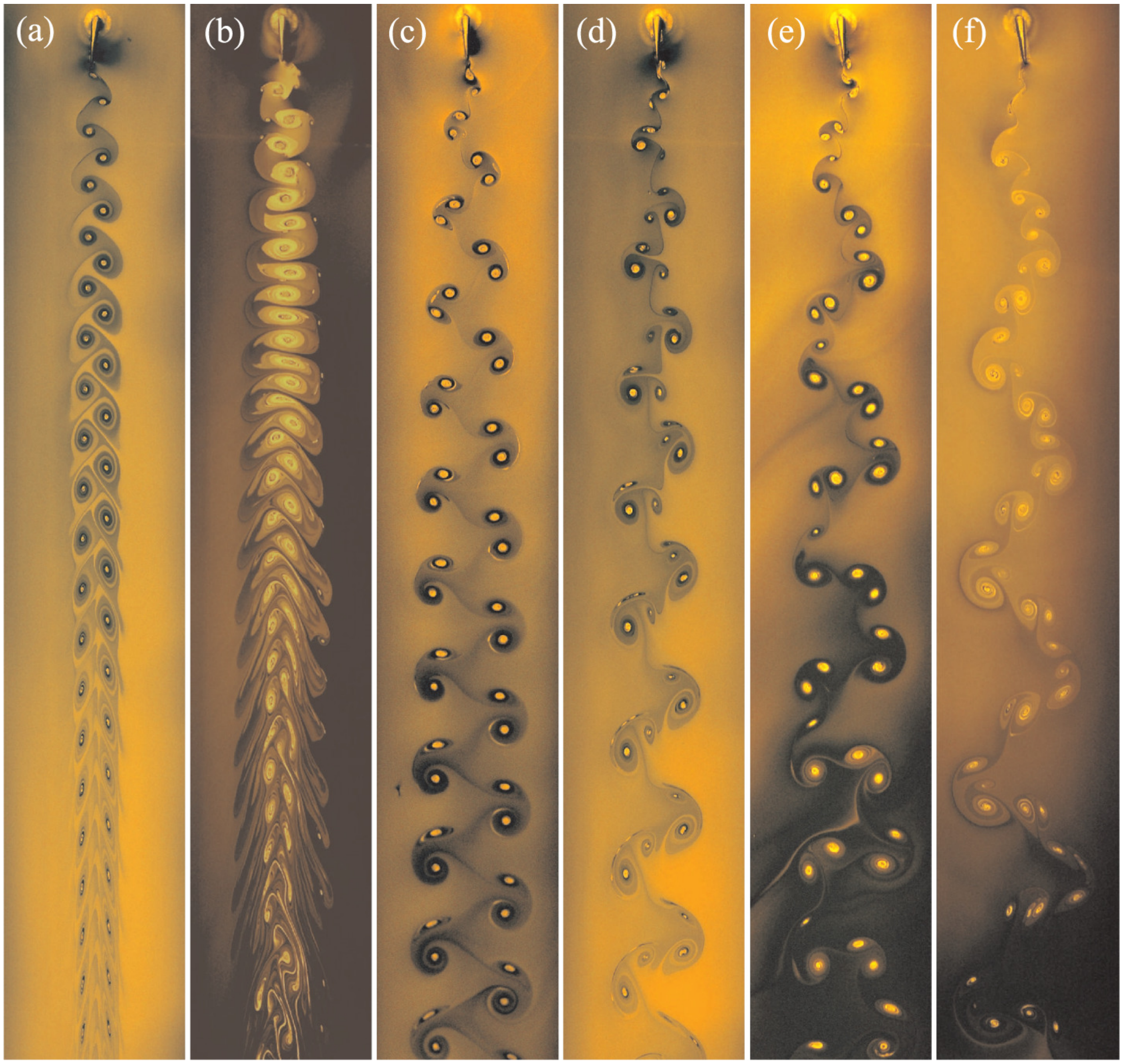

Figure 3.1: Selected wakes: a) BvK, b) reverse-BvK, c) 2P, d) 2P + 2S, e) 4P and f) 4P+2S. Taken from Schnipper et al.[68]. Reprinted with permission from Cambridge University Press.

In their pivotal experiment on transversly oscillating cylinders, Willamson and Roshko[69] observed a number of vortex modes (spatially-periodic patterns) locked into the body's translational frequency. The types of wakes observed were (in their nomenclature that has since been commonly adopted) 2S, 2P and 2C. In this nomenclature, a 2S wake is one in which two oppositely-signed vortices are shed per cycle and is typical of a BvK. This is the most common pattern observed. A 2P wake is the second most commonly observed and consists of a wake with two counter-rotating vortex pairs shed per cycle. These wakes have been observed in several oscillating foil studies[35, 68, 70–72] as well as e.g. behind vibrating cylinders[73] and deformable plates[74]. A 2C wake consists of two co-rotating vortex pairs per cycle. More exotic wakes with three or more vortex pairs per cycle have been observed[69, 75] as well as hybrid wakes[68, 71] which consist of various combinations of the modes described above. Figure 3.1 illustrates some examples of 2S, SP and 2S/2P hybrid wake modes and Figure 3.9 shows an example of a 2C mode.

In addition to defining wake modes, Williamson and Roshko[69] developed the idea that for a fixed Re, an "amplitude-wavelength plane" which completely maps the trajectory of the body can describe the mode of the wake. The phase plane, thus defined, specifies the wake mode for any given amplitude and St_D. Schnipper, Anderson and Bohr[68] studied the different regimes of an oscillating foil wake, and Figure 3.2 shows the A_D-St_D phase plane they obtained, where A_D is the diameter-normalized double-amplitude defined as $A_D = 2A/d$. Due to the nature of vortex interaction, it can be seen that the transitions between wake modes are rather abrupt. In addition, they presented a method of calculating the number of vortices shed per cycle as well as the circulation strength for vortices in 2P wake modes. In the present study, BvK, reverse-BvK, 2S, 2P and 2C wakes are observed and discussion of these modes can be found in Section 3.3.

At higher St_A, asymmetric wakes are seen in which the wake is shed with its

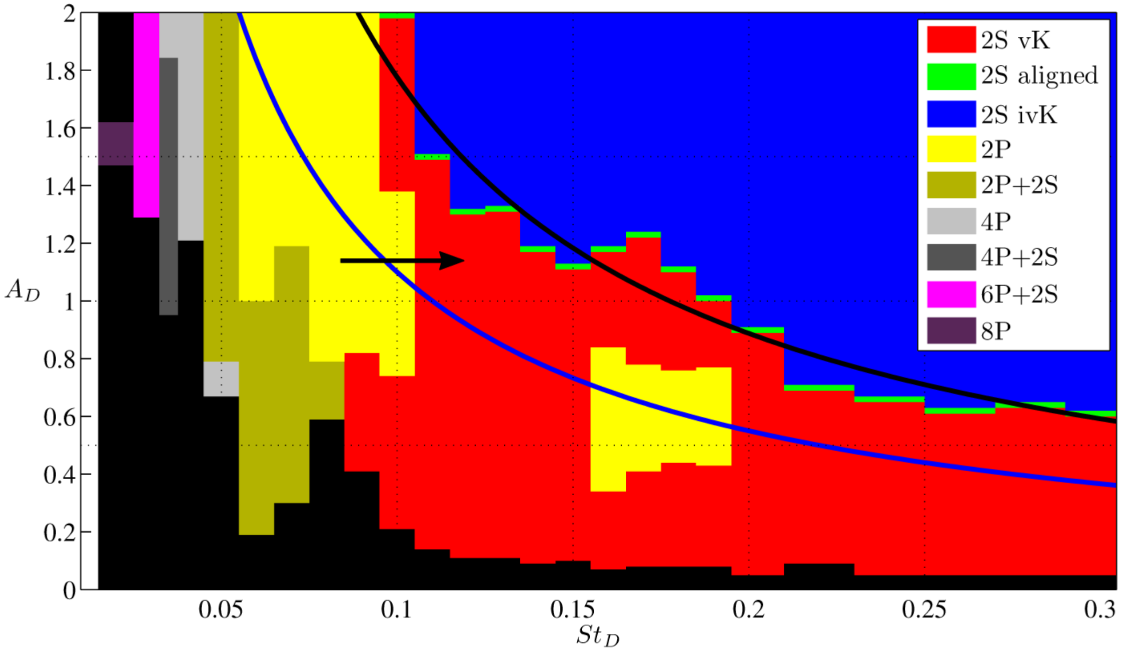

Figure 3.2: A_D-St_D phase diagram of wake modes. The color indicates the type of wake observed. The solid blue line marks the constant St_A value of 0.11, while the solid black line marks $St_A = 0.18$. The black are indicates regions where a synchronized wake was not observed. Taken from Schnipper et al.[68]. Reprinted with permission from Cambridge University Press.

centerline at an angle relative to the oncoming velocity[32, 35, 38, 60, 72, 76] and the symmetry breaking has no preference to either side of the wake. Godoy-Diana et al.[35, 72] took PIV measurements of oscillating foil wakes and claim this assymetry occurs at a transition where a dipole vortex is first shed and transient pressure gradients cause fluid momentum to shift away from the centerline of the wake.

While the majority of theoretical, computational and experimental analyses assume two-dimensionality, three-dimensional flow effects—like those induced by low aspect-ratio (A_R) foils or typical fish pectoral fins—can have a significant effect on wake structure and thrust production[55, 77]. Green and Smits[78] tested biologically inspired panels of varying ratios and found that A_R and A greatly affect the pressure distribution on the panels, vorticity generation on the panels, and thrust production. They proposed a scaling law to collapse pressure magnitude and thrust coeffecients given these three-dimensional parameters. Buccholz and Smits[79] performed flow visualization on a low aspect foil ($A_R = 0.54$) and described a three-dimensional BvK consisting of horseshoe vortices of alternating sign shed twice per oscillation cycle. A PIV study of an oscillating, finite-span ($A_R = 3$) foil by Parker, Ellenrieder and Soria[80] showed that, under thrust generating conditions, wingtip vortices cause the wake structure to be quite differnt from the typical reverse BvK, exhibiting a high degree of complexity. A numerical simulation by Dong, Mittal and Najjar[81] on thin ellipsoidal foils showed a wake consisting of vortex rings, whose mean flow is characterized by two oblique jets.

3.1.3 Oscillating Bodies in Tandem

The majority of research on tandem oscillating bodies addresses two bodies that are either a) both actively controlled, as in the case of tandem insect wings[58, 82] wings, or b) both passive, as in the case of two flags flapping in the wind[83]. In either case, it is well understood that downstream bodies are greatly affected by the wake of the upstream body. For rigid bodies in tandem, it has been show experimentally[27, 84, 85] and numerically[86–88] that downstream bodies gain an advantage through drag reduction from the upstream wake; although oddly, none of these studies addressed the case where the front body produces thrust and would therefore have a wake characteristic of a jet rather than a velocity-deficit.

Deng, Shao and Zhao-Sheng[89] performed a numerical study on two flexible foils oscillating in tandem to simulate a theoretical propulsion system for a ship. They found that, at low St_A, the drag of the downstream foil is in fact reduced, whereas at high St_A, the drag is increased but can yield higher thrust if the foil is controlled such that it "slaloms" through the vortices rather than plowing through them. They noted that for all cases, the thrust and efficiency of the front foil are improved for all St_A if the foils are closely spaced and approach that for a single foil as the spacing increases. Similar results were shown by Drucker and Lauder[52, 53] in their study of the interaction between the dorsal and tail fins of live bluegill sunfish. Again, the importance of the phase relationship to thrust enhancement of the downstream fin was emphasized. A computational simulation of the same system was carried out by Akhtar and Mittal[90] and found that the thrust augmentation was extremely sensitive to relative phase.

Warkentin and DeLaurier[82] tested an ornithopter configuration consisting of two sets of symmetrically oscillating wings located one behind another in a wind tunnel.

He et al.[88] showed that a modified wake impingement numerical model can more accurately simulate three-dimensional oscillating foils in tandem than those based on existing two-dimensional theory. They found that the best propulsive efficiency occured when the spacing was of the order of one chord length and the relative phase was near $\pm 50^0$.

Münch et al.[86] studied an active-passive system in which they did a numerical and experimental analysis of the low amplitude-high frequency coupling of elastic foil systems—such as a rotor-stator coupling in high speed turbines—to find a model which accurately simulates such a configuration. Their model was found to be in good agreement with their experimental data but applies primarily to small vibrations where boundary layer separation is not very significant.

Kim, Huang and Hyung[83] numerically modelled two flexible flags in tandem. They found constructuve and destructive interaction modes from the shedding of vortices of the upstream flag to the downstream (based on input parameters), and found that the former mode increases drag on the downstream flag while the latter decreases it.

A fascinating set of studies deal with the locomotion of passive foils in the wake of a cylinder. Liao, Dong and Lu[91] carried out a computational simulation of a passive foil placed in the wake of circular cylinder. They found various modes of vortex interaction such as induced separation, vortex pairing, and vortex impingement and described the lift and drag of the foil in various locations in and outside the cylinder's wake. Eldredge and Pisani[27] simulated the behavior of two-dimensional, linked, rigid bodies in a circular cylinder wake. The body consisted of three plates connected by two frictionless hinges and it was found that, once vortex rollup occurs, the passing vortices induce undulatory motion and that, for certain body lengths relative to the cylinder diameter, the body was propelled upstream towards the cylinder. It was also shown that the body is propelled just as effectively when the hinges are fixed, indicating that induced body indulation is not required to create a net thrust. Beal et al.[92] found that a dead fish (yes, a *dead* fish!) can extract sufficent energy from the vortices shed by a circular cylinder to passively propell itself upstream. They also tested a passively mounted rigid foil under roughly the same conditions and found that it too can propel itself upstream employing the same energy harvesting phenomena.

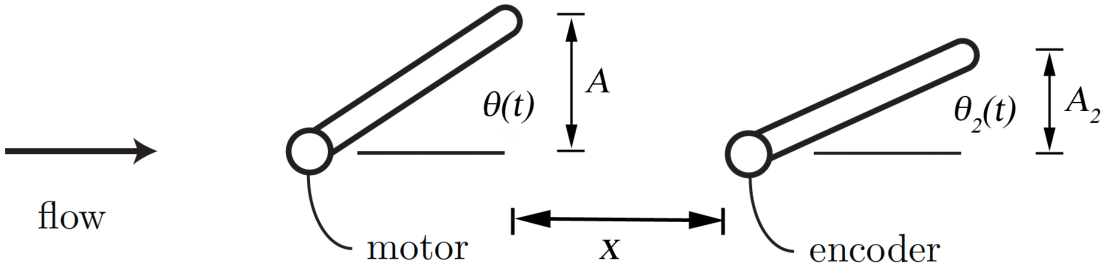

Figure 3.3: Schematic of experimental layout.

3.2 Experimental Setup and Parameters

The experimental setup consists of two hydrofoils arranged in tandem as depicted schematically by Figure 3.3. A laboratory realization is shown in Figure 3.4. The foil upstream is forced to oscillate; the foil downstream oscillates passively as it encounters flow structures shed from the foil upstream. The experimental control parameters are the flow velocity of the channel U_∞, the foil oscillation frequency f and amplitude A, and the spacing between foils x. They are placed into the test section of the hydrodynamic channel described in Chapter 2. The foils are solid, machined, aluminum panels with rounded (semicircular) leading and trailing edges, having chord $c = 12.7cm$, span $s = 25.4cm$, and width $d = 1.27cm$, yielding an aspect ratio $A_R = 2$. Each foil is pressed onto a $0.25in$ stainless steel shaft at the leading edge and cantilevered from a support (Figure 3.5) which has two low-friction bearings; the upper is a needle roller bearing and the lower is ball bearing. The force (applied at the trailing edge) required to cause foil rotation in a quasi-static test in air is less than the $0.02\,lbf$ resolution of the digital force gauge used to test it. The passive foil has a Contelec Vert-x touchless encoder mounted at the top of the support to read the angular position of the foil, while the actively forced foil has, instead, an Animatics SM2336D servo motor to control position as well as an internal optical encoder for reading angular position. The supports are mounted to an Isel double-rail traverse

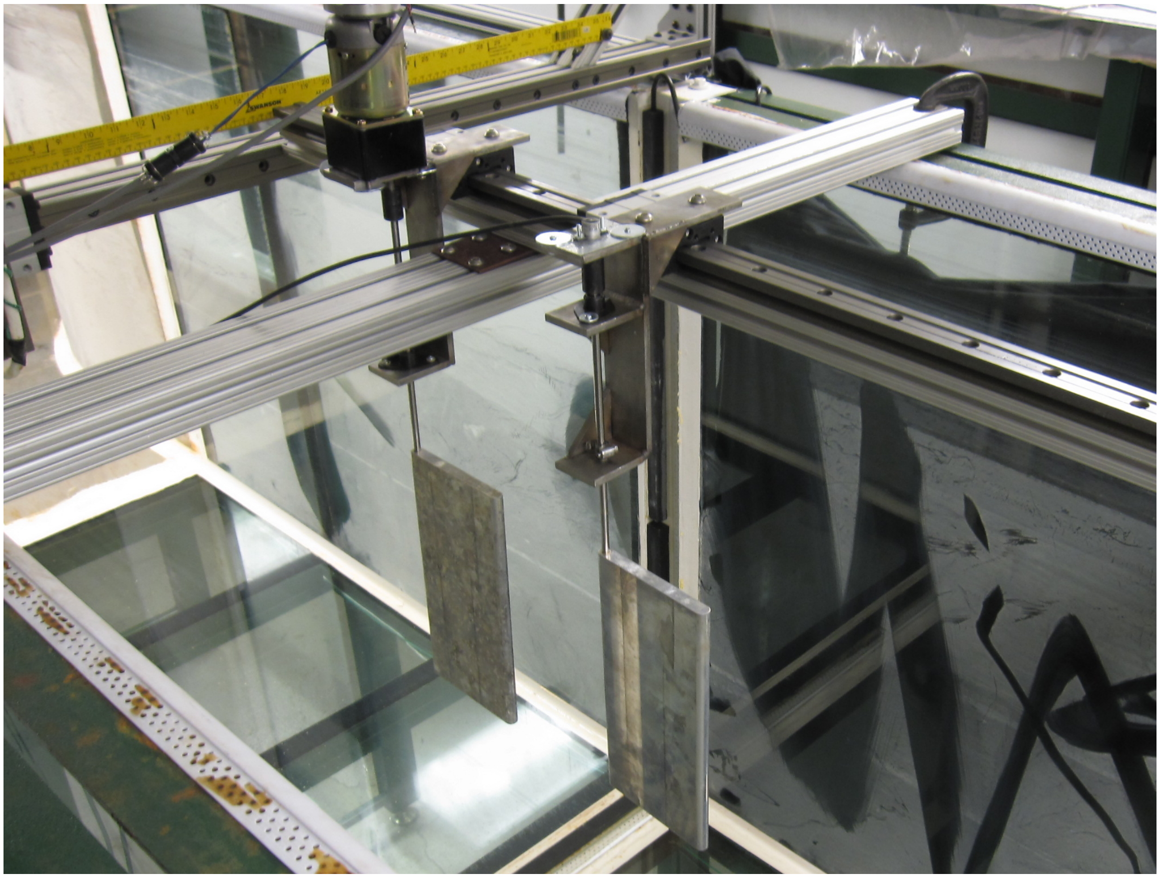

Figure 3.4: Laboratory realization of preliminary experiment is shown. A traverse and servo motor were added for the final experiment; the additional equipment made photographing the new experimental setup impossible.

atop the water channel. The traverse servo motor (Isel Schrittmotor) is operated by an Isel C142-4 controller having linear placement resolution of $0.1mm$. Data logging is done using National Instruments (NI) PCI-6602 (for the optical encoder) and USB-6008 (for the touchless encoder) data aquisition (DAQ) devices and LabView 10.1 software.

3.2.1 Angular Position Control

The upstream foil's motion is controlled by Animatic's SM2337D smart motor. The smart motor consists of an integration servo system including a servo motor, encoder, amplifier and controller which communicates with a PC via an RS232 connection. The periodic motion of the motor is specified by providing the controller a

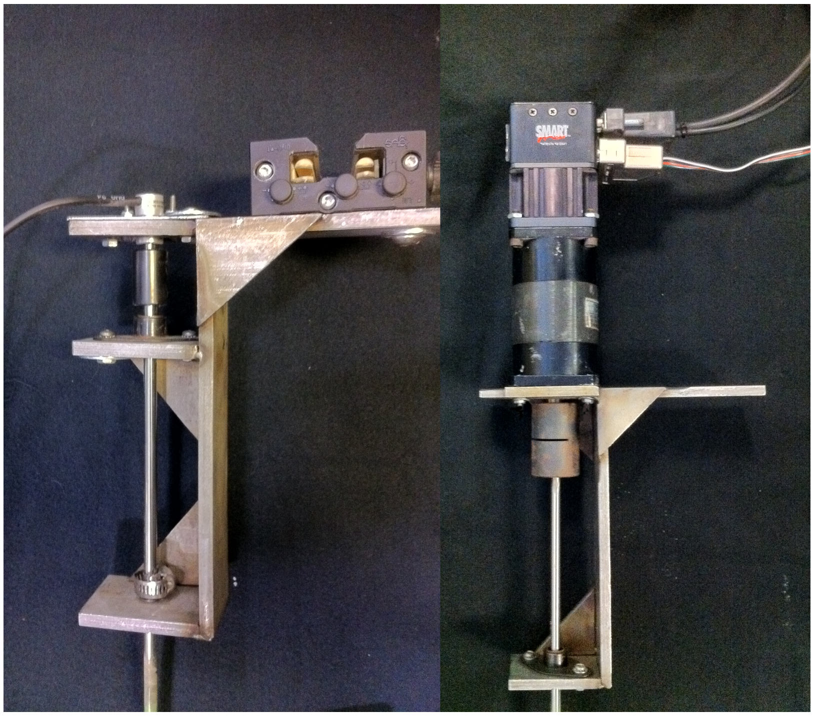

Figure 3.5: Supports used to cantelever foils into water channel. Passive foil support (left) with touchless encoder mounted at top of shaft. Driven foil support (right) with servo motor mounted.

continuous list of target positions at the frequency of approximately $31.8Hz$ (dictated by the controller's processor speed). The controller calculates the required velocity and acceleration based on a splined trajectory through the upcoming time/position targets. The motor position is checked regularly, and a standard PID control is implemented to acheive the required motion by

$$MV(t) = K_p e(t) + K_i \int_0^{K_L} e(\tau) d\tau + K_d \frac{d}{dt} e(t) \tag{3.2.1}$$

where MV is the manipulative variable, e is the position error and the specified parameter values are shown in Table 3.1. The maximum recorded position error in the experiment is $e = 33$ pulses ($\sim 0.12°$) while the motor itself has a maximum resolution of approximately $0.045°$ based on the accuracy of the incorporated optical quadrature encoder.

Table 3.1: PID Control Parameters.

PID Parameter	Value
Proportional Gain (K_p)	50
Integral Gain (K_i)	25
Differential Gain (K_d)	500
Integral Limit (K_l)	100
Max Possition Error	8000 pulses (of 98,000 /rev)

The more significant error source comes not from target location error, but rather from the discretized specification of the targets. The motion specified by the controller is not truly sinusoidal, but rather a splined fit to a discretized input sin function. Because the frequency of target specification is fixed, the approximation becomes less accurate as frequency increases. For instance, at a driven frequency $f = 0.1Hz$ (the lowest tested), there are 318 target locations specified for one period of oscillation, whereas at $f = 4Hz$ (the highest tested), there are only 8. In some cases, this creates a frequency error as large as 9% when comparing desired input frequency to that measured using the motor's optical encoder (DAQ and spectral analysis discussed in Section 3.2.2).

3.2.2 Angular Position Measurement and Spectral Analysis

Because of the errors inherent in the positioning of the oscillating servo motor, the motion of both the forced and passive foils are logged using NI LabView 10.1. The position of the forced foil is measured using the internal quadrature encoder via a NI PCI-6602 counter. The digital position is then converted to an analog signal within LabView prior to spectral analysis. The position of the passive foil is measured using a Centelec Vert-X touchless, permanent-magnet encoder. The output is an analog voltage signal (with an accuracy of ±0.3% at 12 bit resolution) which is read through a NI USB-6008 device. The scaled, analog position signals for both foils are sampled at $1024Hz$, and 46,080 samples are taken for each steady-state measurement. The samples are then passed through LabView's spectral analyzer instrument which

Table 3.2: Velocity and Reynolds numbers tested.

Velocity	Re_c	Re_d
$0.25 m/s$	31,750	3,175
$0.30 m/s$	38,100	3,810
$0.40 m/s$	50,800	5,080
$0.50 m/s$	63,500	6,350
$0.60 m/s$	76,200	7,620

carries out a Fast Fourier Transform (FFT) employing a Hanning window and returns the amplitude, frequency and absolute phase for the highest amplitude tone present in the signal. The resulting data is then output from LabView and written to file.

While the Nyquist criteria are more than sufficeintly satisfied in terms of maximum sampling frequency, the number of samples taken may generate amplitude estimation error for lower frequencies. This error becomes smaller with increased frequency. For example, at $f = 4Hz$, 180 periods are are sampled providing a good statistical base, whereas at $f = 0.1Hz$, only 4.5 periods are sampled.

3.2.3 Parameter Domain

An understanding of the dynamic coupling betwen the two foils as a function of U_∞, x, f, and A requires the exploration of an extremely cumbersome parameter space. Five velocities are tested and Table 3.2 shows their values and corresponding chord-, and width-based Reynolds numbers. Six foil spacings are tested in the range of $x/c = 0.5$ to $x/c = 5$, where x is is the distance from the trailing edge of the upstream foil when $\theta = 0$ to the leading edge of the downstream foil.

At each velocity-spacing combination, a broad range of amplitudes and frequencies (listed in Table 3.3) is chosen and a set of measurements is taken; more detailed frequency sweeps are then carried out for areas of interest to identify wake transitions. Figure 3.6 shows the range of tested oscillation parameters in terms of the reduced frequency St_D and diameter-normalized amplitude A_D, where $A_D = 2A/d$.

Table 3.3: Frequency and amplitude input parameters. The values in the columns underneath each (±)amplitude are the frequencies (in Hz) tested for that amplitude.

±2.5°	3.75°	5°	5.625°	7.5°	11.25°	12.5°	15°	17.5°	20°	22.5°	30°	37.5°	45°
0.25	0.25	0.25	0.25	0.25	0.25	0.25	0.25	0.25	0.25	0.25	0.25	0.25	0.25
0.50	0.50	0.50	0.50	0.50	0.50	0.50	0.50	0.50	0.50	0.50	0.50	0.50	0.50
0.75	0.75	0.75	0.75	0.75	0.75	0.75	0.75	0.75	0.75	0.75	0.75	0.75	0.75
1.0	1.0	1.0	1.0	1.0	1.0	1.0	1.0	1.0	1.0	1.0	1.0	1.0	1.0
1.25	1.25	1.25	1.25	1.25	1.25	1.25	1.25	1.25	1.25	1.25	1.25	1.25	1.25
1.50	1.50	1.50	1.50	1.50	1.50	1.50	1.50	1.50	1.50	1.50	1.50	1.50	1.50
1.75	1.75	1.75	1.75	1.75	1.75	1.75	1.75	1.75	1.75	1.75	1.75	1.75	1.75
2.0	2.0	2.0	2.0	2.0	2.0	2.0	2.0	2.0	2.0	2.0	2.0	2.0	2.0
2.25	2.25	2.25	2.25	2.25	2.25	2.25	2.25	2.25	2.25	2.25			
2.5	2.5	2.5	2.5	2.5	2.5	2.5	2.5	2.5	2.5	2.5			
2.75	2.75	2.75	2.75	2.75	2.75	2.75	2.75	2.75	2.75	2.75			
3.0	3.0	3.0	3.0	3.0	3.0	3.0	3.0	3.0	3.0	3.0			
3.25	3.25	3.25	3.25	3.25	3.25	3.25	3.25						
3.55	3.5	3.5	3.5	3.55	3.5	3.5	3.5						
3.75	3.75	3.75	3.75	3.75	3.75	3.75	3.75						
4.0	4.0	4.0	4.0	4.0	4.0	4.0	4.0						

This range is chosen to represent a useful engineering regime for aquatic locomotion and energy extraction. The hyperbolic curves in Figure 3.6 represent the previously mentioned Strouhal numbers ($0.2 < St_A < 0.4$) commonly observed in nature for cruising efficiency. Note that St_A is the amplitude-based Strouhal number defined as

$$\begin{aligned} St_A &= fA/U_\infty \\ &= St_D A_D. \end{aligned} \tag{3.2.2}$$

Besides aquatic locomotion, this range represents a wide collection of natural and engineered applications which employ relatively low-frequency/high-amplitude motion.

3.2.4 Wake Visualization

The wake visualization is carried out using the well known[93–96] hydrogen bubble technique in which electrolysis is used to generate hydrogen bubbles which follow the local flow. The setup consists of a small stainless steel probe wire ($0.8mm$ in diameter)

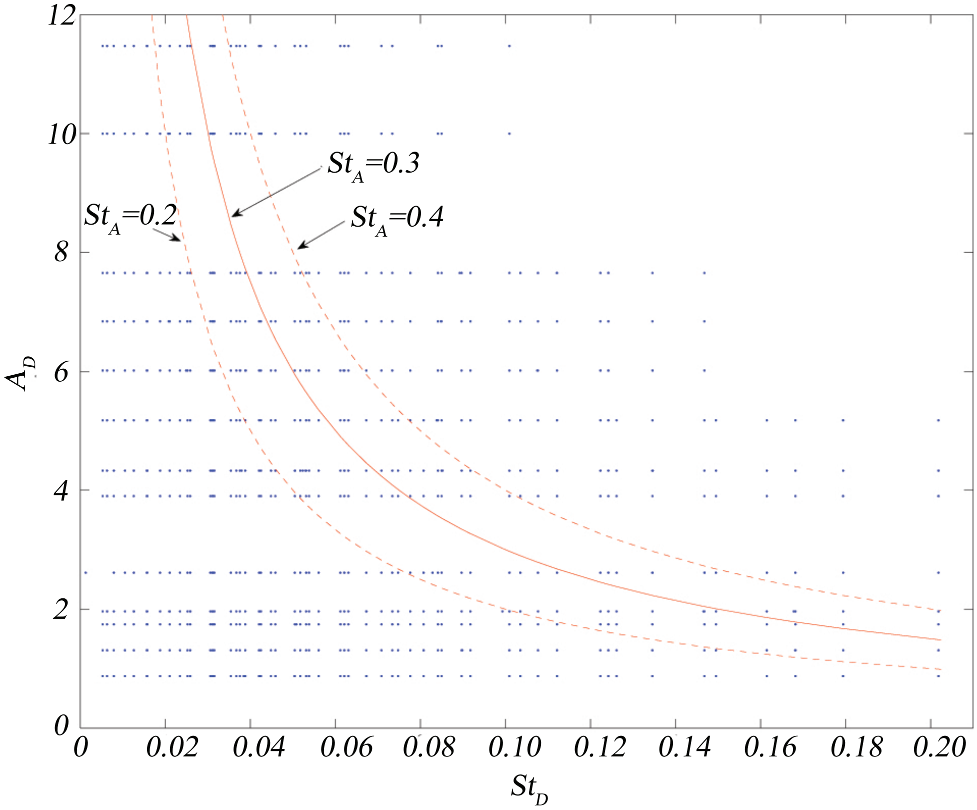

Figure 3.6: Range of tested A_D and St_D. Each blue dot corresponds with a tested configuration (i.e. a test was carried out at each point). The red lines represent constant values of St_A in the range commonly observed for cruising swimming/flight in nature.

placed upstream of the foil at the midplane height. The probe is negatively charged with a positively energized probe in the flow located approximately $0.5m$ away in the spanwise direction. A DC current of $40V$ is applied between the two probes. The eloctrolyte used is salt in a concentration of approximately 0.75 parts per thousand resulting in a current of $1.4A$ between the probes. The shed hydrogen bubbles are illuminated at the midplane height using a $500W$ halogen spot light and two $200W$ incandecent flood lights from each side of the test section. An $8\,bit$ CCD camera with 2048 x 2048 resolution is placed underneath the tunnel and aimed normal to the foil's midplane. A Tamron AF $18 - 250mm$ F/3.5-6.3 aspherical (IF) macro zoom lens is fitted and images are captured continuously at $14.7Hz$.

For Re in the range of this study, bubble visualization has some limitations. For fully developed turbulent flows, the drag and momentum forces on the bubbles can prevent them from following local fluid paths faithfully[97, 98] making quantitative analysis less accurate. However, qualitative flow observations are still valid in the majority of subsonic cases and have been employed quite regularly for such turbulent flows[99, 100]. Another source of error is the bouyancy driven rise of the bubbles as they are convected downstream. The vertical velocity normal to the midplane can be estimated[101] by

$$vc = \frac{(d_b)^2 g}{12\nu} \tag{3.2.3}$$

where vc is the velocity, d_b is the mean diamter of the bubbles, g is the local acceleration force due to gravity and ν is the kinematic viscosity of water. For estimating vc, the diameter of the bubbles is found to be $d_b = \mathcal{O}(.1mm)$ yielding $vc = \mathcal{O}(8mm/s)$. The maximum vertical rise calculated (i.e. at the lowest U_∞ and the largest x tested) is thus $\mathcal{O}(20mm)$. While a rise of $20mm$ out of the plane is not insignificant, the qualitative analysis performed for the present study are not greatly affected. The vertical rise does, however, create difficulty in maintaining focus on the bubbles due to the fact that the focal depth of the camera lens is set for the midplane. The result is that some images become slightly blurry with increasing downstream distance.

3.3 Wake Modes and Transitions

It is important to first examine the wake behind the upstream foil in order to understand the response of the downstream foil and define their dynamic coupling. As mentioned previously, the wakes shed by oscillating foils have been examined both experimetnally and numerically by a number of researchers and the possible wake modes resulting from vortex coupling and interaction can be quite complex. It is found that although the finite-span foil used in this study has a three-dimensional wake, the visualization data in the mid-span plane show good agreement with previous two-dimensional results found in the literature. This suggests that some methods and analyses employed for infinite, planar foils can be applied to finite-span foils.

3.3.1 Wakes at Low Amplitude

For the static case when f=0, the wake consists of a BvKstreet as seen in Figure 3.7. This is a well known phenomena for blunt bodies (see [30, 69] amongst others) and the shedding frequency for this mode can be calculated as

$$f = 0.198\frac{U_\infty}{d}(1 - \frac{19.7}{Re}), \tag{3.3.1}$$

where Re is the diameter-based Reynolds number, yielding f in the range of $3.3 - 7.9Hz$ for the tested velocities. Equation 3.3.1 applies only in the range of Re where this wake mode is observed and the experimentally measured frequencies in the present study are in excellent agreeement with those calculated using it.

As the frequency is increased, several transitions can be seen in the wake and a number of vortex modes develop. Figure 3.8 follows the evolotuion of the wake for a constant (small) amplitude of oscillation, $A = 5°$. For $f \leq 0.5$, the wake consists of an undulating BvK street. This is essentially a superposition of the low amplitude BvK street and the large amplitude oscillating fluid momentum of the

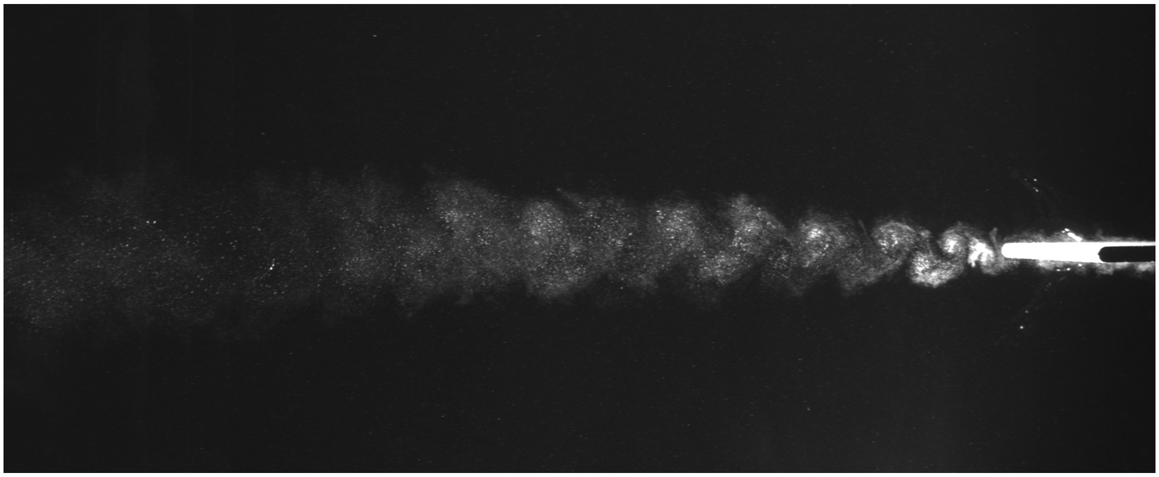

Figure 3.7: BvK street seen behind static foil. $U_\infty = 0.5m/s$.

foil. Frequency of the street is unchanged, and the lower undulating frequency is locked-in to the foil's motion. In this regime, increasing the frequency simply changes the spatial wavelength of the observed wake.

As f approaches $0.75Hz$, the roll-up transition is observed where the wake consists of discrete concentrations of vorticity. Here, the BvKstreet is no longer seen. In fact, the wakes observed at $0.75Hz$ and $1.0Hz$ are 2C wakes with a co-rotating vortex pair shed every half-cycle. Figure 3.9 shows a closer view of the 2C wake.

A 2S BvK regime is seen (in Figure 3.8) from $1.25 - 2.0Hz$. This type of wake is similar in topology to the natural vortex shedding wake observed in the static case, however the alternating sign street is locked-in to the frequency of the foil motion. This mode indicates that the foil is still in the drag regime[35, 60, 68]. The thrust regime is seen from $f \geq 2.5Hz$, where the wake consists of a 2S reverse-BvK mode. This corresponds well with previous studies[35, 38, 55, 56, 68] that show the transition to occur between $0.2 < St_A < 0.4$, as the present data find the transition to occur near $St_A \simeq 0.22$. The transition to thrust is punctuated by a 2P wake at $2.25Hz$ which is shown more closely in Figure 3.10. Further, it is found that the 2P mode only occurs for $3.25° < A < 11.25°$. The existence of a 2P wake for a small range of A_D near the drag-thrust boundary was also observed by Schnipper et al[68] corresponding to the

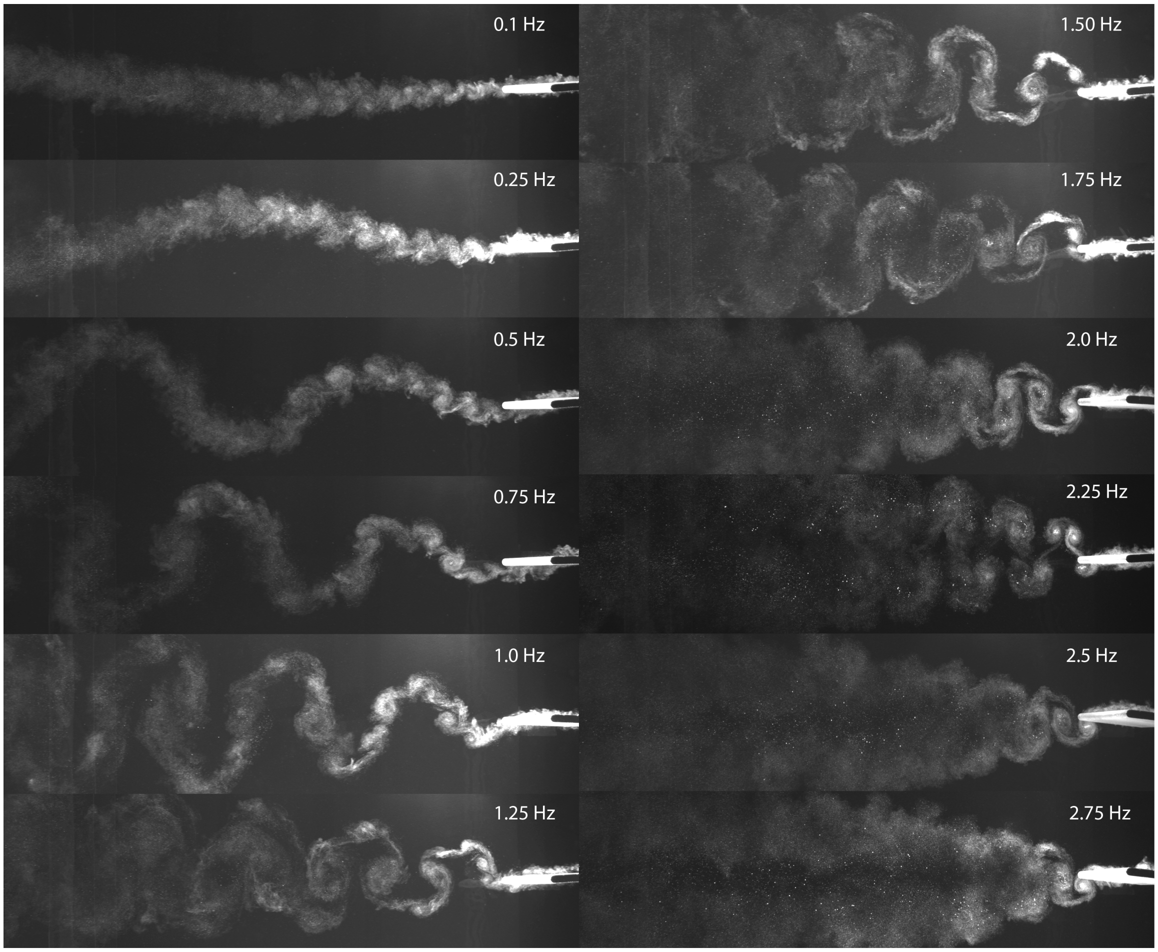

Figure 3.8: Wake transitions as a function of frequency for low amplitudes. $U_\infty = 0.25 m/s, A = 5^\circ$

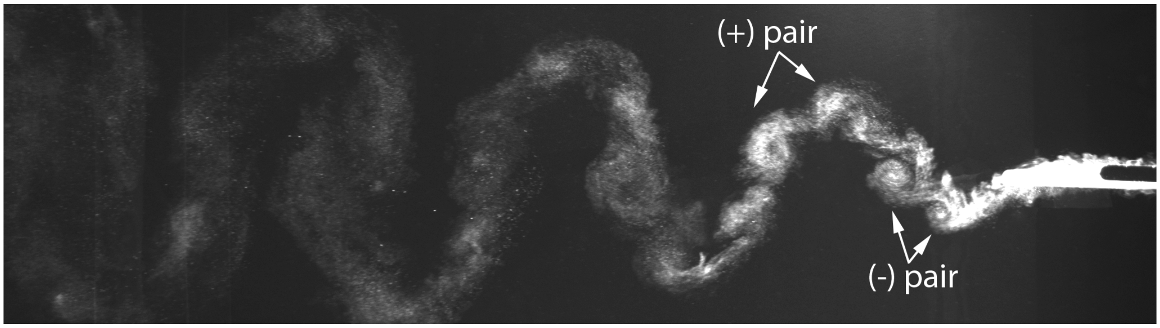

Figure 3.9: 2C wake seen at $U_\infty = 0.25m/s, A = 5°, f = 1.0Hz$

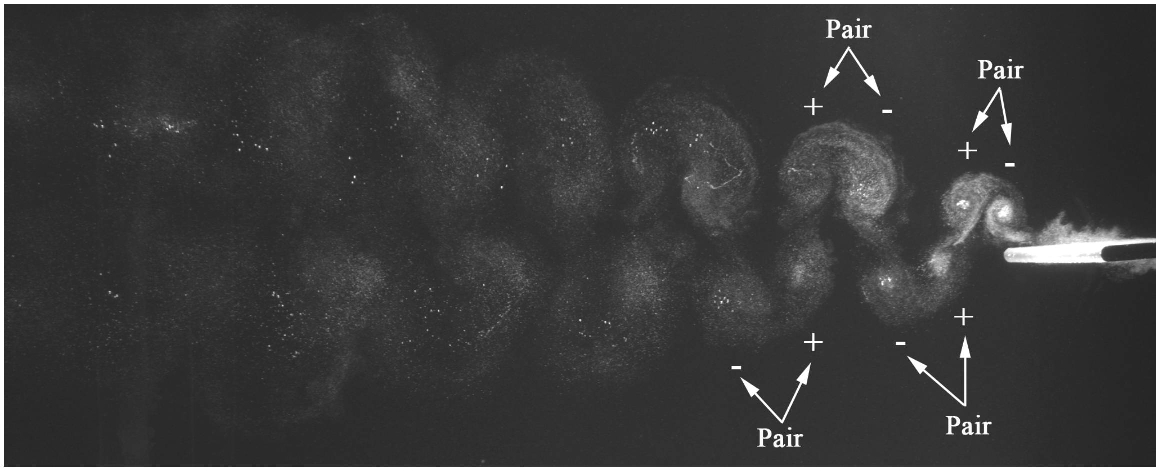

Figure 3.10: 2P wake seen at $U_\infty = 0.25m/s, A = 5°, f = 2.25Hz$

yellow 2P "island" in Figure 3.1.

3.3.2 Wakes at High Amplitude

A frequency sweep at larger amplitudes—e.g. $A = 15°$ shown in Figure 3.11—yields slightly different phenomena. In the undulating wake regime before the rollup transition, the larger amplitude oscillation causes the flow to separate from the leading edge and shed a large vortex along with the undulating wake. This separation wake, shown closely in Figure 3.12, is found to occur during the undulating wake regime for all $A > 11.25°$ and causes a bifurcation in the dynamic coupling of foils which is discussed in Section 3.4.2. As the rollup transition occurs, near $f \simeq 0.5Hz$, a 2P + 2S hybrid wake mode is found (Figure 3.13) which is, once again, consistent with two-dimensional foil wake anlysis where this regime is also found by Schnipper et

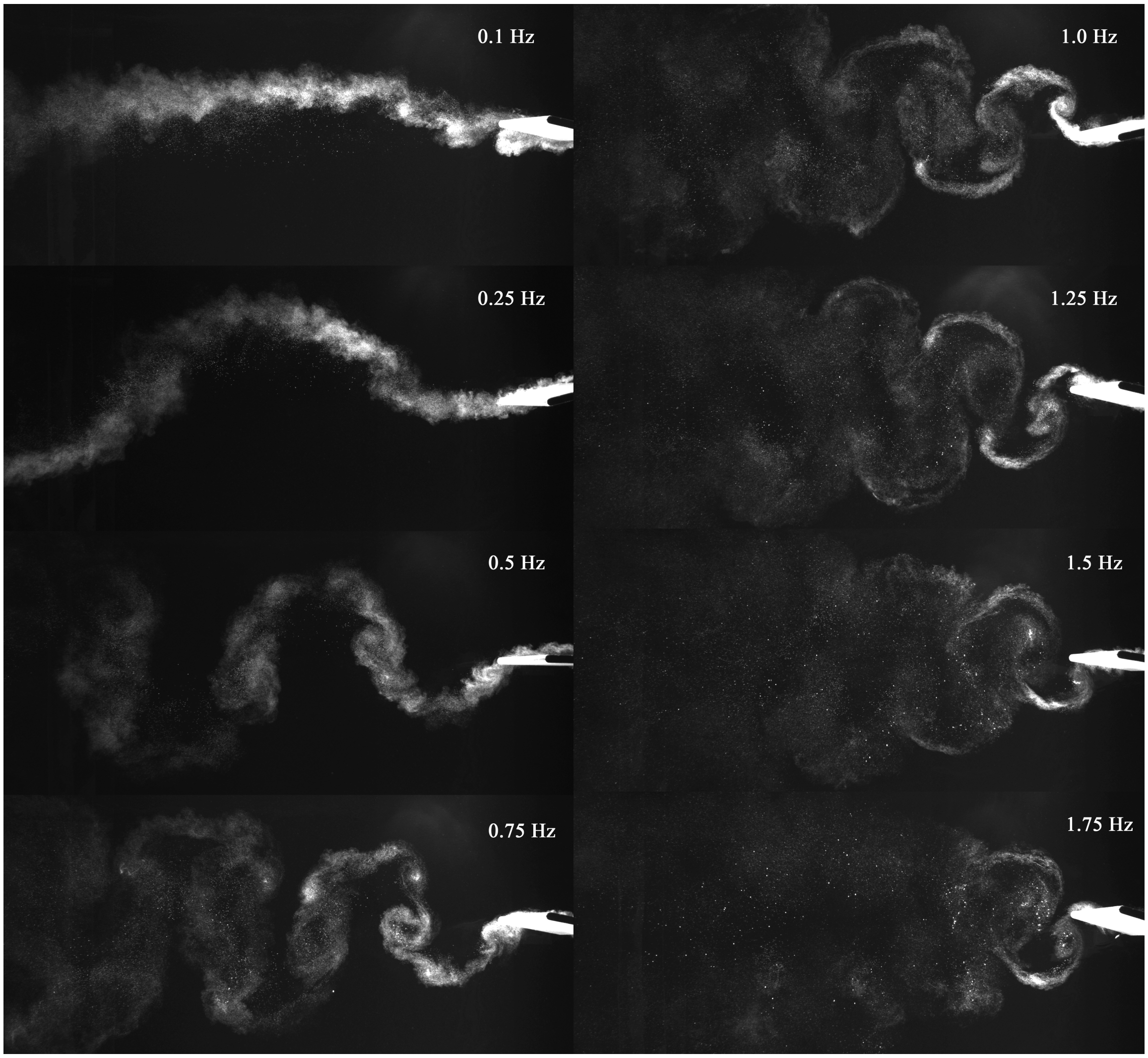

Figure 3.11: Wake Transitions as function of frequency for high amplitudes. $U_\infty = 0.25 m/s, A = 15^\circ$

al.[68] as Figure 3.1 indicates.

The transition to thrust is found to occur near $f \simeq 1.0Hz$ where an aligned 2S wake is observed. This translates to $St_A \simeq 0.26$ which agrees well with the observations at lower amplitude oscillations. In fact, the transition is located between $0.22 < St_A < 0.28$ for all experiments in this study and perhaps this range could be narrowed with data taken at higher resolution. Beyond this transition, 2S reverse-BvK modes are observed.

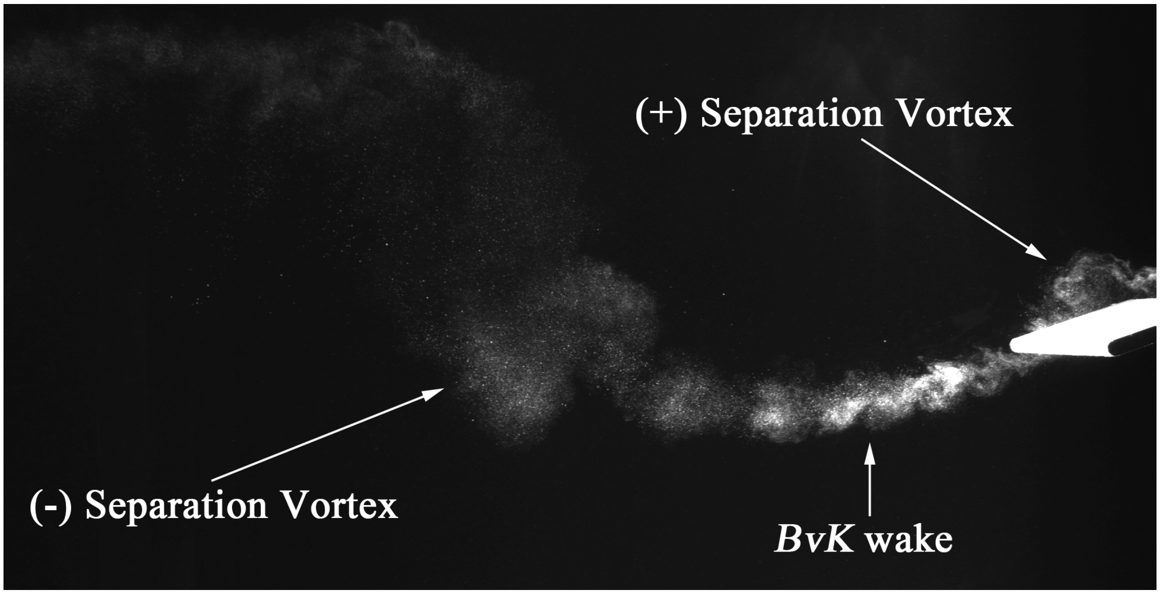

Figure 3.12: Flow separation wake. $U_\infty = 0.25m/s, A = 15°, f = 0.25Hz$

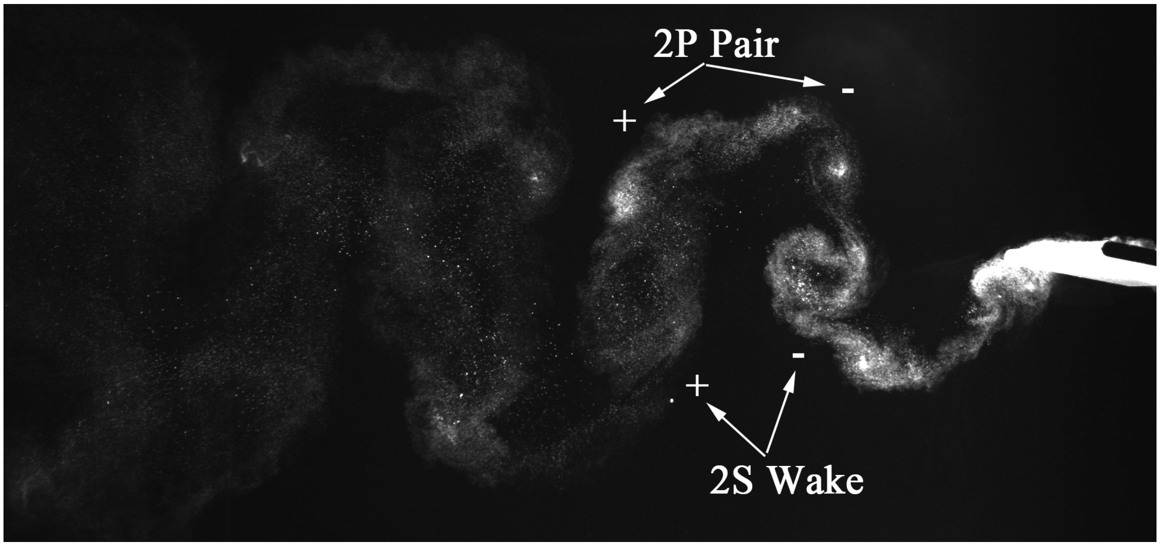

Figure 3.13: 2P + 2S hybrid wake. $U_\infty = 0.25m/s, A = 15°, f = 0.75Hz$

3.3.3 Reynolds Number Effects

In the previous sections, the wake modes were described for low and high amplitude oscillation across a range of frequencies all at a single velocity, $U_\infty = 0.25 m/s$. The question follows: What is the effect of Reynolds number on the wake structure? This has been largely unaddressed in the literature as wake structure studies have primarily been done at a single Re. Willimson and Roshko[69] first introduced the idea of representing wake modes in a A_D-St_D phase plane and proposed it for a fixed Re. However, Bratt[62] found experimentally that the flow structure depends primarily on reduced frequency even when the velocity varies by a factor of 4. Both Schnipper et al.[68] and Ramiro-godoy et al.[35] state that the phase-plane representation is meant to represent the wake modes only for a fixed Re, however, the former carried out experiments at two different Re which varied by a factor of 2, and found the data to collapse to a single plane.

In the present study, it is found that, within the tested chord Reynolds number range of $25,000 < Re_c < 60,000$, the wake structure appears to be independent of Re. Figure 3.14 for example, shows the effect of varying Re while maintaining the same St_D for three different wake modes. This indicates that, for the observed Re range, the wake structure is a function only of A_D and St_D.

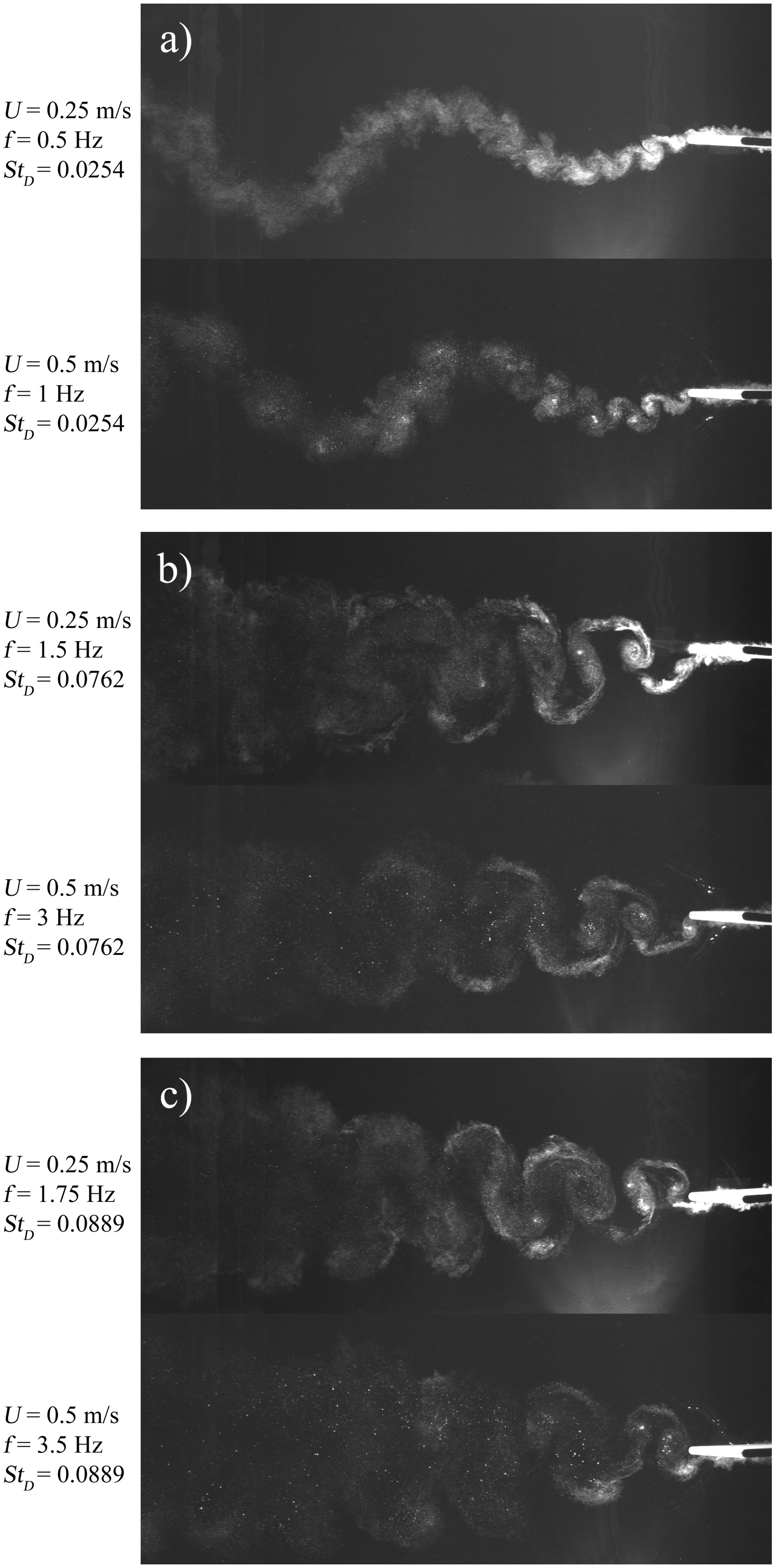

Figure 3.14: Reynolds number independence of wake topology. Wake shown at a) $st_D = 0.0254$, b) $st_D = 0.0762$, and c) $st_D = 0.0889$, each at $A = 5°$.

3.4 Frequency Response Models

The system depicted in Figure 3.3 represents the simplest functional unit in an arbitrarily large network of oscillating bodies coupled through vorticity-mediated interactions. The control of energy flow through such a network—e.g. a school of swimming robots seeking to maximize the internal recapture of its own wake energy—requires, in practice, a description of the coupling between adjacent elements that should eschew costly explicit modeling of the mediated vortex phenomena. Accurate, low-order, models, require the system to display linearity for any given configuration.

3.4.1 Requirements for System Linearity

In order to examine the linearity of these systems, it is neccessary to define the system and establish criteria for linearity. The system consits of two foils in which the upstream foil is forced to oscillatate periodically such that

$$\theta(t) = A \sin \omega t, \tag{3.4.1}$$

where θ is the angle of incidence of the foil, A is the amplitude of oscillation and ω is the angular frequency of oscillation. The downstream foil oscillates passively as it encounters flow structures shed from the foil upstream and the steady state response of the downstream foil due to convected vortical energy is examined. Were the two foils coupled by stable linear dynamics for a given system, then it would be observed that

$$\theta_2(t) = A_2 \sin(\omega t + \phi), \tag{3.4.2}$$

where the amplitude ratio $|A_2/A|$ and the phase shift ϕ would depend on the frequency ω but not on the input amplitude A.

Here, the "system" must be defined and the parameters that fully specify the system are the foil spacing x and the mean ambient flow velocity U_∞. It would be expected that for each system defined by these two parameters, a different frequency response function (FRF),

$$\left|\frac{A_2}{A}\right| = fn(\omega) \tag{3.4.3}$$

would be observed. A solid-mechanics analogue could be varying parameters such as spring rates or support constraints which would, similarly, yield varying response. Additionally, defining the system response can be done only for a specific range of A and θ, however, the span of frequencies and amplitudes examined in this study (see Figure 3.6 and Table 3.3) represent a useful range for aquatic locomotive engineering applications. Ideally, each A-θ system should be described by a distinct FRF or distinguishable set of FRFs. A family of such functions could then be parameterized by the inputs.

3.4.2 System Response

It is found that in nearly every case tested, following an interval no longer than a few oscillations during which transient dynamics die out, the downstream foil oscillates sinusoidally—modulo small-amplitude, high-frequency noise—at the same frequency as the upstream foil. The only exception occurs when the response amplitude of the forced motion is smaller (or is essentially negligible) than that of vortex-induced vibrations (VIV) caused by the natural shedding of vorticity from the foil. VIV is a commonly observed phenomena[73] where forces from vortices shed by a body cause it to oscillate. In these cases, the measured oscillations of the downstream foil are found to match the natural shedding frequency given by Equation 3.3.1.

For each forcing frequency, furthermore, the amplitude ratio $|A_2/A|$ and the phase shift ϕ prove to be independent of the amplitude A either a) throughout the entire range of A for a system or b) for discrete regions of A within a system. The latter is primarily observed. For example, Figure 3.15 shows the attenuation and absolute phase shift for a system ($U_\infty = 0.6m/s, x/c = 2.5$) displaying linearity throughout the entire range of A, while Figure 3.16 shows a system ($U_\infty = 0.4m/s, x/c = 1.5$) exhibiting discrete regions of linearity. In the former, it can be seen that the criteria for establishing linearity are satisfied. That is, both the attenutation and phase shift are functions of frequency only.

Figure 3.16 shows, instead, two distinct regions of linearity; one existing when $A \leq 7.5$ and the other when $A \geq 11.25$. This step-change in response (or system bifurcation) is seen in nearly every system and corresponds with the amplitude threshold for flow separation. As the system response is due to convected vorticity between the two foils, it is perhaps intuitive that bifurcations in system linearity would occur as a direct result of the abrupt changes in wake structures shed from the upstream foil. As discussed in Section 3.3.2, higher oscillation amplitudes in the undulating wake regime causes the flow to separate, convecting large vortices downstream. It seems that the adverse pressure forces from the separation vortices in the wake cause (relatively) larger displacement of the downstream foil than does the undulating wake alone. Separation is seen at lower frequencies whenever $A > 11.25°$, and in each system where it is observed, it results in higher attenuation for the same ω than attached flow.

Another apparent break from linearity can be seen in Figure 3.16. For $A = 3.75°$ and $A = 5°$, the attenuation has a large dip near $f = 2.25Hz$. This corresponds with the location of a 2P wake mode which occurs for a only for a very narrow island at lower amplitudes as mentioned in Section 3.3.1. Flow visualization of this coupling mode is shown in Figure 3.17, while Figure 3.18 shows the 2S coupling mode for the same A and slightly lower f. It can be seen that the 2P wake with counter-rotating vortex pairs convecting downstream resulting in co-rotating vortices acting nearly symmetrically on the downstream foil at any given time essentially balancing each other out and creating neutral forcing of the foil. The 2S wake, on the other hand, allows for alternating vortices of opposite sign to act on the foil. Clearly the 2S wake

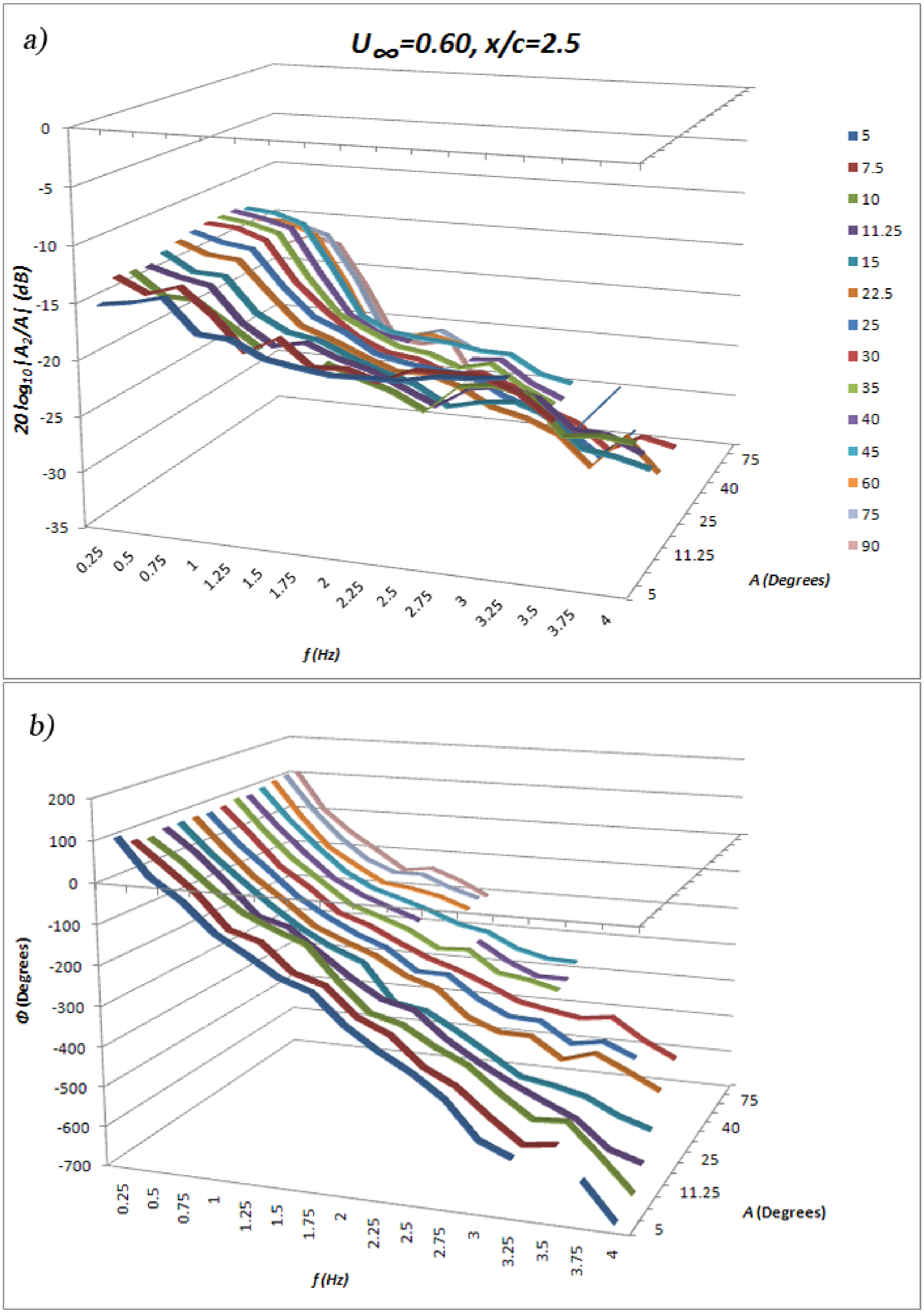

Figure 3.15: System frequency response for $U_\infty = 0.6 m/s, x/c = 2.5$ as a function of forced frequency and amplitude. Each color represents the amplitude (A) indicated by the legend. a) Attenuation of system (in dB). b) Absolute phase shift of system.

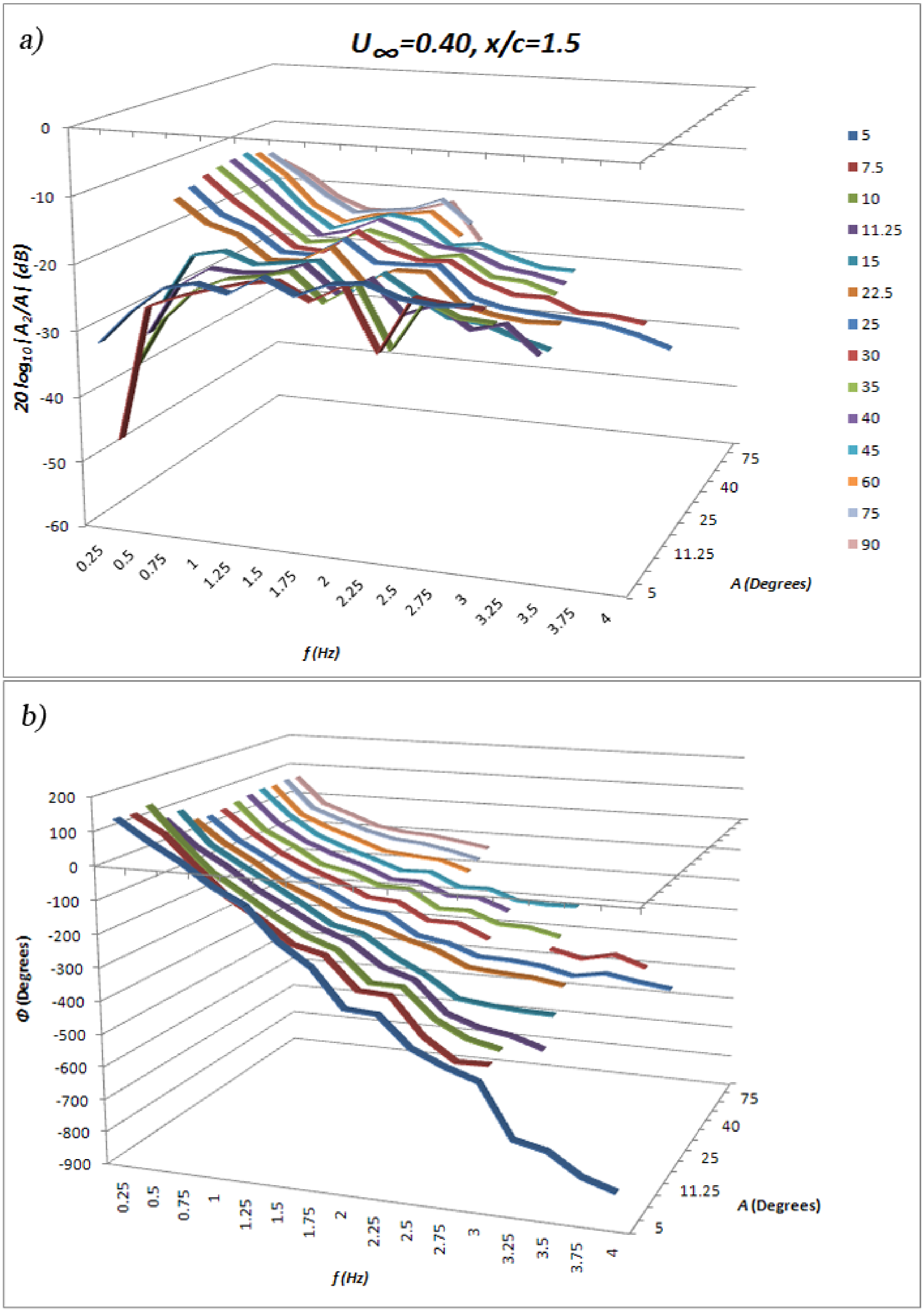

Figure 3.16: System frequency response for $U_\infty = 0.4m/s, x/c = 1.5$ as a function of forced frequency and amplitude. Each color represents the amplitude (A) indicated by the legend. a) Attenuation of system (in decibels). b) Absolute phase shift of system.

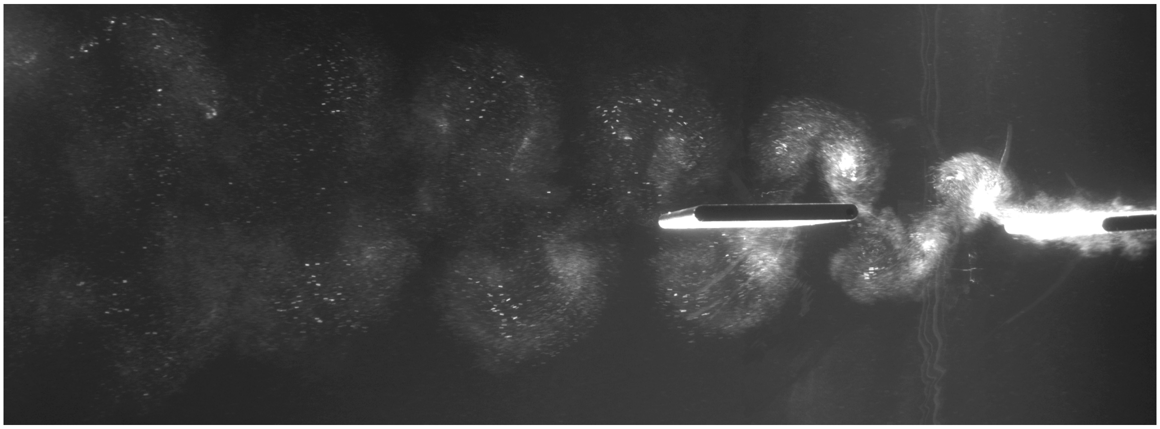

Figure 3.17: 2P wake coupling for $U_\infty = 0.4 m/s, f = 2.25 Hz, x/c = 1.5$.

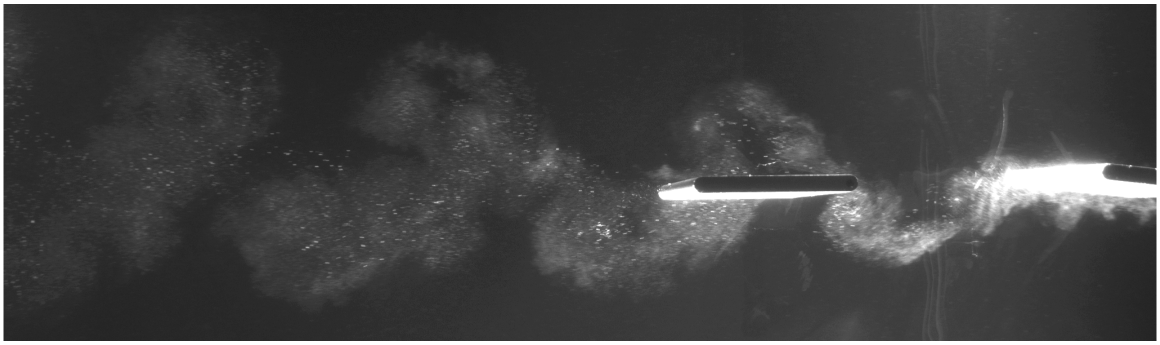

Figure 3.18: 2S wake coupling for $U_\infty = 0.4 m/s, f = 1.5 Hz, x/c = 1.5$.

mode is able to engender higher displacements from the downstream foil, explaining the drop in response seen at the location of the 2C island (See Section 3.3.1).

While the discontinuities in wake modes and corresponding non-linearities in fluid-dynamic response make a unique approximation for each system impossible, the fact that locally linear blocks are observed is quite promising. In fact, this indicates that the response of the downstream foil is linear, however, it is the forcing of the foil that is discontinuous. In order to separate the two, the defnition of a FRF given by Equation 3.4.3 needs to be modified. Once again, analyzing the present system with methods used for solid-mechanical systems may prove useful. A FRF can relate any SDOF system output to a given input. In a typical mechanical system, a FRF is often defined as

$$\left|\frac{X(t)}{F(t)}\right| = fn(\omega) \tag{3.4.4}$$

where $X(t)$ is the output variable response caused by a time-dependent forcing function $F(t)$. In a linearly elastic system for example, $X(t)$ would be the output displacement caused by an input force $F(t)$. In this system, a physics-based linear relationship between $F(t)$ and a measured input displacement $Y(t)$ could be established in the form

$$F(t) = fn(Y(t)), \tag{3.4.5}$$

which would allow a bijective transformation of the FRF to

$$\left|\frac{X(t)}{Y(t)}\right| = fn(\omega), \tag{3.4.6}$$

directly relating measured output displacements to measured input displacements. Displacement ratios as in Equation 3.4.6 are often the measured quantity in experiments of such systems and the forces are inferred from the relationship defined by Equation 3.4.5.

For the present hydrofoil system, measurements were in fact taken in the form of displacement ratios $|B/A|$, however, the relationship between the input amplitude A and the vorticity-mediated force F_v acting on the downstream foil is not explicitly defined. A modified FRF for this system would be of the form

$$G\left|\frac{A_2}{A}\right| = fn(\omega), \tag{3.4.7}$$

where

$$G = \frac{A}{F_v}. \tag{3.4.8}$$

Although a constitutive function such as G is not currently known, several of its properties can be qualitatively deduced. The first is that it is most likely discontinuous based on the discrete nature of the changes in wake modes. Furthermore, G is most likely a function of A, f, Re and x. Clearly, A, f, and Re are directly responsible for the number, form and strength of the shed structures, while x governs the effect of length and time scale phenomena such as vortex formation and dissipation. Some prelimenary work has been done by Schnipper et al.[68] on numerically specifying the wake transitions while several studies[62, 102] have calculated the circulation strength of vortical structures in various wake modes. This suggests that an understanding of these forces is possible. The effect of vortex formation, dissipation and interaction as structures are convected over time is the focus a great deal of research [103–106]. An important question is whether or not these variables show up in the FRF; i.e. do any of the variables of G fall out as a result of system dynamics?

As it has been observed that the wake structure throughout the domain of this study is a function only of A_D and St_D (see Section 3.3.3) and a linear system should prove independent of A, if the response of the system were a linear function only of the wake structure, the data should collapse into a function of St_D for each x—or perhaps two functions, one for the case above and one for the case below the flow separation threshold. Figure 3.19 shows the attenuation plots at each foil spacing x as a function of reduced frequency St_D for all cases above the separation threshold ($A \geq 11.25°$). It can be seen that the data collapse reasonably well for small foil spacing $x/c = 0.5$. However, the grouping becomes less coherent as downstream spacing x increases. To quantify the coherence, the MATLAB function `fit` is used to recursively fit a 4th degree polynomial (higher orders yield diminishing reduction of residuals) to each of these plots and the norm is given as

$$norm = \sqrt{\sum_{i=1}^{n} d_i^2}, \tag{3.4.9}$$

where d_i are the residuals (differences between data points and polynomial values). A lower value indicates a better curve fit. For $x/c = 0.5$, the norm is calculated as 34.242 while for $x/c = 5$ it is 127.98.

This shows that the foil spacing has a large effect on the response of the system, possibly due to dissipative effects as well as vortex interaction and breakdown. With increased spacing, the difference in time it takes for vortical structures shed at varying velocities to reach the downstream foil becomes larger. Increased time allows more viscous dissipation of energy and more interaction of adjacent structures. As this effect becomes greater with increased spacing, the data collapse using St_D becomes increasingly poor as seen in Figure 3.19. The fact that the response is primarily a function of St_D when x/c is small does indicate that perhaps Re effects appear only in a dissipative term of G. A possible explanation could be due to the fact that while circulation strength of the vortices shed from the upstream foil increases with U_∞^2[62, 68], so does the inertial fluid force resisting motion of the downstream foil. This would essentially negate Re effects on system response for terms other than dissipation.

3.4.3 FRF Approximation

In the regions where locally linear response is observed, various approaches to approximating system response are possible including a number of commercially available software packages—such as MATLAB's Robust Control Toolbox—which are capable of fitting models to measured data. For example, MATLAB's `fitfrd` function is discussed in the following section (3.4.4). First, a FRF approximation educed from the dynamics of the system and its observed behavior is examined.

For the FRF approximation, the dynamic system will consist of the downstream foil and the fluid surrounding it. It is modeled simply as consisting of a spring, mass and damper with a single degree of freedom as shown schematically in Figure 3.20. In this system, the foil is itself a rotating mass m, but the surrounding fluid is acting

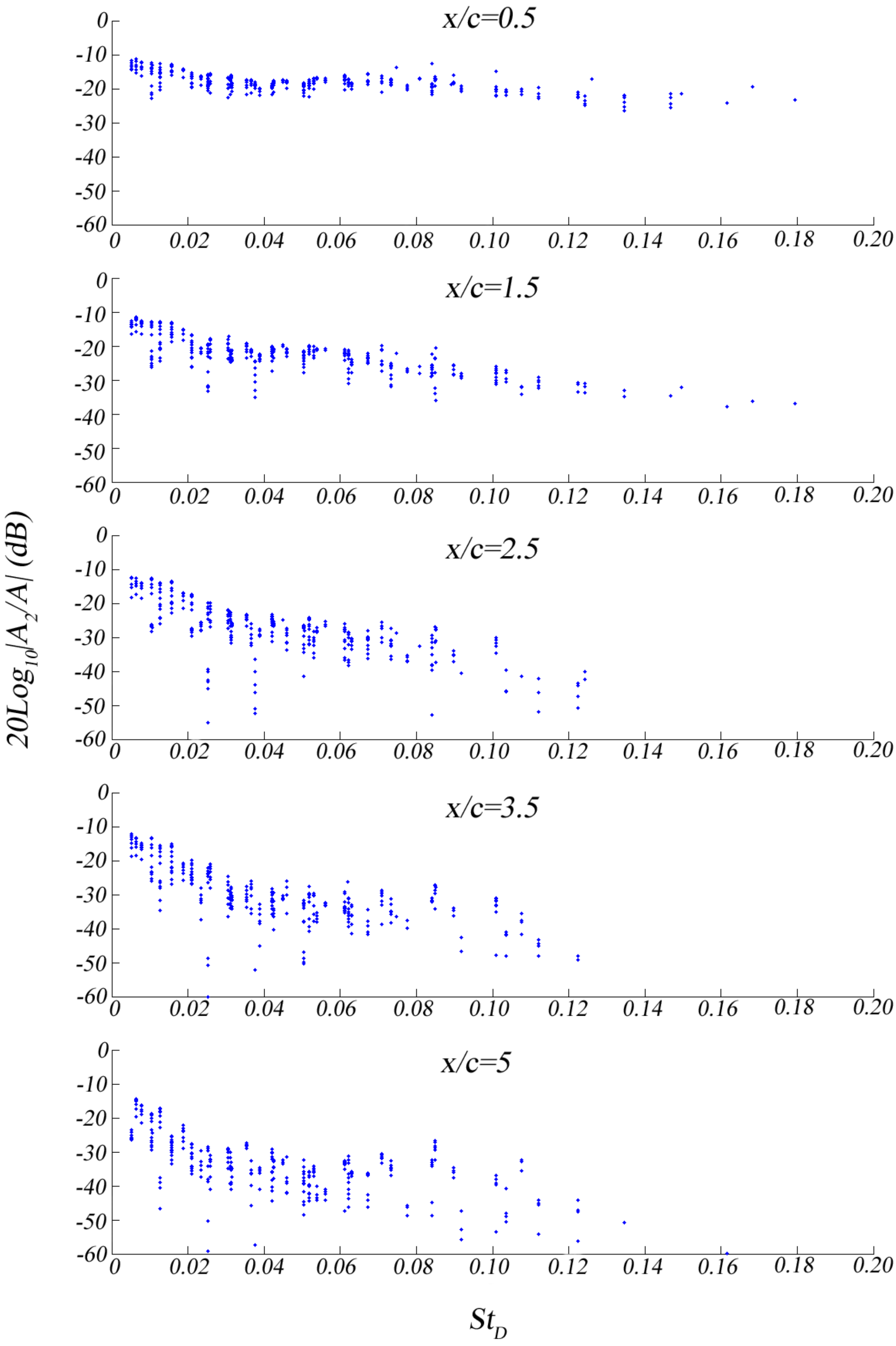

Figure 3.19: Sytem attenuation at each foil spacing x/c as a function of reduced frequency St_D.

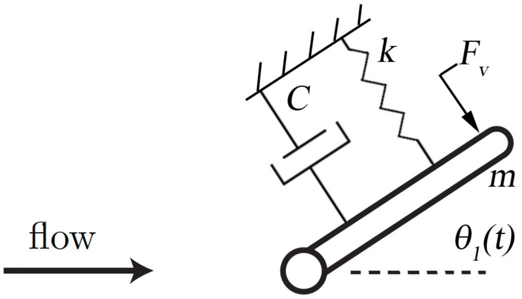

Figure 3.20: Schematic of foil system model for FRF approximation.

as the spring force, damping, and the excitation force. The fluid forces must be split into two components in order to anlyze the system. The streamwise fluid motion is considered to act as the spring force (the force centering the foil) and the oscillating, spanwise fluid motion caused by the shedding of structures from the upstream foil will be modeled as the excitation force F_v. First, the equations of motion are found for the undamped case by equating rotational forces as,

$$I_\circ \ddot{\theta}_2 = \tau_\circ, \tag{3.4.10}$$

where $\tau_\circ$ are the moments acting on the system and $I_\circ$ is the rotational mass moment of inertia,

$$\begin{aligned} I_\circ &= \int_V r^2\, dm \\ &= \rho_A \int_V r^2\, dV \end{aligned} \tag{3.4.11}$$

where ρ_A is the density of the aluminum foil. If we assume the width of the foil d to be small, then

$$\begin{aligned} I_\circ &= \rho_A s d \int_0^c r^2\, dr \\ &= \frac{1}{3} m c^2. \end{aligned} \tag{3.4.12}$$

The moment $\tau_\circ$ equates to the streamwise component of inertial fluid force acting on the foil as

$$\begin{aligned}\tau_\circ &= -\frac{c}{2}\int_A \rho_w U_\infty^2 \cdot \hat{\mathbf{n}}\, dA \\ &= -\frac{1}{2}c^2 s \rho_w \sin(\theta_2), \end{aligned} \tag{3.4.13}$$

where ρ_w is the density of the fluid (water). Gathering the terms yields

$$\frac{1}{3}mc^2\ddot{\theta}_2 = -\frac{1}{2}c^2 s\rho_w \sin(\theta_2), \tag{3.4.14}$$

which is the undamped equation of motion for the downstream foil. To obtain a useable approximation, the $\tau_\circ$ term needs to be linearized. Because the largest measured response amplitude θ_2 is less than 9°, excellent accuracy is acheived using a low order approximation. By expanding about $\theta_2 = 0$ such that

$$\sin(\theta_2) = \theta_2 - \frac{\theta_2^3}{3!} + \frac{\theta_2^5}{5!}\cdots \tag{3.4.15}$$

and ignoring higher order terms, Equation 3.4.14 becomes

$$\frac{1}{3}mc^2\ddot{\theta}_2 = -\frac{1}{2}c^2 s\rho_w\theta_2. \tag{3.4.16}$$

Rearranging and adding in the damping term C and the vorticity-mediated forcing F_v term yields

$$m\ddot{\theta}_2 + C\dot{\theta}_2 + \frac{3}{2}s\rho_w\theta_2 = F_v. \tag{3.4.17}$$

Assuming F_v(t) to be sinusoidal, Equation 3.4.17 represents a SDOF, forced-vibration system, with a spring coefficient of the form

$$k = \frac{3}{2} s\rho_w \tag{3.4.18}$$

and an undamped natural frequency of oscillation

$$\omega_n = \sqrt{\frac{\frac{3}{2} s\rho_w}{m}}. \tag{3.4.19}$$

A commonly used aproach[107] for a harmonically oscillating system such as this, assumes a solution of the form

$$\theta_2 = \Theta_1 e^{i\omega t}, \tag{3.4.20}$$

where Θ_1 and its derivatives

$$\begin{cases} \dot{\Theta}_1 = i\omega\Theta_1 e^{i\omega t} \\ \ddot{\Theta}_1 = -\omega^2\Theta_1 e^{i\omega t} \end{cases} \tag{3.4.21}$$

are substituted into Equation 3.4.17 to get

$$(-\omega^2 m + i\omega C + \frac{3}{2} s\rho_w)\Theta_1 e^{i\omega t} = F_v e^{i\omega t} \tag{3.4.22}$$

and resulting FRF function

$$\frac{\Theta_1}{F_v} = \frac{1}{(-\omega^2 m + i\omega C + \frac{3}{2} s\rho_w)}. \tag{3.4.23}$$

Finally, because $A_2 = fn(\Theta_1)$ and G (defined by Equation 3.4.8) relates A to F_v, the resulting complex FRF is

$$G \cdot \frac{A_2}{A} = \frac{1}{(-\omega^2 m + i\omega C + \frac{3}{2} s\rho_w)}. \tag{3.4.24}$$

In order to use Equation 3.4.24, the values of G and C must be determined from the data. As discussed in Section 3.4.2, G is not currently known, but for the present FRF it is simply a scalar coefficient function. The damping coefficient C is obtained by using *a posteriori* information regarding observed response of the system. It is observed that the response behaves like an underdamped system, and therfore a damped natural frequency ω_d can be deduced by finding the frequency where the maximum system response, $|A_2/A|$ is located. The damping ratio ζ and therfore the damping coefficient C can therefore be determined by using the relationships

$$\begin{cases} \omega_d = \omega_n\sqrt{1-\zeta^2} \\ \zeta = \dfrac{C}{\sqrt{2km}}. \end{cases} \tag{3.4.25}$$

One more operation must be made in order to properly analyze these systems. The measured absolute phase shifts need to be corrected due to the delay in time between the shedding of vortices and their interaction with the downstream foil. The measured phase shifts are first unwrapped using MATLAB code shown in Appendix B.2. The phase delay due to the spacial separation of the foils is then subtracted from the unwrapped absolute phase shifts as follows,

$$\begin{aligned} \phi_{corrected} &= \phi - \phi_{spacial\,delay} \\ &= \phi - N_p(mod\,p)\cdot 360^\circ. \end{aligned} \tag{3.4.26}$$

Here, the *mod* operator yields the remainder from division, and N_p is the number of oscillation periods between foils defined by

$$N_p = \frac{t}{p} \tag{3.4.27}$$

where t is the time it takes for a wave to travel between foils and p is the period of

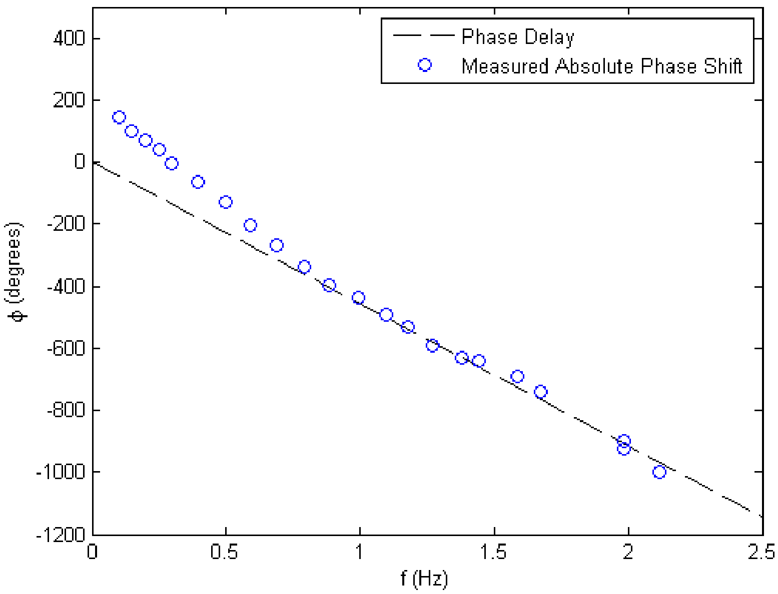

Figure 3.21: Absolute phase shift and phase delay for a system. $U_\infty = 0.5m/s$

the wave,

$$\begin{cases} t = \dfrac{x}{U_\infty} \\ p = \dfrac{1}{f}. \end{cases} \tag{3.4.28}$$

An example graph of a measured, unwrapped absolute phase shift and phase delay for a particular system in shown in Figure 3.21.

Because G is unknonwn, the FRF in Equation 3.4.24 can currently be used only for one of the linear blocks where there is not a step change in the system response. For example, at $U_\infty = 0.5m/s$, the reduced frequency remains low enough throughout the tested domain that the foil does not transition to thrust or display a 2P wake mode. Approximations using the FRF in Equation 3.4.24 are shown for two spacings at $U_\infty = 0.5m/s$ in Figure 3.22. It can be seen that the FRF approximation is reasonably good for this configuration, accurately modeling both the attenuation and phase shift. In fact, it is found that for every tested block without discontinuities, this approximation method works quite well, once again indicating that the response of the downstream foil is linear.

3.4.4 Model Fitting using MATLAB's Robust Control Toolbox

The `fitfrd` command in MATLAB's Robust Control Toolbox fits frequency response data with a state-space model of specified order. The data must be given in the form of a complex system response which incorporates the response magnitude $|\theta_2/\theta|$ and phase shift ϕ (in rad/s). Once the state space model is obtained, a transfer function can be specified. For instance, Figure 3.23a depicts the frequency response of the system ($U_\infty = 0.3m/s.x/c = 1$) with transfer funtion

$$\frac{\Theta_1(s)}{\Theta(s)} = \frac{.057s^6 - .0091s^5 + .89s^4 - .67s^3 - .076^2 - .067s + .010}{s^6 - 1.3s^5 + 5.1s^4 - .84s^3 + 1.1s^2 + .10s + .066}. \tag{3.4.29}$$

The order of this model was chosen to allow the magnitude and phase plots to follow the (graphical) nonlinearities in the experimental data as shown, and in fact, a higher-order model could be generated to follow these nonlinearities arbitrarily closely. Figure 3.23b depicts the response of the same system with transfer function

$$\frac{\Theta_1(s)}{\Theta(s)} = \frac{-.050s^5 - .74s^4 - 3.5s^3 - 5^2 - 2s - .19}{s^5 - 10s^4 + 24s^3 - 16s^2 + 3.2s - .21}. \tag{3.4.30}$$

The magnitude and phase curves for this system follow the best-fit lines passing through the experimental data.

It is observed that `fitfrd` works well for certain systems—for instance, those that appear *graphically* linear in nature—but often obtains poor model fits. Perhaps the fact that it does not take into account any knowledge of the physical system could explain why this is the case. For instance, any small errors in data can bias the fit of the resulting transfer function, whereas a model employing knowledge of the system, such as the one described in the Section 3.4.3, naturally weights data that conform to a physical model .

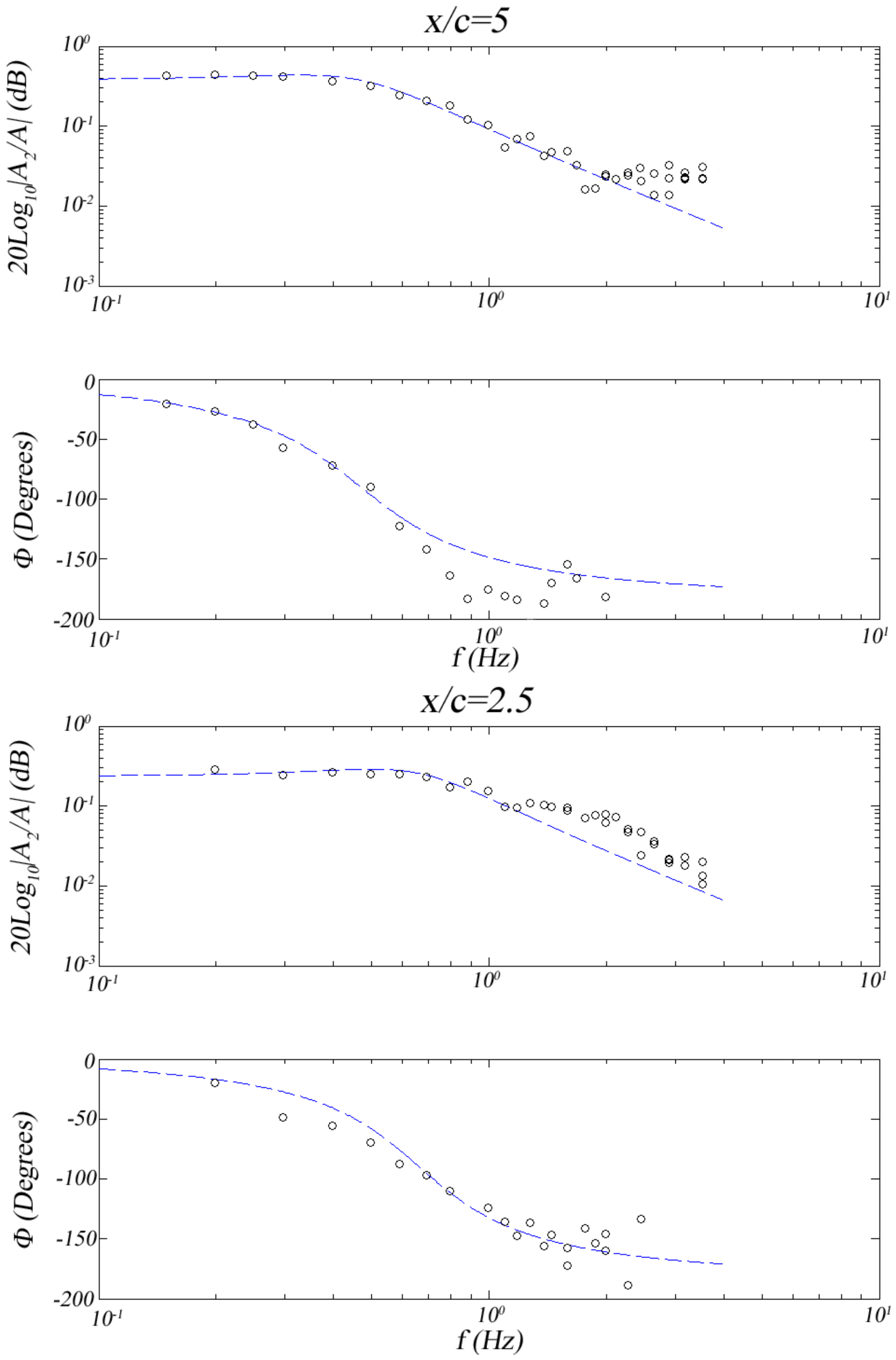

Figure 3.22: Linear approximation of system. The dashed lines are the response calculated by the FRF in Equation 3.4.24 and the circles are measured data points. Phase shift data points are corrected for phase delay. $U_\infty = 0.5m/s, A = 15°$

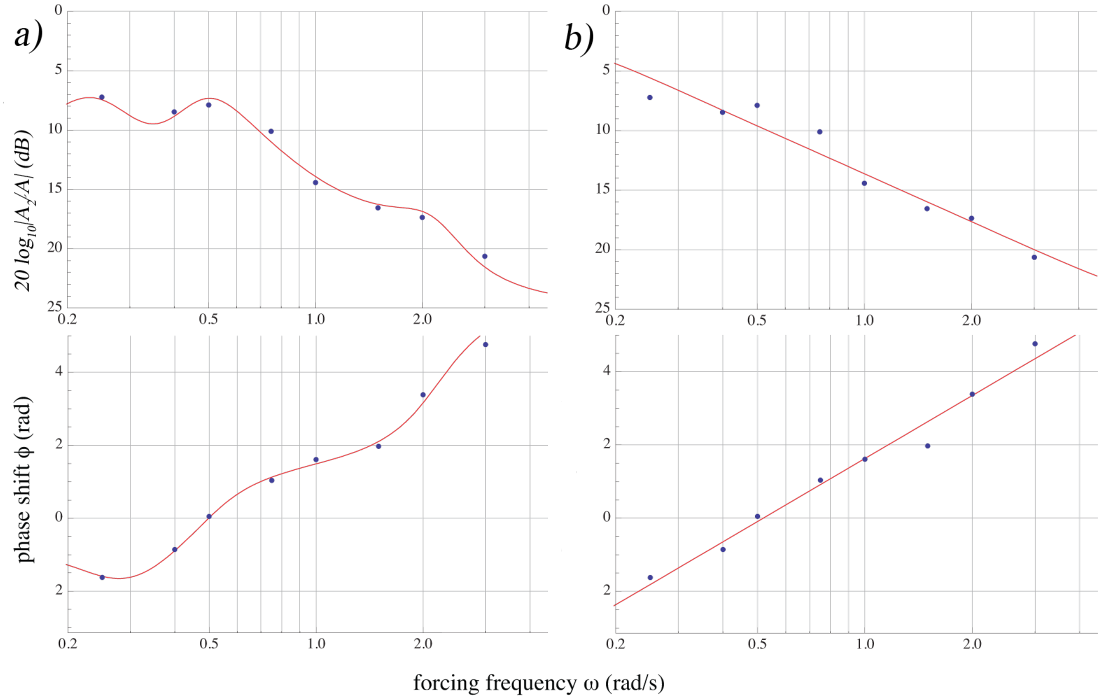

Figure 3.23: Transfer functions obtained using MATLAB's `fitfrd` command for $U_\infty = 0.3m/s, x/c = 1$.

3.5 Three Foil System

The possibility of combining linear coupling models into a large network exists only if the inter-agent couplings maintain linearity while interacting *en masse*. A preliminary exploration is carried out by placing three foils in tandem (see Figure 3.24) and observing the behavior of the two passive foils while the front foil is forced in the same manner as the previous experiment. The tested configurations consist of the rear foil (furthest downstream) located at $x/c = 5$ and the middle foil located

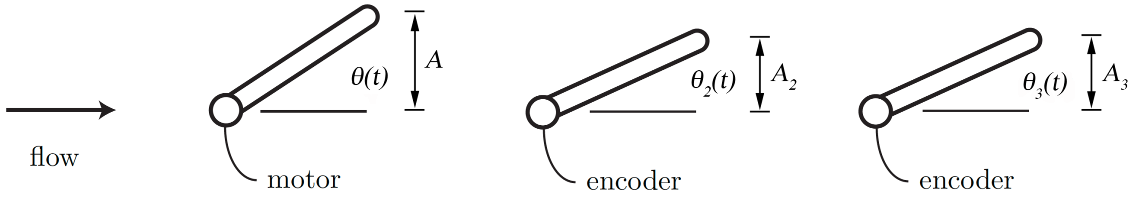

Figure 3.24: Schematic of three-foil experimental layout.

at intermediate spacings between the front and rear foils. Six intermediate spacings are tested at $U_\infty = 0.5m/s$ and $A = 15°$. The first observation is that the middle foil has the same frequency response $|A_2/A|$ with or without the rear foil in place for all configurations tested. This indicates that there are no significant dynamic effects which propagate upstream in such a network. This may or may not be true in a substantially larger group or one in which the downstream agents interact with nearby solid boundaries.

The second observation is that the coupling between the front and rear foils maintains linearity. Figure 3.25 shows the frequency response of the rear foil to the forced oscillations of the front foil $|A_3/A|$ with and without a passive middle foil present. With a middle foil located at any x/c, the response of the rear foil is the same; in particular the response has an approximately 50% reduction in magnitude and a constant absolute phase shift, $\phi \sim 200°$ compared with the case when no middle foil is present. The constant phase shift found in these experiments corresponds to the resulting phase shift obtained by subtraction of one chord length c from x in Equation 3.4.28. Thus, the middle foil has no effect on the corrected phase shift (see Equation 3.4.26) of the rear foil, and the resulting absolute phase shift is equivalent to moving the rear foil one chord length closer to the front foil. Additionally, the reduction of the response $|A_3/A|$ by 50% means that the response between the middle and rear foil is approximately constant at

$$\left|\frac{A_3}{A_2}\right| = 2 \tag{3.5.1}$$

indicating that there is no significant modification of the wake. These findings imply that an intermediate passive foil does not change the nature of the coupling between the foils, it simply extracts energy from the system.

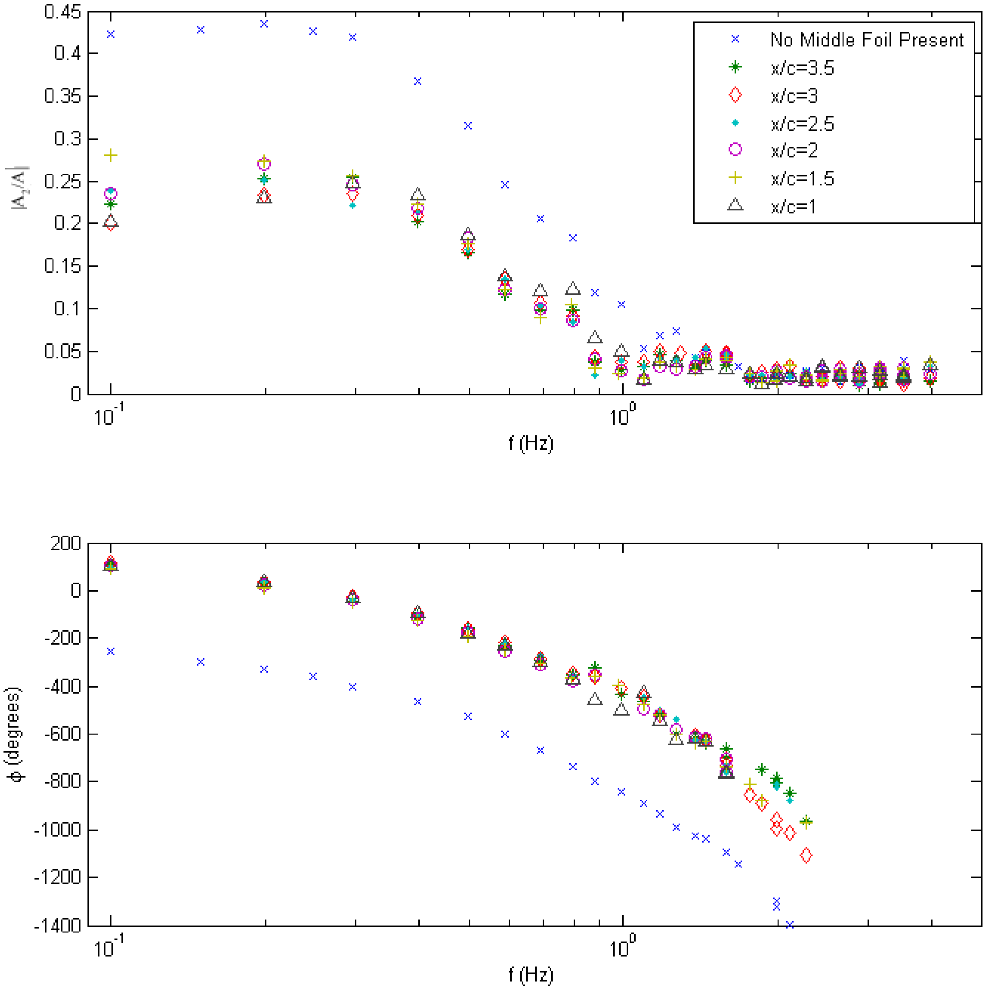

Figure 3.25: System response and absolute phase shift shown for rear foil with and without a middle foil present. The markers in the legend indicate the downstream location of the middle foil. $U_\infty = 0.5m/s, A = 15°$.

3.6 Summary

In order to take advantage of the vorticity-mediated, fluid-dynamic coupling inherent in large multi-agent systems, an understanding of the coupling between adjacent bodies is necessary. An experimental study of the dynamic coupling between oscillating, finite-span hydrofoils in tandem is carried out. An upstream foil is forced to oscillate periodically while a foil downstream oscillates passively as it encounters the shed vortical structures from the upstream foil. Hydrogen bubble flow visualization is employed to examine the strucutre of the wakes generated by the foil and identify the transitions in wake structure that occur as the input parameters are changed. The frequency response of the system due to vorticity-mediated forcing is examined by measuring the angular position of both foils with encoders.

BvK, reverse-BvK, 2S, 2P, and 2C wake modes are observed as well as several hybrid modes including a 2P + 2S wake. The wake modes prove to be independent of Re for the range tested in the present study; the modes are found to be a function only of their location in the A_D-St_D plane. While the flow past a finite-span foil is three-dimensional, visualization data in the mid-span plane show that the occurance of wake modes in the A_D-St_D plane as well as their transition locations correspond well with previous studies of two-dimensional oscillating foils. This indicates that some of the analytical tools used for two-dimensional analyses may apply to finite-span foils. Furthermore, the transition from drag to thrust—as indicated by the BvK/reverse-BvK boundary—is found to occur for $0.22 < St_A < 0.28$ which coincides both with the optimal cruising range observed for aerial and aquatic animals, as well as the noted drag-thrust transition for planar hydrofoils.

For each system tested (consisting of a unique $U_\infty - x$ configuration) the frequency response of the downstream foil is found to display linearity either a) for the entire range of forced amplitudes, or b) for discrete ranges of amplitudes. The bifurcations in system response are a direct result of abrupt transitions in the topology of the wake structures shed from the upstream foil. The most significant transition is found at lower frequencies when flow separation from the leading edge of the foil is found to occur at $A \geq 11.25°$; a bifurcation is seen at this amplitude for nearly all tested systems. Changes in system response are also noted for “islands” in the A_D-St_D plane where 2C wakes are present.

The linear nature of the system with respect to wake structure indicates that the response of the passive foil to the forcing caused by the wake is, in fact, linear within the range of conditions tested. A relationship between the motion of the upstream foil and the magnitude of the force its wake imparts on the passive foil—as expressed by G in Equation 3.4.8– is, however, unkown. Two frequency response approximations are explored, including a frequency response function derived from a physical model of the system as well as a transfer function fit using MATLAB’s Robust Control Toolbox. It is found that the approximation derived from a physical model can accurately represent the system response with the system damping and scalar value of G determined *a posteriori* from the data. MATLAB’s `fitfrd` command can yeild a good model fit, but fails to adapt to certain system configurations, for instance those with graphical non-linearities. Future studies are required to address the specification of the constitutive relationship G if a complete model is to be determined.

Finally, a brief study is carried out with three foils in tandem to explore the nature of the coupling with an additional system agent. If local coupling models are to be combined for large multi-agent systems, the coupling must remain linear between adjacent members as the system interacts in the large. For the tested configuration, it is found that with a passive foil located anywhere between the front and rear foils, the response remains linear; a constant absolute phase shift as well as constant-multiple decrease in magnitude is observed. Interestingly, the constant phase shift is found to be equivalent to decreasing the distance between front and rear foils by one chord length. Additionally, it is noted that the constant response between the middle and rear foils (i.e. $|A_3/A_2| = constant$) indicates that the passive middle foil does not alter the wake, but merely extracts energy from it.

3.6.1 Future Work

The most important area requiring further study is the determination of the constitutive function G. Either a deterministic calculation from first principles or an accurate model derived from experimentation is required to make the linear system model predictions useful in practice. More detailed experimentation specifically targeted at extracting this function may provide insight into the physics which govern it.

In addition, further study on the effect of foil configuration is suggested. The present study looks only at foils in tandem (aligned in the same streamwise axis), however, the effect of offsetting or staggering foils may change the dynamics significantly. A systematic experiment examining the efffect of spanwise offset is required.

Ultimately, it is hoped that the low order models discussed in this thesis can be extrapolated and applied for large systems of significantly higher complexity. Testing of these models against, e.g., systems with more degrees of freedom and larger numbers of agents will show if they hold for “real-world” applications.

CHAPTER 4: NASCAR COT CASE STUDY

4.1 Background

The NASCAR Sprint Cup series is a widely viewed form of automobile racing in the US with a fan base of approximately 75 million. After a number of dangerous and even fatal accidents, NASCAR decided to design a new racing vehicle which culminated in the Car of Tomorrow (COT) in 2007. It was designed by NASCARs Research and Development Center to replace the previous car used in the series and improve upon safety, performance, competition and cost efficiency for the teams[108]. The COT must drive at high speeds (over 300 kph) and in close proximity to other vehicles which made aerodynamics play a large part in its design and development. Along with an entirely new chassis and body, the COT implemented two new aerodynamic features which included a front, bumper-mounted splitter and a rear, deck-mounted wing, whereas the previous vehicle (popularly known as the Car of Yesterday or COY) employed a rear deck-mounted spoiler only. Both of these new features were intended to generate downforce. While the COT successfully achieved most of its design goals, it was found to have a serious safety issue under extreme yaw (near 180°). When turned around backwards as it might during a crash, the COT was prone to generating lift which could cause the car to rise off the ground and flip. This problem had existed in the COY, and a robust device known as a roof flap was already put in place to counteract it. Roof flaps act similarly to aerodynamic spoilers used on aeroplane wings and should not be confused with wing flaps. Roof flaps (shown in Figure 4.1) are passive aerodynamic devices that consist of flat plates located at the rear of the vehicle's roof which are hinged at the front edge. Under normal driving conditions,

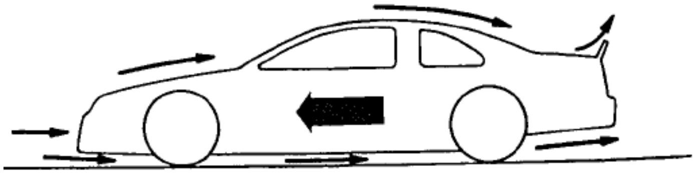

Roof Flaps Closed In Forward Motion

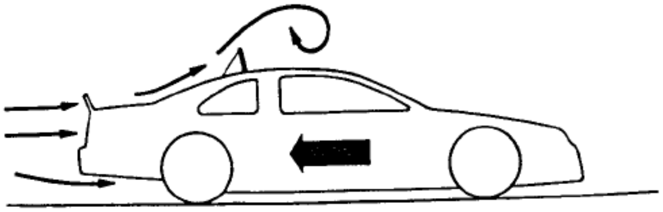

Roof Flaps Open In Extreme Yaw

Figure 4.1: Illustration of roof flap function on (pre-2007) COY from the original design paper by Nelson et al.[109]. The COY was fitted with a lip spoiler as shown above and flow is from left to right (car travelling right to left).

the flow over the roof keeps the roof flaps down; however, when turned at extreme yaw, low pressure is intended to pull them up into the oncoming air. When extended into the air, the roof-flaps increase drag and spoil the lift over the vehicle[109] in much the same way as spoilers on a landing airplane.

The roof flaps were carried over to the COT, however, as has been observed in various media sources, they did not seem to function consistently or deploy quickly enough to prevent the flipping problem in many cases. Due at least in part to this problem, NASCAR recently replaced the wing with a deck-mounted spoiler similar to the one employed on the COY. Figure 4.2 shows an image of both a wing and spoiler affixed to the COT. With the spoiler car (SC) in use for the 2010 season, the flipping problem has not occurred. There are primarily two speculative arguments being made about the cause of the problem for the winged car (WC), neither of which has been substantiated by credible experimentation or simulation. The first is that the wing itself creates increased lift over the spoiler when in reverse while the second argument places the blame on the ineffectiveness of the roof flaps on the WC. There is a clear

Figure 4.2: Image of the COT fitted with a spoiler (top) and wing (bottom). From [110].

lack of a) scientific justification for either explanation b) a physical understanding as to why the roof flaps might not function consistently with the wing or c) proof that there is in fact a greater tendency for the WC to lift.

Both NASCAR as well as independent teams have studied these vehicles, using experimental and computational testing, however, the scope and results of these tests have often been proprietary. The experimental studies conducted by NASCAR, to the authors knowledge, were restricted to wind tunnel measurements of force coefficients and on the determination of critical spin angle at which the roof flaps deploy. The roof flaps were found to deploy consistently in wind tunnel tests at relatively low yaw angles (below 90°) and thus it was assumed that tests at extreme yaw were unnecessary. However, these tests were carried out on a wind tunnel turntable that turns orders of magnitude slower than real racing situations. In real racing conditions, the yaw rate is often very fast during a wreck and the roof flaps may not have time to overcome inertial effects in the low to mid yaw range before reaching an extreme yaw position. Additionally, Nelson et al.[109] found that on the COY, the flow reattached to the roof (creating lift condition) only beyond 110° yaw, which indicates that a similar phenomena might occur for the COT.

In the open literature, independent teams have carried out flow visualization on these vehicles using smoke sheets in wind tunnels as well as through the use of complex wake imaging systems[111]. Many experimental studies have been done on the basic aerodynamics of the COY and similar types of race cars such as those done by Laise and Bayless[112], Duncan[113] and Leuschen and Cooper[114]. Others have discussed these characteristics in related studies such as Nelson et al.[109] in their paper describing the development of the roof flap design or Landman[115] in his study of road simulation for NASCAR vehicles in wind tunnels. In a bluff body wake generator study of the COY, Dominy and LeGood[116] claim many of the wake characteristics should be the same for the COT, however, they found that the flow structures in the wake were primarily the result of vortices shed from the spoiler. Additionally, several computational studies have been carried out on NASCAR vehicles to describe the fundamental flow. Duncan and Golsch[117] performed a CFD study on a 2003 Pontiac NASCAR race car, while Singh[118] carried out CFD analyses on a winged COT to study the effects of a rolling road surface and rotating wheels. It is fair to say that many of the basic characteristics of the flow around this type of car are well understood, however, the specific differences between the wing and spoiler—particularly at extreme yaw—have yet to be described.

While a full scale test at an air speed of $\sim 80m/s$ (typical car speed in race) would yield the most accurate results, given the constraints due to the flow rate and cross-sectional area of the water channel facility at the University of North Carolina at Charlotte, the present study is restricted to a 10% scale model at a maximum water velocity of $U_\infty = 0.7m/s$. The effects of Reynolds number are discussed in Section 4.2.1. This paper qualitatively compares flow past a wing and spoiler mounted to a COT model in order to evaluate the performance and safety of these two devices at zero and 180 degrees of yaw. 2D PIV is employed to visualize the flow and identify structure topology. Results pertaining to the zero yaw case can be used to compare the performance and safety benefits for these devices on the COT under normal operating conditions and can likely be considered for comparison of a wing and spoiler mounted to other types of race vehicles. Results at 180° yaw help to analyze the interaction of these devices with the roof flaps employed on the COT and investigate a possible cause for their inconsistent deployment. Although the wing is no longer employed in the NASCAR racing series (and therefore may be of little interest for that community), this is a very interesting problem from a fluid dynamics perspective. This study seeks to understand the observed flow phenomena and to provide insights for future designs both in the NASCAR racing series and any form of motorsport where a similar system may improve safety.

4.2 Experimental Methods

Experiments are carried out in a closed-loop, open-top water channel with a test section $1m$ deep x $1m$ wide yielding a maximum solid blockage of less than 3% based on a frontal projected area of $0.0285m^2$ for the tested models. However, given the free surface at the top of the channel, the effective blockage ratio is expected to be even lower. The standard selection for the characteristic length in the motorsports industry is the wheelbase of the vehicle, however the projected height of the vehicle is a more important scale for aerodynamics. Reynolds numbers derived from both wheelbase

Table 4.1: Reynolds number comparison.

	COT at 185 *mph* in Air	COT at 130 *mph* in Air	10% Scale Model at $0.70m/s$ in Water	10% Scale Model at $0.50m/s$ in Water	10% Scale Model at $0.25m/s$ in Water
Re_w	1.53×10^7	1.07×10^7	1.96×10^5	1.40×10^5	6.99×10^4
Re_h	7.37×10^6	5.18×10^6	9.42×10^4	6.73×10^4	3.37×10^4

Figure 4.3: 10% scale models of COT with wing (back) and spoiler (front). The models are translucent, thermoformed poylcarbonate, but a temporary powder coating is applied for the photograph.

and vehicle height will be included and referred to as Re_w and Re_h respectively. Two models, shown in Figure 4.3, are examined at yaw angles of zero and 180° at Re_h of 3.37×10^4 (Re_w: 6.99×10^4), 6.73×10^4 (Re_w: 1.40×10^5), and 9.42×10^4 (Re_w: 1.96×10^5) based on a kinematic viscosity of water at 20° C of $10^{-6} m^2/s$ and mean free stream velocities of $0.25 m/s$, $0.50 m/s$ and $0.70 m/s$. Table 4.1 shows Reynolds numbers tested in the present study as well as standard velocities used in wind tunnel tests for comparison. The Reynolds number dependence of turbulent structures—specifically flow separation and reattachment—is an ongoing debate. Evidence from published data suggest it is, to a large extent, dependent on the geometry of the test object. Detailed discussion of this dependence is given in Section 4.2.1.

A schematic of the experimental setup is shown in Figure 4.4. Laser light travels down the periscope, which is located approximately 7 car lengths downstream of the model, and is split into a vertical, spanwise sheet. The laser sheet is centered on the model and illuminates the front, top and rear of the model as well as a small portion of the underbody. This large coverage area is facilitated by use of transparent models and allows for optical measurements upstream of the vehicle. The model vehicles

(Figure 4.3) are thermoformed, clear polycarbonate shells mounted to stainless steel bases. These 10% scale models are 510mm x 190mm x 150mm (length x width x height). The models are inverted in the tunnel to allow future force measurements using un-submerged load cells. The underside of the bodies are suspended/supported by two thin stainless vertical steel plates, which are only 1.5mm wide (<0.3% CL) in the spanwise direction and therefore should not have a significant effect on the underbody flow and trailing wake. Both models have the same geometric properties; however, one model has a wing affixed to the rear deck lid (WC) while the other has a spoiler (SC). On the WC model, the wing does not include endplates which are used in the actual COT because only the center plane is being analyzed and these should not have a significant effect. The exclusion of endplates allows a more complete profile view of the wing for the camera. Additionally, the chord of the rear-pivoting wing on the COT is adjustable between 0° to 16° from horizontal. In this study, the models wing is fixed at the (race typical) maximum 16° angle of attack.

The PIV system consists of a double-head Nd-Yag Laser employing a submerged laser light periscope, timing controlled CCD camera, synchronizer, and computer for control and post processing. The maximum output energy of the Nd-Yag laser is 1200mJ with a double wavelength of 512nm and 1064nm and a pulse duration of 4ns. The CCD camera has 2048 x 2048 pixel resolution. The mean thickness of the vertical laser light sheet is 2mm which is approximately 0.4% of the characteristic length (CL) of the model. The seeding particles are silver-coated hollow glass spheres with a mean diameter of 10 microns.

For the two dimensional, time-averaged analyses, a single camera is used and 500 PIV realizations are generated at 7.4Hz with the time step between images in each pair set at 3000μs (0.003s). Image correlation is done through an adaptive Fast Fourier Transform (FFT) based algorithm using Dynamic Studio v3.14 software. A measurement plane scale of 62.8 pixels/mm, interrogation areas of 16 x 16 $pixels$,

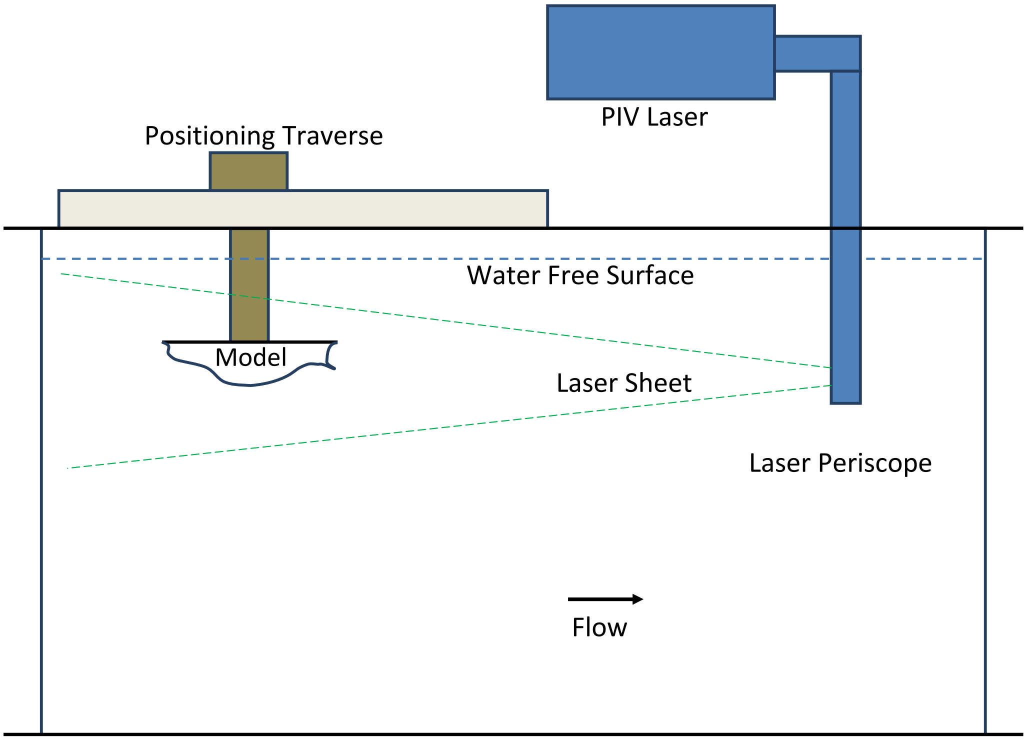

Figure 4.4: Schematic of 2-D PIV experimental setup. Not to scale.

25% overlapping, an initial interrogation area of 64 x 64 *pixels*, central offset, and two-step refinement is used. Spatial calibration is achieved using a scaled target in the laser sheet plane. The spatial resolution of the velocity vectors in the measurement plane is approximately 3.925 vectors/mm corresponding to one vector every 0.77% CL.

4.2.1 Reynolds Number Dependence of Wake Structure

The question may be raised as to the validity of testing at Reynolds numbers which are different from real operating conditions. As Table 4.1 shows, the tested Reynolds numbers are two orders of magnitude lower for this study than those in the full-scale case. Flow structure analysis in low-speed water channels is found to be an effective tool for examining complex aerodynamic flows[119] and although these tests are necessarily carried out at Reynolds numbers much lower than actual operating conditions, certain flows show insignificant Reynolds number dependence. According to Cobleigh and Frate[120], "phenomena such as vortices and their generation, interaction and breakdown are in this category and are ideally studied in a facility such as a water tunnel." Erikson[119] notes that although separation shows Reynolds number dependence, the basic structure of vortices is similar regardless of Reynolds number. However, the Reynolds number dependence of the sparation bubble has been shown to diminish beyond certain Re thresholds; for example, in the case of a forward-facing step, the recirculation step appears to be independent of Reynolds number for $Re > 8500$[121]. For fully developed flows, experiments done in other water channels have proven to be qualitatively accurate when vortical flows are more dominant than the viscous flow effects[120]. Additionally, data obtained from NASAs water tunnel visualization studies on models as diverse as combat aircraft and gurney flaps have shown excellent correlation with tests in wind tunnel and real-world experiments at Reynolds numbers that are two or more orders of magnitude higher[120, 122, 123]. A "universal mixing transition" for turbulent flows is proposed to occur at a minimum

Re of 10^4[124], however there is great difficulty in selecting the proper characteristic length for external aerodynamics when compared to somewhat more intrinsic scales for shear flows. In the present study, the Re independence observed in the overall flow characteristics (wake size/shape, separation/attachment points etc.) suggest this transition has been reached (with the important exception of the local transition observed in the WC under extreme yaw as discussed in Section 4.4.2).

4.3 Zero Yaw

It is important to first compare the two aerodynamic devices under normal operating conditions (i.e. zero yaw). Figure 4.5 shows the mean flow streamlines past the models and Figure 4.6 shows the mean velocity maps for the same configuration. Note that, for all figures in this paper, flow direction is from right to left. No discernable Re dependence was observed in the wake structures for the zero yaw configuration, and thus figures are shown for only one case ($Re_h = 3.37 \times 10^4$). While there are some striking differences in the flow topologies between the WC and SC, the over-body flow up to the backlight region, as well as the lower portion of the wake is similar in both cases. The overall size and shape of the wake are comparable in both cases and are consistent with the wakes observed in previous studies such as[113, 116].

As a result of the models underbody geometry, the flow issuing from below the rear fascia can be thought of as 2D plane jet which is known to shed a rolling vortex (see [125] for example) in the lower portion of the models wake. The lower region of the wake for both models is characterized by a clockwise vortical structure with foci in similar locations. This indicates that, in the central plane of the vehicle, neither the wing nor the spoiler has a significant effect on the lower portion of the wake.

The difference in topology between the two models can easily be seen in the upper region of their wakes. This region of the SC is characterized by a large counterclockwise vortical structure shed from the tip of the spoiler, while the WC is characterized instead by a mixing layer. Although the mean velocity fields describe the nature

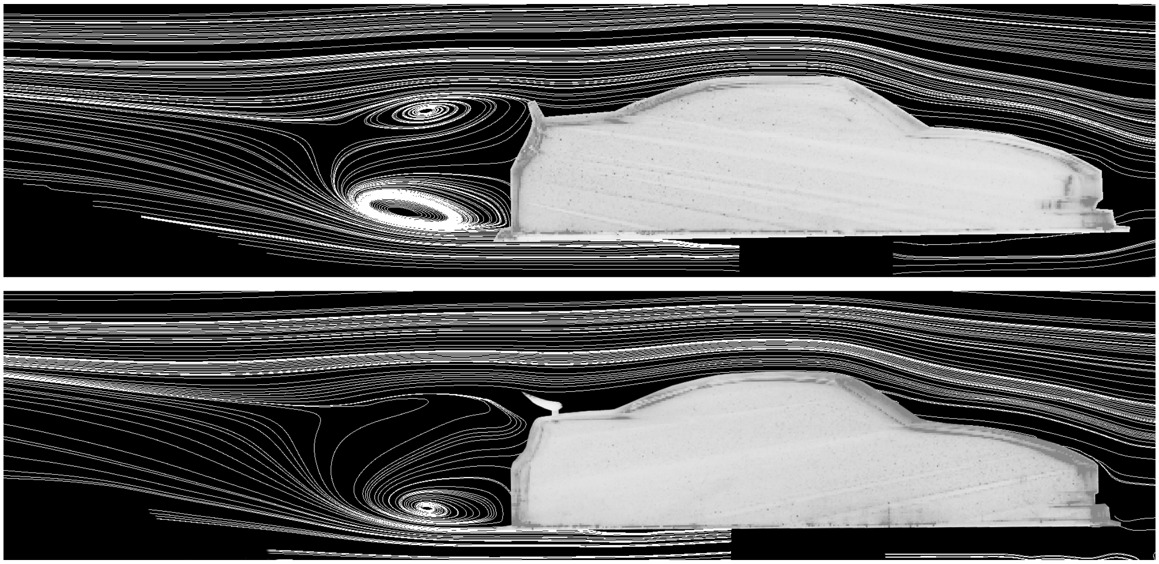

Figure 4.5: Streamlines showing mean flow past SC (top) and WC (bottom) at zero yaw, $Re_H = 3.37 \times 10^4$.

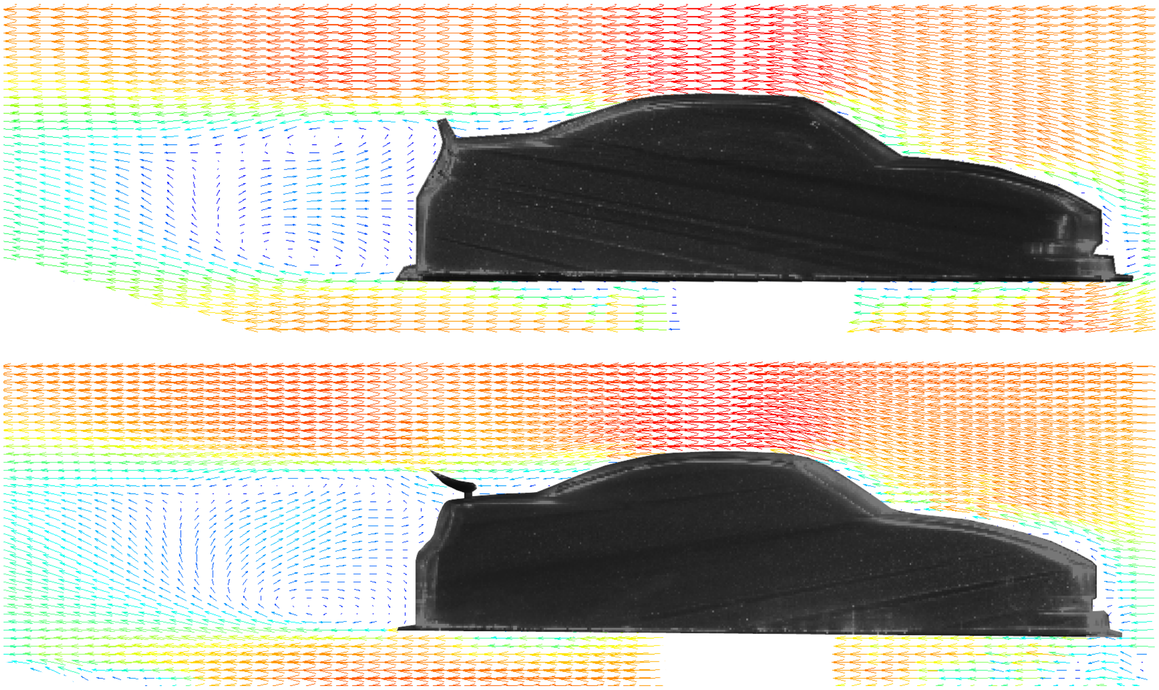

Figure 4.6: Ensemble averaged velocity maps of wake region for SC (top) and WC (bottom) at zero yaw, $Re_H = 3.37 \times 10^4$.

of the flow, they only yield direct information about flow structures with essentially infinite time scales. A typical instantaneous vector field in the wake is shown for both models in Fig. 4.7 which illustrates the nature of eddies in this region, and a Galilean decomposition—in which half of the free stream velocity is subtracted from the velocity field—is shown in Fig. 4.8 which is slightly more representative of a moving car in a stationary flow field. The latter provides a view of the vortical structures which are convecting downstream at the boundary of the wake. Both the vortices in the wake and those travelling downstream are important when considering the ambient conditions through which a trailing vehicle must drive. A qualitative observation suggests that the time and length scales of the structures inside and at the boundary of the WC wake are significantly smaller than those in the SC. This should yield significantly different racing performance characteristics for groups of these vehicles. The wing should create less disruption to the handling characteristics of vehicles trailing closely behind (as is common in racing) because the smaller scales in the WC wake yield more consistent downforce as a function time with smaller magnitude deviations in force compared to the SC.

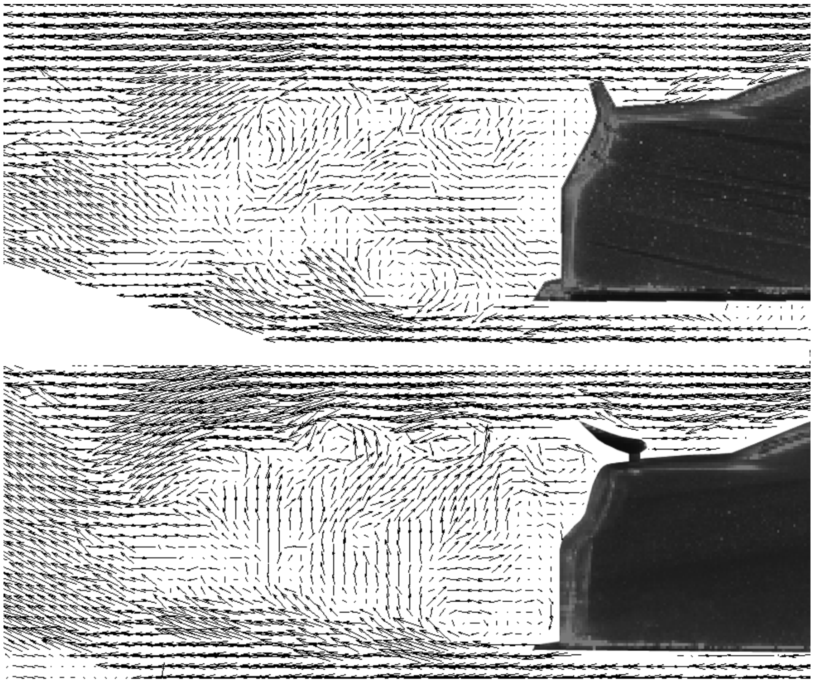

Figure 4.7: Instantaneous velocity field in wake of SC (top) and WC (bottom) at zero yaw and $Re_H = 3.37 \times 10^4$.

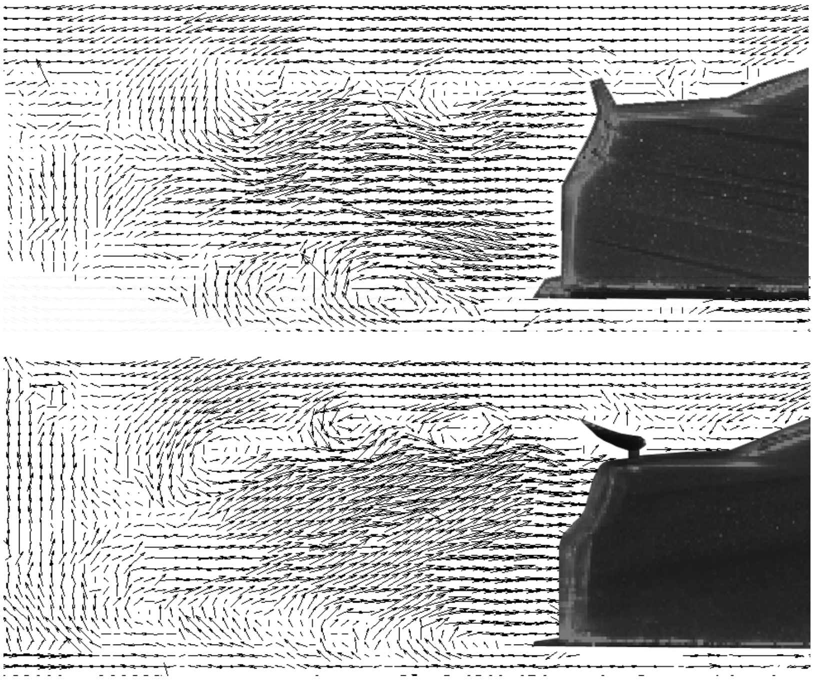

Figure 4.8: Instantaneous velocity field in wake of SC (top) and WC (bottom) at zero yaw and $Re_H = 3.37 \cdot 10^4$ with $0.5U_\infty$ subtracted, i.e. a closer representation of a moving car in a stationary flow field.

4.4 Extreme Yaw

Examining the flow in an extreme yaw configuration, the primay concern with is interaction of the roof flaps with the wake from the wing or spoiler. Section 4.4.1 discusses this interaction and Section 4.4.2 provides a preliminary analysis of the flow structure and development.

4.4.1 Roof-Flap Interaction with Wake at Extreme Yaw

Figure 4.9 shows mean streamwise velocity profiles at four locations along the rear of the SC and WC at $Re_h = 3.37 \times 10^4$ and 180° yaw. The leftmost location corresponds with the rear edge of the roof flaps. It can be seen that the separated flow region past the spoiler persists in the streamwise direction over the roof flaps and the flow remains unattached at this point. Although the fluid-structure interaction can be quite complicated, the low-pressure separation wake over the roof should be the primary mechanism by which the roof flaps are deployed. In this case, the reverse flow over the SCs roof indicates that the wake extends over the flaps and suggests that they would be drawn open and function correctly. Conversely, flow over the WC appears to be reattached before the rear edge of the roof and therefore is attached at the location of the roof flaps. This indicates that the low pressure wake does not extend over the flaps and implies that the flaps may not function consistently under these conditions. It can also be seen that the earlier reattachment of the flow on the WC leads to increased fluid momentum over the roof and a corresponding increase in lift generated by the wing-effect of the vehicles profile.

The mean velocity maps shown in Figure 4.10 correspond to the velocity profiles in Figure 4.9. They indicate the topology of the structures in the separated region and are consistent with the above analysis. While it was already shown that the flow on the WC is reattached in the mean, is also important to comment on the time-dependent nature of the flow. While both models have a large separation wake over the rear deck and backlight, the turbulent motions of their wakes fluctuate quite differently.

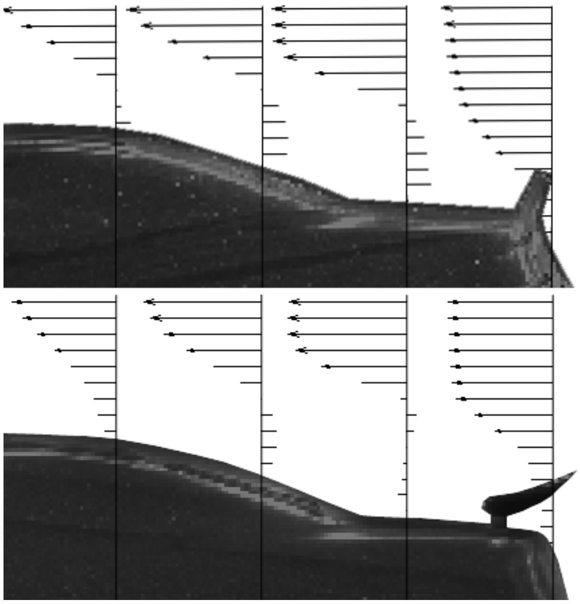

Figure 4.9: Streamwise velocity profiles at four locations for SC (top) and WC (bottom) at 180° yaw and $Re_H = 3.37 \times 10^4$. Leftmost profile location corresponds to rear edge of roof flap.

Typical instantaneous velocity maps are shown in Figure 4.11 for $Re_h = 3.37 \times 10^4$ for the SC and WC. The instantaneous maps identify structures with non-infinite time scales and provide more insight into these flows. The spoiler continuously sheds vortices which roll down the length of the roof in a periodic manner. The velocity snapshot for the SC shows two vortices exhibiting this behavior. The wake on the WC on the other hand, exhibits a *relatively* stationary boundary. There are turbulent fluctuations in the wake and over the roof flaps (as would be expected), however the vortical structures in the wake do not regularly convect downstream over the roof as on the SC. The velocity snapshot for the WC demonstrates the turbulent fluctuations, but also maintains an overall structure similar to the ensemble average. This further complicates the description of the roof-flap interaction and deployment. The rolling vortices being shed from the SC wake may be more likely to pull the flaps open than the small scale fluctuations over the flaps on the WC again indicating that the spoiler is more likely to yield proper function for the flaps.

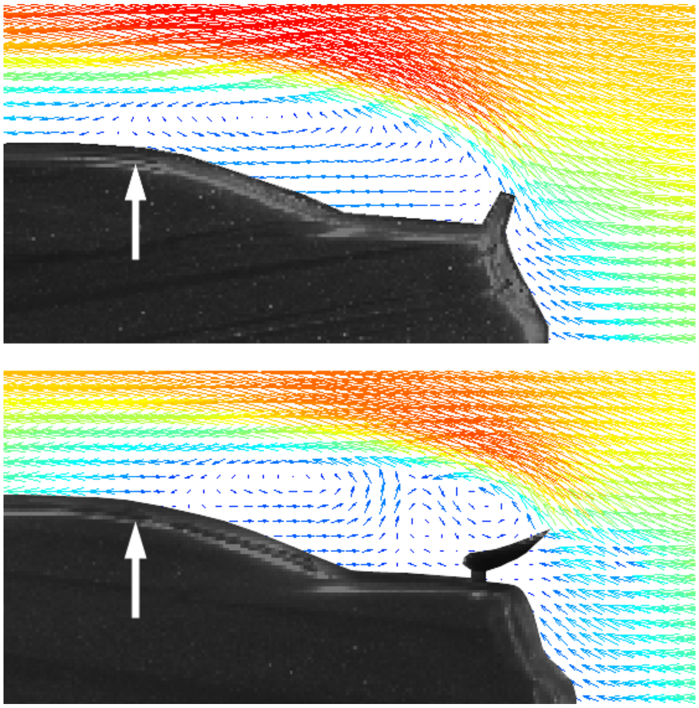

Figure 4.10: Ensemble averaged velocity maps for SC (top) and WC (bottom) at 180° yaw, $Re_H = 3.37 \times 10^4$. Arrows indicate rear edge of roof flaps.

4.4.2 Flow Characterization and Reynolds Number Scaling

For the mean SC flow, the region downstream of the spoiler can be described as an asymmetric wake in which there is a single large vortex shed from the edge of the spoiler. This is a wall-bounded wake which has a solid boundary imposed on it by the rear deck and backlight of the vehicle. Comparing streamlines at various Re in Figure 4.12, it is observed that the reattachment point and wake structure for the SC show negligible dependence on Re in these experiments. While there is no single canonical case with which to compare, this flow can be described in part as a forward facing step. This analysis does not hold perfectly as there is in fact a backward facing step downstream of the spoiler and a favorable pressure gradient imposed by the backlight. Conclusions drawn from comparing this flow scenario with idealized flow reattachment past a forward or backward facing step can be misleading; however, considering the forward facing step as a limiting case, one can attempt to

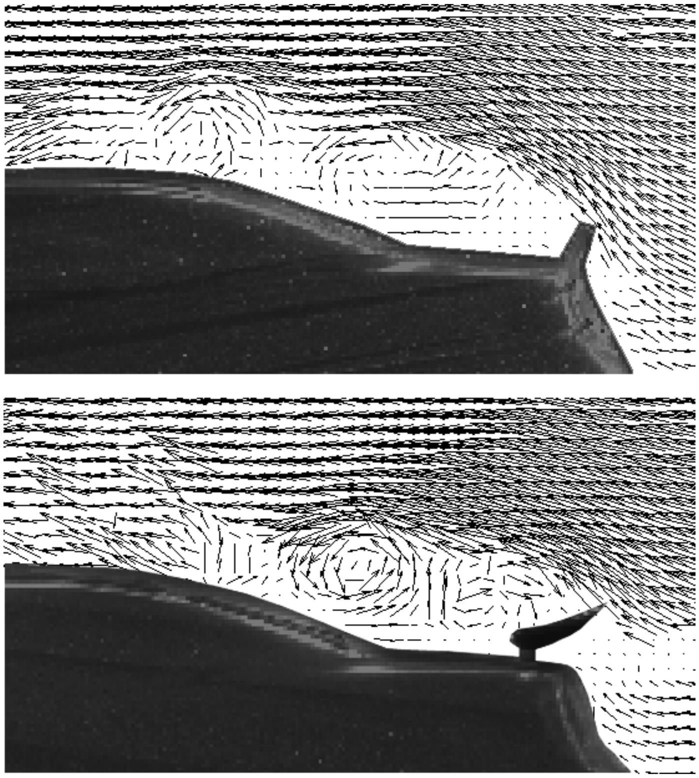

Figure 4.11: Instantaneous velocity maps for SC (top) and WC (bottom) at 180° yaw, $Re_H = 3.37 \times 10^4$.

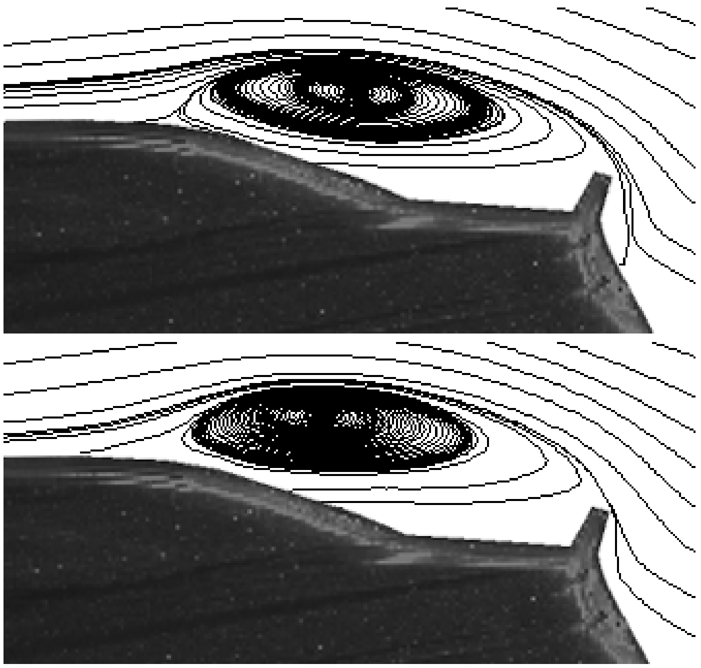

Figure 4.12: Streamlines showing mean flow past SC at 180° yaw and $Re_H = 3.37\times10^4$ (top) and $Re_H = 9.42 \cdot 10^4$ (bottom).

find rationale for phenomena observed in this flow. In describing this wake structure as such, the relevant local length scale is the size of the step in the fluid stream which, in this case, is the distance from the edge of the rear-fascia (where the rear bumper would be) to the tip of the spoiler. The relevant velocity scale is the free stream velocity, U_∞ which yields a local governing Reynolds number defined by

$$Re_L = D_L \cdot U_L/\nu \tag{4.4.1}$$

where D_L is the local length scale, U_L is the local streamwise velocity scale and is the kinematic viscosity, which is of the order 10^4. This appears to be sufficiently large to offset any Re dependence of downstream flow topology. This observation is consistent with results from Sherry et al.[121] who showed that the point of reattachment for a forward facing step immersed in a turbulent boundary layer has extremely weak dependence on Re beyond $Re = 10^4$.

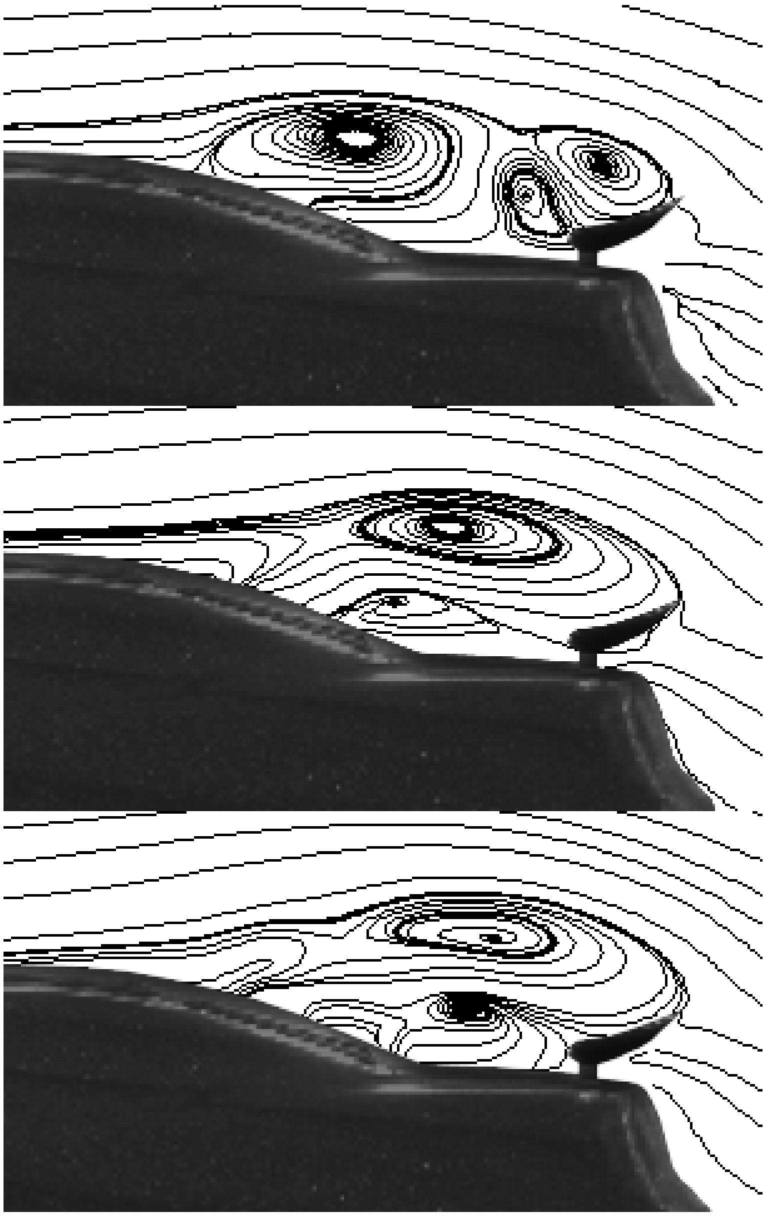

Figure 4.13: Streamlines showing mean flow past WC at 180° yaw and $Re_H = 3.37 \times 10^4$ (top), $Re_H = 6.73 \times 10^4$ (middle) and $Re_H = 9.42 \times 10^4$ (bottom).

The flow over the WC is much more complex than that of the SC. Several distinct structures can be seen in its wake and Figure 4.13 shows the development of vortical flow downstream of the wing for three Re_h. For $Re_h = 3.37 \times 10^4$, two counter-rotating vortices are being shed from the wing and a large counterclockwise vortex sits atop the rear window. A transition occurs at the higher Re_h in which only two distinct structures can be seen. Clearly, the vortical structures in this case are strikingly different from what is observed in the SC and strong Re dependence is seen. The region downstream of the wing appears to be a superposition of a planar wall-jet issuing through the gap between the wing and the deck-lid, and two wakes; the larger one is due to the blockage created by the rear fascia and the smaller more intense one is due to the projected frontal face of the wing. There are at least three Re_L scales (indicated in Figure B.7) that influence this flow with two additional Re_L scales compared to the SC. The first scale describes the wake caused by the rear fascia which is of the same order as that described in the SC case. The second Re_L is related to the wake caused by the wing, that has a similar velocity scale as the SC case, but a length scale—the projected height of the wing—which is an order of magnitude lower, yielding Re_L of the order 10^3. The third is related to the planar wall jet—issung between the wing and deck lid—where both the length and velocity scales are much lower than the SC. The data indicates that the velocity scale is an order of magnitude lower than U_∞, and the length scale, which is of the order of the gap between the wing and the deck-lid, is two orders of magnitude smaller than the rear fascia, which yields Re_L of the order 10^2. Subsequently, since the effective (relevant) local Reynolds numbers are not sufficiently large, it can be seen why such a strong Re dependence is observed in this case.

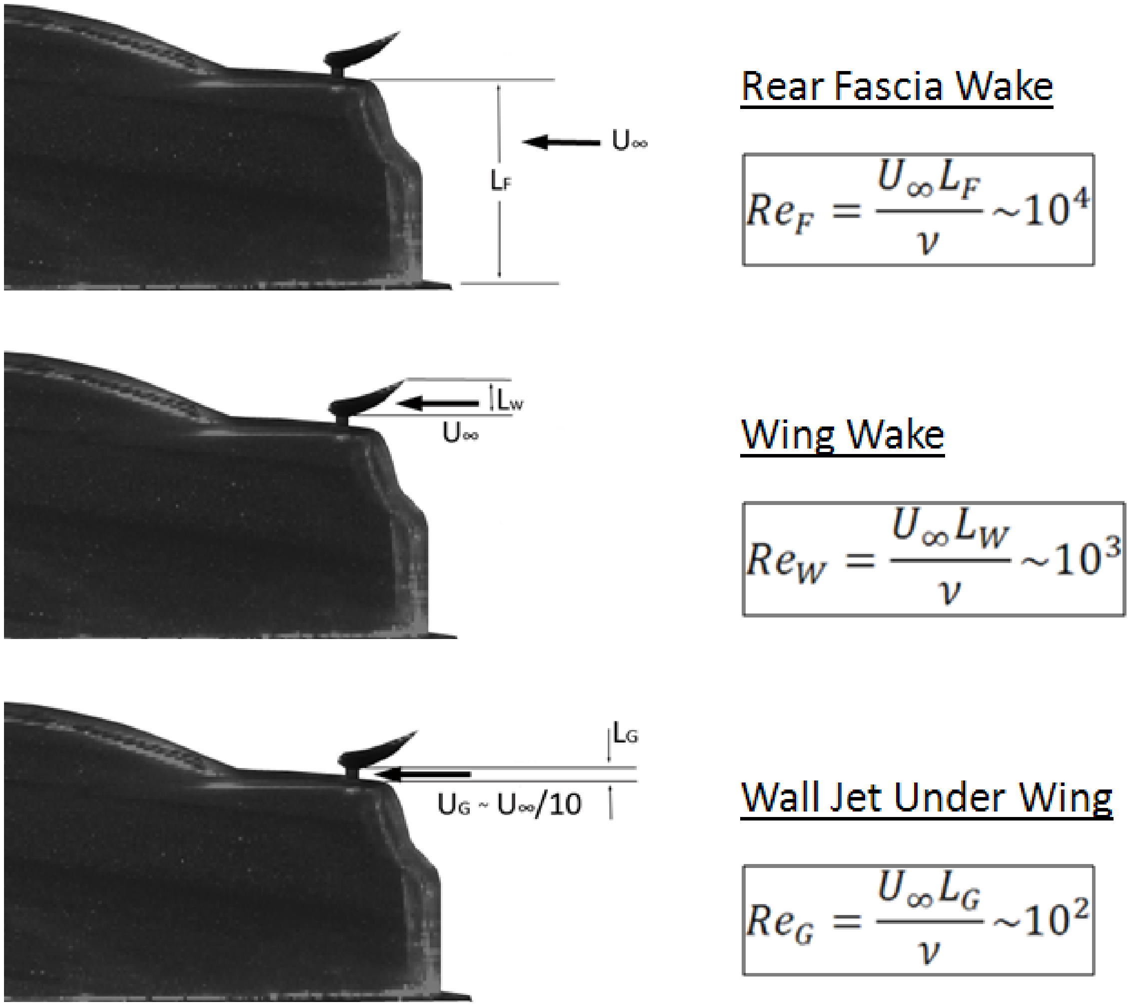

Figure 4.14: Local Reynolds number scales for flow modes contributing to wake at extreme yaw.

4.5 Summary

NASCAR COT models were tested under zero and 180° degree yaw with both a wing and spoiler mounted to evaluate the difference in performance and safety between the two downforce-generating devices. Additionally, interaction of these devices with roof flaps employed on the COT is analyzed. At zero yaw, the flow is found to show negligible Re dependence on either vehicle. The smaller length and time scales of the structures in the wake of the WC indicate enhanced performance with regards to trailing vehicle safety due to smaller fluctuations in downforce on the hood and roof of vehicles in close proximity. At 180° yaw, it is shown that the roof flaps may not function consistently on the WC because the low-pressure wake downstream of the wing does not extend over the roof and flow is reattached. On the SC, the wake downstream of the spoiler persists over the roof flaps and indicates that the flaps should deploy. The reattachment point and flow structure in the SC is found to show negligible dependence on Re, while strong dependence is seen in the WC case. Local Reynolds number scales are identified for both cases and at least one scale in the WC is found to be as low as 10^2 indicating why the flow is Re dependent.

REFERENCES

[1] R. H. Website, “Model 1520 research tunnel,” tech. rep., 2008.

[2] L. Jacquin, D. Fabre, D. Sipp, V. theofilis, and H. Vollmers, “Instability and unsteadiness of aircraft wake vortices,” *Aerospace Science and Technology*, vol. 7, pp. 577–593, 2003.

[3] R. Olfati-Saber, “Flocking for multi-agent dynamic systems: Algorithms and theory,” *IEEE Transactions on Automatic Control*, vol. 51, pp. 401–420, 2006.

[4] J. Katz, “Aerodynamics of race cars,” *Annual Review of Fluid Mechanics*, vol. 38, pp. 27–63, 2006.

[5] F. Lehmenn, S. Sane, and M. Dickinson, “The aerodynamic effects of win-wing interaction in flapping insect wings,” *Journal of Experimental Biology*, vol. 208, pp. 3075–3092, 2005.

[6] A. Gentry, “The aerodynamics of sail interaction,” in *Proceedings of the Third AIAA Symposium on the Aero/Hydrodynamics of Sailing*, 1971.

[7] L. Vermeer, J. Sorensen, and A. Crespo, “Wind turbine wake aerodynamics,” *Progress in Aerospace Science*, vol. 39, pp. 467–510, 2003.

[8] B. Munson, *Fundamentals of Fluid Mechanics.* John Wiley & Sons, Inc., 2006.

[9] A. Group, “ABS RCP 800 60 hz pump performance curve,” tech. rep., ABSEL PRO 1.7.2, 2007.

[10] Sikaflex, “221 sealant/adhesive,” tech. rep., Sika Corporation, Madison Heights, MI, 2007.

[11] T. Gelder and J. Moore, “Wind tunnel turning vanes of modern design,” tech. rep., NASA, 1985.

[12] R. Berry, “Design verification of hvac duct turning vanes in nuclear engineering,” *Structural Engineering in Nuclear Facilities*, vol. 23, pp. 412–426, 2000.

[13] S. Moujaes and S. Aekula, “CFD predictions and experimental comparisons of pressure drop effects of turning vanes in 90° duct elbows,” *Journal of Energy Engineering*, vol. 135, p. 119, 2009.

[14] P. Bradshaw, “The effect of wind-tunnel screens on nominally two-dimensional boundary layers,” *Journal of Fluid Mechanics*, vol. 22, pp. 679–687, 1965.

[15] P. Bradshaw, “Design rules for small low-speed wind tunnels,” *Aeronautical Journal of the Royal Aeronautical Society*, vol. 73, p. 443, 1979.

[16] C. Pennycuick, T. Alerstam, and A. Hendenstrouml, “A new low-turbulence wind tunnel for bird flight experiments at Lund University Sweden,” *Journal of Experimental Biology*, vol. 200, pp. 1441–1449, 1999.

[17] S. DeFrance, “The N.A.C.A. full-scale wind tunnel,” tech. rep., NACA, 1935.

[18] J. Bell, “Boundary layer predictions for small low-speed contractions,” *American Institute of Aeronautics and Astronautics Jounral*, vol. 27, pp. 372–374, 1989.

[19] E. Shaw, “Fish in schools,” *Natural History*, vol. 84, pp. 40–45, 1975.

[20] A. Mogilner and L. Edelstein-Keshet, “A non-local model for a swarm,” *J. Math. Biology*, vol. 38, pp. 534–570, 1999.

[21] B. Partridge, “The structure and function of fish schools,” *Scientific American*, vol. 246, pp. 114–123, 1982.

[22] A. Okubo, “Dynamical aspects of animal grouping: swarms, schools, flocks. and herds,” *Advances in Biophysics*, vol. 22, pp. 1–94, 1986.

[23] J. Parrish, S. Viscido, and D. Grunbaum, “Self-organized fish schools: an examination of emergent properties,” *Biol. Bull.*, vol. 202, pp. 296–305, 2002.

[24] C. Reynolds, “Flocks, herds, and schools: a distributed behavioral model,” *Computer Graphics*, vol. 21, pp. 25–34, 1987.

[25] P. Lissman and C. Shollenberger, “Formation flight of birds,” *Science*, vol. 168, pp. 103–105, 1970.

[26] S. Kelly and H. Xiong, “Controlled hydrodynamic interactions in schooling and aquatic locomotion,” in *Proceedings of the 44th IEEE Conference on Decision and Control*, 2005.

[27] J. Eldredge, “Dynamically coupled fluid-body interactions in vorticity-based numerical simulations,” *Journal of Computational Physics*, vol. 227, pp. 9170–9194, 2008.

[28] R. Katzmayr, “Effect of periodic changes of angle of attack on behavior of airfoils,” tech. rep., NACA TM 147, 1922.

[29] T. Theodorsen, “General theory of aerodynamic instability and the mechanism of flutter,” tech. rep., NACA TR 496, 1935.

[30] T. Von Karman and W. Sears, “Airfoil theory for non-uniform motion,” *Journal of the Aeronautical Sciences*, vol. 5, pp. 379–390, 1938.

[31] A. Silverstein and U. Joyner, “Experimental verification of the theory of oscillating airfoils,” tech. rep., NACA TR 673, 1939.

[32] J. O. Scherer, "Experimental and theoretical investigation of large amplitude oscillating foil propulsion systems," tech. rep., U.S. Army Engineering Research, 1968.

[33] J. DeLaurier and J. Harris, "Experimental study of oscillating wing propulsion," *Journal of Aircraft*, vol. 19, pp. 368–373, 1982.

[34] P. Lai, N. Bose, and R. McGregor, "Wave propulsion from a flexible-armed, rigid-foil propulsor," *Marine Technology*, vol. 30, pp. 28–36, 1993.

[35] R. Godoy-Diana, J. Aider, and J. Wesfried, "Transitions in the wake of a flapping foil," *Physical Review E*, vol. 77, pp. 2–5, 2008.

[36] D. Read, F. Hover, and M. Triantafyllou, "Forces on oscillating foils for propulsion and maneuvering," *Journal of Fluids and Structures*, vol. 17, pp. 163–183, 2002.

[37] A. Techet, "Propulsive performance of bioligically inspired flapping foils at high Reynolds numbers," *Journal of Experimental Biology*, vol. 211, pp. 274–279, 2007.

[38] J. Anderson, K. Streitlien, D. Barrett, and M. Triantafyllou, "Oscillating foils of high propulsive efficiency," *Journal of Fluid Mechanics*, vol. 360, pp. 41–72, 1998.

[39] T. Wu, "Swimming of a waving plate," *Journal of Fluid Mechanics*, vol. 10, pp. 321–344, 1961.

[40] T. Wu, "Hydromechanics of swimming of fishes and cetaceans," *Advances in Applied Mechanics*, vol. 11, pp. 1–63, 1971.

[41] T. Maxworthy, "The fluid dynamics of insect flight," *Annual Review of Fluid Mechanics*, vol. 13, pp. 329–350, 1981.

[42] G. Longvinovich, *Hydrodynamics of a Thin, Flexible Body.* Joint Publications Research Service, Washington DC, 1971.

[43] H. Cheng and L. Murillo, "Lunate-tail swimming propulsion as a problem of curved lifting line in unsteady flow. part 1. Aysmptotic theory," *Journal of Fluid Mechanics*, vol. 143, pp. 327–350, 1984.

[44] G. Karpouzian, G. Spedding, and H. Cheng, "Lunate-tail swimming propulsion. part 2. performance analysis," *Journal of Fluid Mechanics*, vol. 210, pp. 329–351, 1990.

[45] J. McCune and T. Tavares, "Perspective: Unsteady wing theory - the karman/sears legacy," *Transactions ASME Fluids Engineering*, vol. 115, pp. 548–560, 1993.

[46] R. Nudds, G. Taylor, and A. Thomas, “Tuning of strouhal number for high propulsive efficiency accurately predicts how wingbeat frequency and stroke amplitude relate and scale with size and flight speeds in birds,” tech. rep., The Royal Society, 2004.

[47] T. Benkherouf, M. Mekadem, S. Oualli, L. Keisbuluk, and L. Labraga, “Efficiency of an auto-propelled flapping airfoil,” *Journal of Fluids and Structures*, vol. 27, pp. 552–566, 2011.

[48] J. Zhang, N. Liu, and X. Lu, “Locomotion of a passively flapping flat plate,” *Journal of Fluid Mechanics*, vol. 659, pp. 43–68, 2010.

[49] E. Stamhuis and J. Videler, “Quantitative flow analysis around aquatic animals using laser sheet particle image velocimetry,” *Journal of Experimental Biology*, vol. 198, pp. 283–294, 1995.

[50] U. Mueller, E. van den Heuvel, E. Stamhuis, and J. Videler, “Fish foot prints: Morphology and energetics of the wake behind a continuously swimming mullet,” *Journal of Experimental Biology*, vol. 200, pp. 2893–2906, 1997.

[51] M. Wolfgang, M. Anderson, M. Grosenbaugh, D. Yue, and M. Triantafyllou, “Near-body flow dynamics in swimming fish,” *Journal of Experimental Biology*, vol. 202, pp. 2303–2327, 1999.

[52] E. Drucker and G. Lauder, “Locomotor forces on a swimming fish: Three dimensional vortex wake dynamics quantified using dpiv,” *Journal of Experimental Biology*, vol. 202, pp. 2393–2412, 1999.

[53] E. Drucker and G. Lauder, “A hydrodynamic analysis of fish swimming speed: Wake structure and locomotor force in slow and fast labriform swimmers,” *Journal of Experimental Biology*, vol. 203, pp. 2379–2393, 2000.

[54] G. Lauder, “Function of the caudal fin during locomotion in fishes: Kinematics, flow visualization and evolutionary patterns,” *Ameri. Zool.*, vol. 40, pp. 101–122, 2000.

[55] M. Triantafyllou, G. Triantafyllou, and D. Yue, “Hydrodynamics of fishlike swimming,” *Annual Review of Fluid Mechanics*, vol. 32, pp. 33–53, 2000.

[56] M. S. Triantafyllou, A. Techet, and F. Hover, “Review of experimental work in biomimetic foils,” *IEEE Journal of Ocean*, vol. 29, pp. 585–594, 2004.

[57] G. Taylor, R. Nudds, and A. Thomas, “Flying and swimming animals cruise at a strouhal number tuned for high power efficiency,” *Nature*, vol. 425, p. 707, 2003.

[58] Z. J. Wang, “Dissecting insect flight,” *Annual Review of Fluid Mechanics*, vol. 37, pp. 183–210, 2005.

[59] G. Lauder, E. Anderson, J. Tangorra, and M. Peter, “Fish biorobotics: Kinematics and hydrodynamics of self-propulsion,” *Journal of Experimental Biology*, vol. 210, pp. 2767–2780, 2007.

[60] M. M. Koochesfahani, “Vortical patterns in the wake of an oscillating airfoil,” *AIAA Journal*, vol. 27, pp. 1200–1205, 1989.

[61] T. Von Karman and J. Burgers, *Aerodynamic Theory*, ch. General Aerodynamic Theory-Perfect Fluids, p. 308. 1943.

[62] J. Bratt, “Flow patterns in the wake of an oscillating airfoil,” tech. rep., Aeronautical Research Council Reports and Memoranda, 1953.

[63] J. Katz and D. Weihs, “Behavior of vortex wakes froom oscillating airfoils,” *Journal of Aircraft*, vol. 15, pp. 861–863, 1978.

[64] A. Thomas and M. Whiffen, “Flow visualization as an aerodynamic diagnostic tool,” tech. rep., Lockheed Horizons, 1984.

[65] R. Djojodihardjo and S. Widnall, “A numerical method for the calculation of nonlinear unsteady lifting potential flow problems,” *AIAA Journal*, vol. 7, pp. 2001–2009, 1969.

[66] M. Vezza and R. Galbraith, “A method for predicting unsteady potential flow about an airfoil,” *International Journal for Numerical Methods in Fluids*, vol. 5, pp. 347–356, 1985.

[67] P. Freymuth, “Propulsive vortical signature of plunging and pitching airfoils,” *AIAA Journal*, vol. 26, pp. 881–883, 1988.

[68] T. Schnipper, A. Anderson, and T. Bohr, “Vortex wakes of a flapping foil,” *Journal of Fluid Mechanics*, vol. 633, pp. 411–423, 2009.

[69] C. Williamson and A. Roshko, “Vortex formation in the wake of an oscillating cylinder,” *Journal of Fluids and Structures*, vol. 2, pp. 355–381, 1988.

[70] T. Lau, R. Kelso, and E. Hassan, “Flow visualisation of a pitching and heaving hydrofoil,” in *15th Australasian Fluid Mechanics Conference*, 2004.

[71] A. Anderson, T. Bohr, and T. Schnipper, “Separation vortices and pattern formation,” *Theoretical and Computational Fluid Dynamics*, vol. 24, pp. 329–334, 2010.

[72] R. Godoy-Diana, C. Marais, J. Aider, and J. Wesfried, “A model for the symmetry breaking of the reverese Benard-von Karman vortex street produced by a flapping foil,” *Journal of Fluid Mechanics*, vol. 622, pp. 23–32, 2009.

[73] C. Williamson and R. Govardham, “Vortex-induced vibrations,” *Annual Review of Fluid Mechanics*, vol. 36, pp. 413–455, 2004.

[74] S. Jung, K. Mareck, M. Shelly, and J. Zhang, "Dynamics of a deformable body in a fast flowing soap film," *Physical Review Letters*, vol. 97, p. 134502, 2006.

[75] H. Aref, M. Stremler, and F. Ponta, "Exotic vortex wakes-point vortex solutions," *Journal of Fluids and Structures*, vol. 22, pp. 929–940, 2006.

[76] K. Jones, c. Dohring, and M. Platzer, "Experimental and computational investigation of the Knoller-Betz effect," *AIAA Journal*, vol. 36, pp. 1240–1246, 1998.

[77] H. Hasegawa and K. Nakagawa, "Dynamic behavior of vortex shedding from an oscillating three-dimensional airfoil," in *27th International Congress of the Aeronautical Sciences*, 2010.

[78] M. Green and A. Smits, "Effects of three-dimensionality on thrust production by a pitching foil," *Journal of Fluid Mechanics*, vol. 615, pp. 211–220, 2008.

[79] J. Buchholz and A. Smits, "On the evolution of the wake structure produced by a low-aspect-ratio pitching panel," *Journal of Fluid Mechanics*, vol. 546, pp. 433–443, 2006.

[80] K. Parker, K. Ellenrieder, and J. Soria, "Morphology of the forced oscillatory flow past a finite-span wing at low reynolds number," *Journal of Fluid Mechanics*, vol. 571, pp. 327–357, 2007.

[81] H. Dong, R. Mittal, and F. Najjar, "Wake topology and hydrodynamic performance of low-aspect-ratio flapping foils," *Journal of Fluid Mechanics*, vol. 566, pp. 309–343, 2006.

[82] J. Warkentin and J. DeLaurier, "Experimental aerodynamic study of tandem flapping membrane wings," *Journal of Aircraft*, vol. 44, pp. 1653–1661, 2007.

[83] S. Kim, W. Huang, and H. Sung, "Constructive and destructive interaction modes between two tandem flexible flags in viscous flow," *Journal of Fluid Mechanics*, vol. 661, pp. 511–521, 2010.

[84] M. Zdravkovich, "Flow induced oscillations of two interfering circular cylinders," *Journal of Sound and Vibration*, vol. 101, pp. 511–521, 1985.

[85] J. Eldredge and D. Passani, "Passive locomotion of a simple articulated fish-like system in the wake of an obstacle," *Journal of Fluid Mechanics*, vol. 611, pp. 97–106, 2008.

[86] C. Munch, O. Ausoni, and F. Avellan, "Fluid-structure coupling for an oscillating hydrofoil," *Journal of Fluids and Structures*, vol. 26, pp. 1018–1033, 2009.

[87] K. Streitlien, G. Triantafyllou, and M. Triantafyllou, "Efficient foil propulsion through vortex control," *AIAA Journal*, vol. 34, pp. 2315–2319, 1996.

[88] M. He, B. Veitch, N. Bose, B. Colbourne, and P. Liu, “A three-dimensional wake impingement model and application on tandem oscillating foils,” *Ocean Engineering*, vol. 34, pp. 1197–1210, 2007.

[89] J. Deng, X. Shao, and Z. Yu, “Hydrodynamic studies on two travelling wavy foils in tandem arrangement,” *Physics of Fluids*, vol. 19, pp. 11–21, 2007.

[90] I. Akhtar and R. Mittal, “A biologically inspired computational study of flow past tandem flapping foils,” in *35th AIAA Fluid Dynamics Conference and Exhibit*, 2005.

[91] Q. Liao, G. Dong, and X. Lu, “Vortex formation and force characteristics of a foil in the wake of a circular cylinder,” *Journal of Fluids and Structures*, vol. 19, pp. 491–510, 2003.

[92] D. Beal, F. Hover, M. Triantafyllou, J. Liao, and G. Lauder, “Passive propulsion in vortex wakes,” *Journal of Fluid Mechanics*, vol. 549, pp. 385–402, 2006.

[93] L. Lu and C. Smith, “Image processing of hydrogen bubble flow visualization for determination of turbulence statistics and bursting characteristics,” *Experiments in Fluids*, vol. 3, pp. 349–356, 1985.

[94] W. Yang, *Handbook of Flow Visualization.* Hemisphere Publishing Corp, 1989.

[95] J. van Wijk, “Image based flow visualization,” in *Proceedings of the 29th annual conference on Computer Graphics and Interactive Techniques*, 2002.

[96] T. Utami and T. Ueno, “Visualization and picture processing of turbulent flow,” *Experiments in Fluids*, vol. 2, pp. 25–32, 1985.

[97] G. Mattingly, “The hydrogen-bubble flow visualization technique, accession number: Ad0630468,” tech. rep., Washington DC Hydromechanics Lab, 1966.

[98] W. Merzkirch, *Flow Visualization Second Edition.* Academic Press, Inc., 1987.

[99] Y. Tanaka, K. Kikuchi, Y. Saihara, and Z. Ogumi, “Bubble visualization and electrolyte dependency of dissolving hydrogen in electrolyzed water using solid-polymer-electrolyte,” *Electromechnica Acta*, vol. 50, pp. 5229–5236, 2005.

[100] S. Kline, W. Reynolds, F. Schraub, and P. Runstadler, “The structure of turbulent boundary layers,” *Journal of Fluid Mechanics*, vol. 30, pp. 741–773, 1967.

[101] S. Meenakshisundaram, “Flow visualisation by hydrogen bubble technique and its use in some fluid problems,” Master’s thesis, Department of Applied Mechanics. IIT-Madras., 1980.

[102] M. Stremler, A. Salmanzadeh, S. Basu, and C. Willamson, “A mathematical model of 2p and 2c vortex wakes,” *Journal of Fluids and Structures*, vol. 27, pp. 774–783, 2011.

[103] M. Hall, “Vortex breakdown,” *Annual Review of Fluid Mechanics*, vol. 4, p. 195, 1972.

[104] S. Leibovich, “The structure of vortex breakdown,” *Annual Review of Fluid Mechanics*, vol. 10, p. 221, 1978.

[105] M. Escudier, “Vortex breakdown: Observations and explanations,” *Progress in Aerospace Science*, vol. 25, p. 189, 1988.

[106] J. Delery, “Aspects of vortex breakdown,” *Progress in Aerospace Science*, vol. 30, p. 1, 1993.

[107] T. Schmitz and K. S. Smith, *Machining Dynamics*. Springer, 2008.

[108] D. Rodman, “Car of tommorrow to make race debut in 2007. nascar.com.” NASCAR.com, Decmeber 9, 2006.

[109] G. Nelson, J. Roush, G. Eaker, and S. Wallis, “The development and manufacture of a roof mounted aero flap system for race car applications,” in *SAE World Congress*, vol. Paper 942522, December 1994.

[110] B. Borden, “Cup car’s wing has a downforce to be reckoned with,” tech. rep., ESPN, 2008.

[111] J. Brzustowitz and J. d. L. Rode, “Experimental & computational simulations utilized during the aerodynamic development of the Dodge Intrepid R/T race car,” in *SAE World Congress*, December 2002.

[112] T. Laise and K. Bayless, “Aerodynamic development of a successful Winston Cup race car,” in *SAE World Congress*, 1994.

[113] L. Duncan, “Wind tunnel and track testing an ARCA race car,” in *SAE World Congress*, 1990.

[114] J. Leuschen and K. Cooper, “The effect of ambient conditions on the measured top speed of a Winston Cup car,” in *SAE World Congress*, 2004.

[115] D. Landman, “Road simulation for NASCAR vehicles at the langley full-scale tunnel,” in *SAE World Congress*, 2000.

[116] R. Dominy and G. LeGood, “The use of a bluff body wake generator for wind tunnel studies of NASCAR drafting aerodynamics,” in *SAE World Congress*, 2008.

[117] B. Duncan and K. Golsch, “Characterization of separated turbulent flow regions in CFD results for a pontiac NASCAR race car,” in *SAE World Congress*, 2004.

[118] R. Singh, “CFD simulation of NASCAR racing car aerodynamics,” in *SAE World Congress*, 2008.

[119] G. Erickson, “Vortex flow correlations,” tech. rep., AFW-AL-TR-80-3143, 1981.

[120] B. Cobleigh and J. Del Frate, “Water tunnel flow visualization study of a 4.4scale x-31 forebody”,” tech. rep., NASA, 1994.

[121] M. Sherry, D. Jacono, J. Sheridan, R. Mathis, and I. Marusic, “Flow separation characterisation of a forward facing step immersed in a turbulent boundary layer,” in *TSFP-6*, 2009.

[122] S. Johnson and D. Fisher, “Water tunnel study results of a tf/a-18 and f/a-18 canopy flow visualization,” tech. rep., NASA, 1990.

[123] P. Neuhart and O. Pendergraft, “A water tunnel study of Gurney flaps,” tech. rep., NASA, 1988.

[124] P. E. Dimotakis, “The mixing transition in turbulent flows,” *Journal of Fluid Mechanics*, vol. 409, no. -1, pp. 69–98, 2000.

[125] Y.-L. Yeh, C.-C. Hsu, C.-H. Chiang, and F.-B. Hsiao, “Vortical structure evolutions and spreading characteristics of a plane jet flow under anti-symmetric long-wave excitation,” *Experimental Thermal and Fluid Science*, vol. 33, no. 4, pp. 630–641, 2009.

APPENDIX A: FREQUENCY RESPONSE DATA

A.1 Frequency Response Magnitude

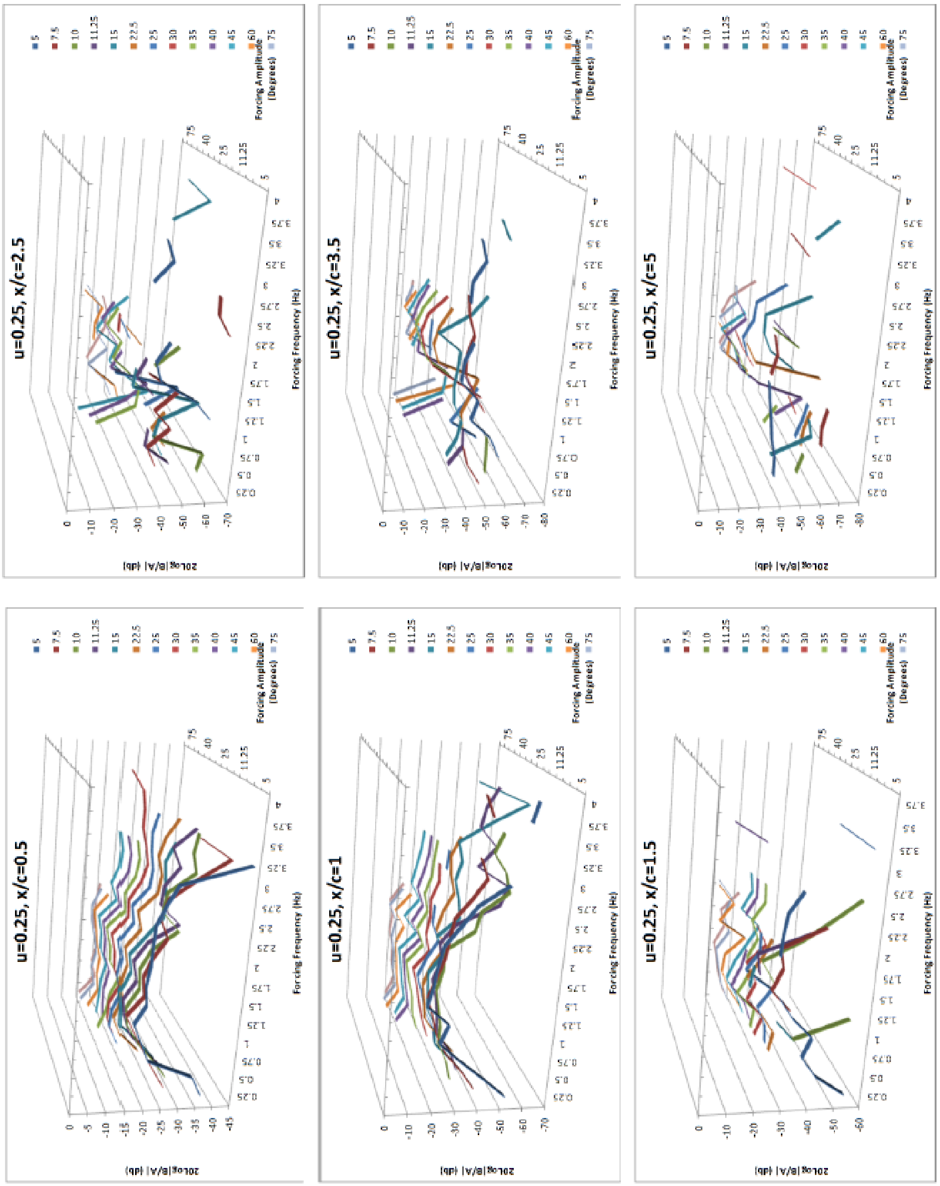

Figure A.1: Frequency response in dB for all x/c at u=0.25m/s.

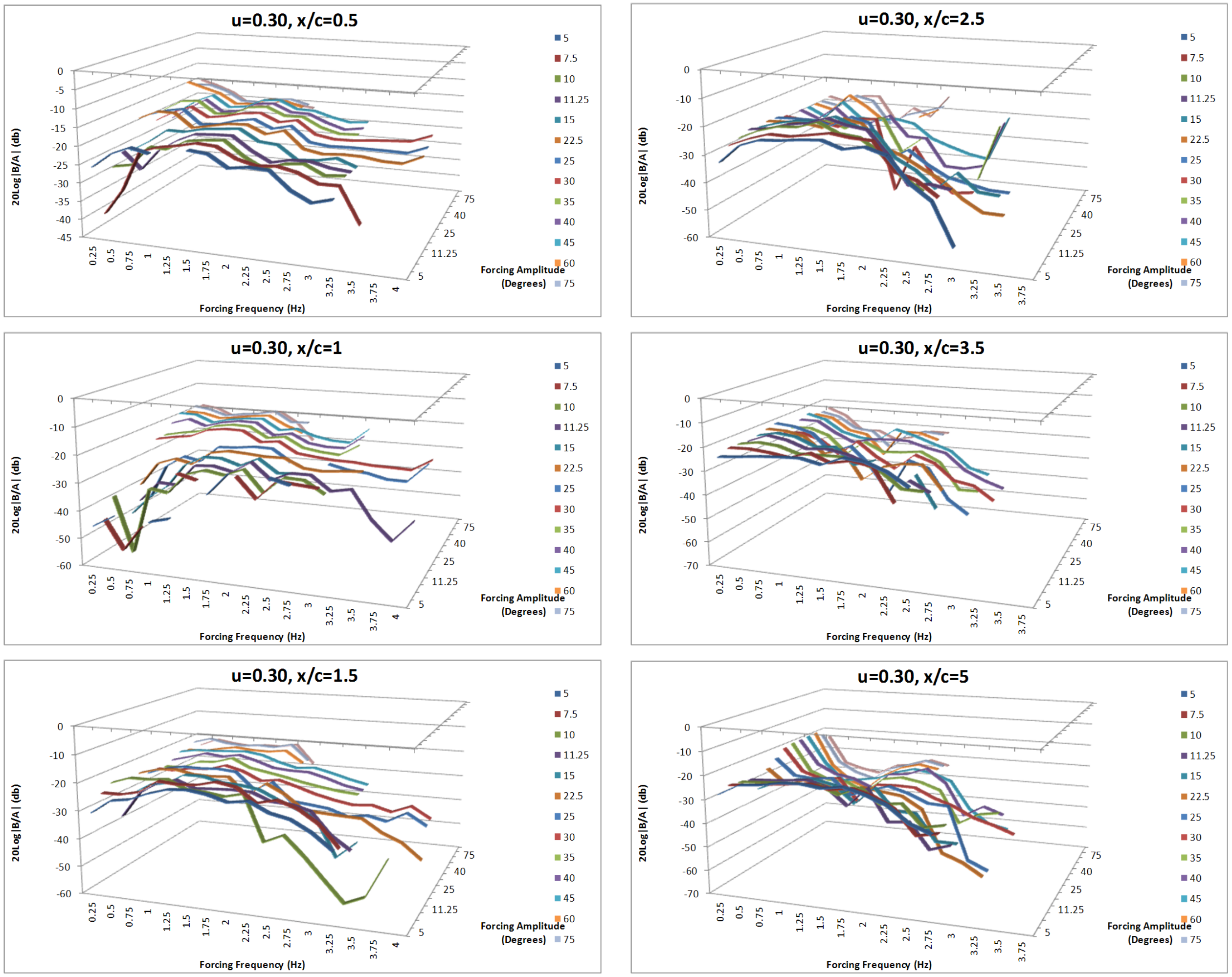

Figure A.1: Frequency response in dB for all x/c at u=0.30m/s.

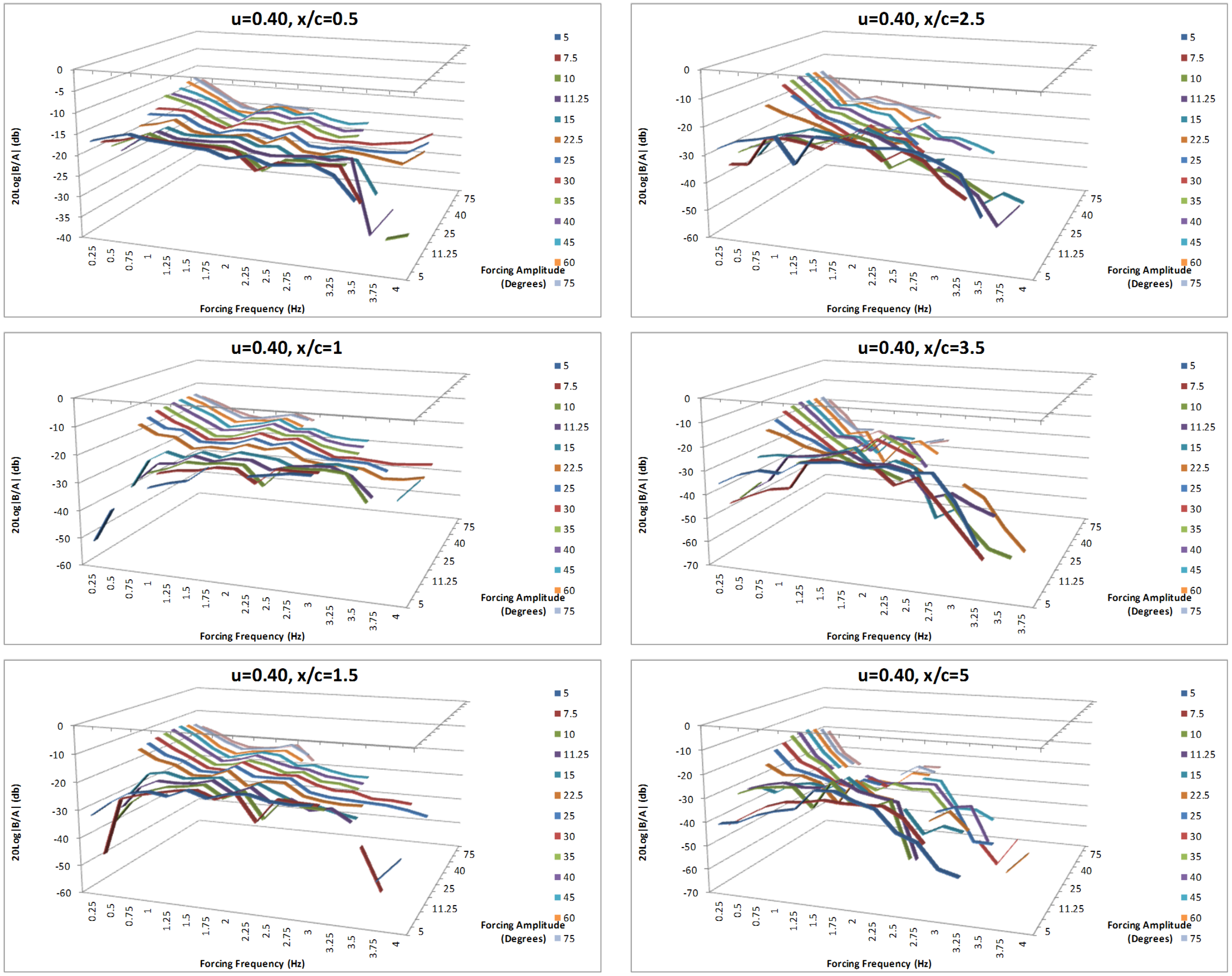

Figure A.2: Frequency response in dB for all x/c at u=0.40m/s.

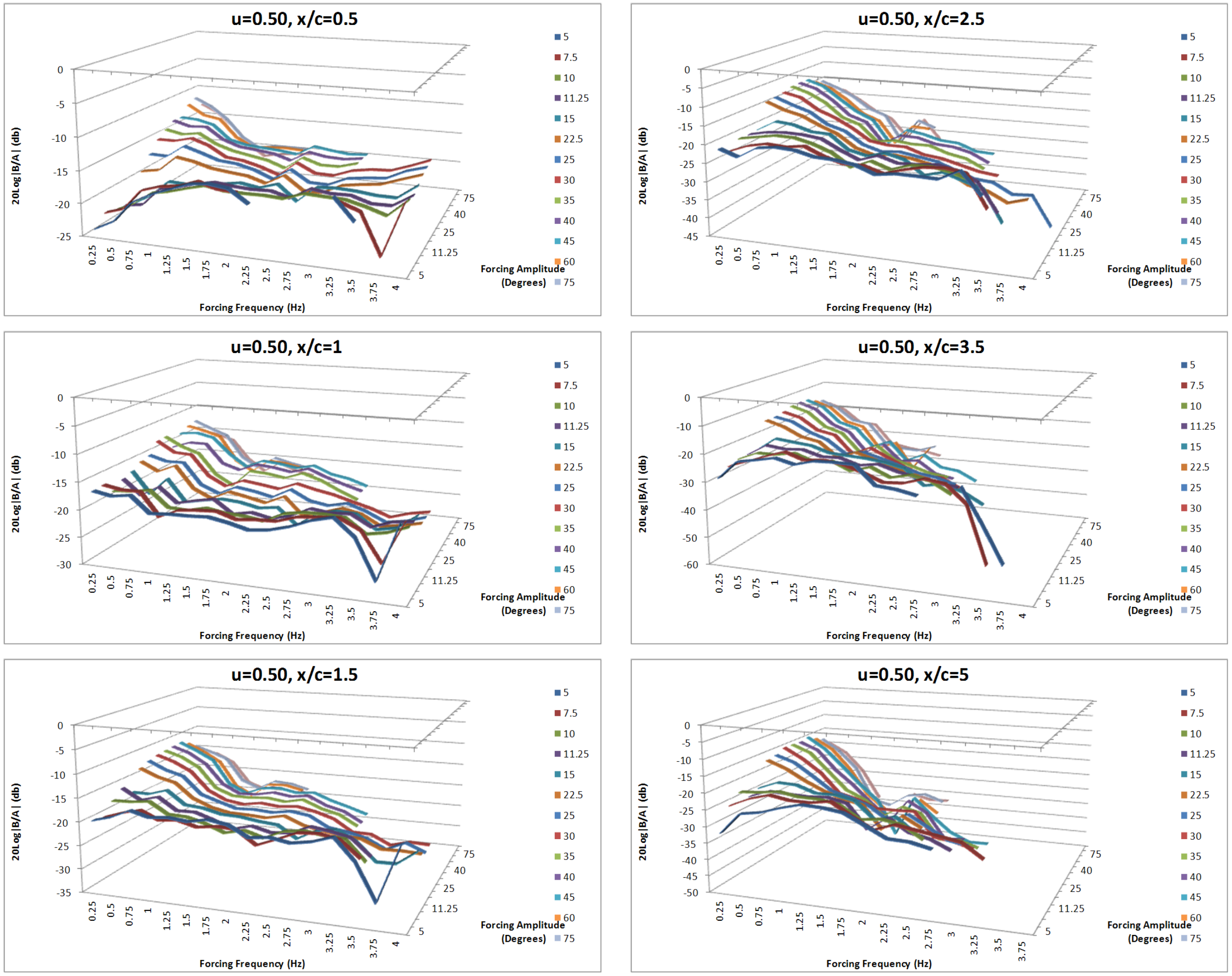

Figure A.3: Frequency response in dB for all x/c at u=0.50m/s.

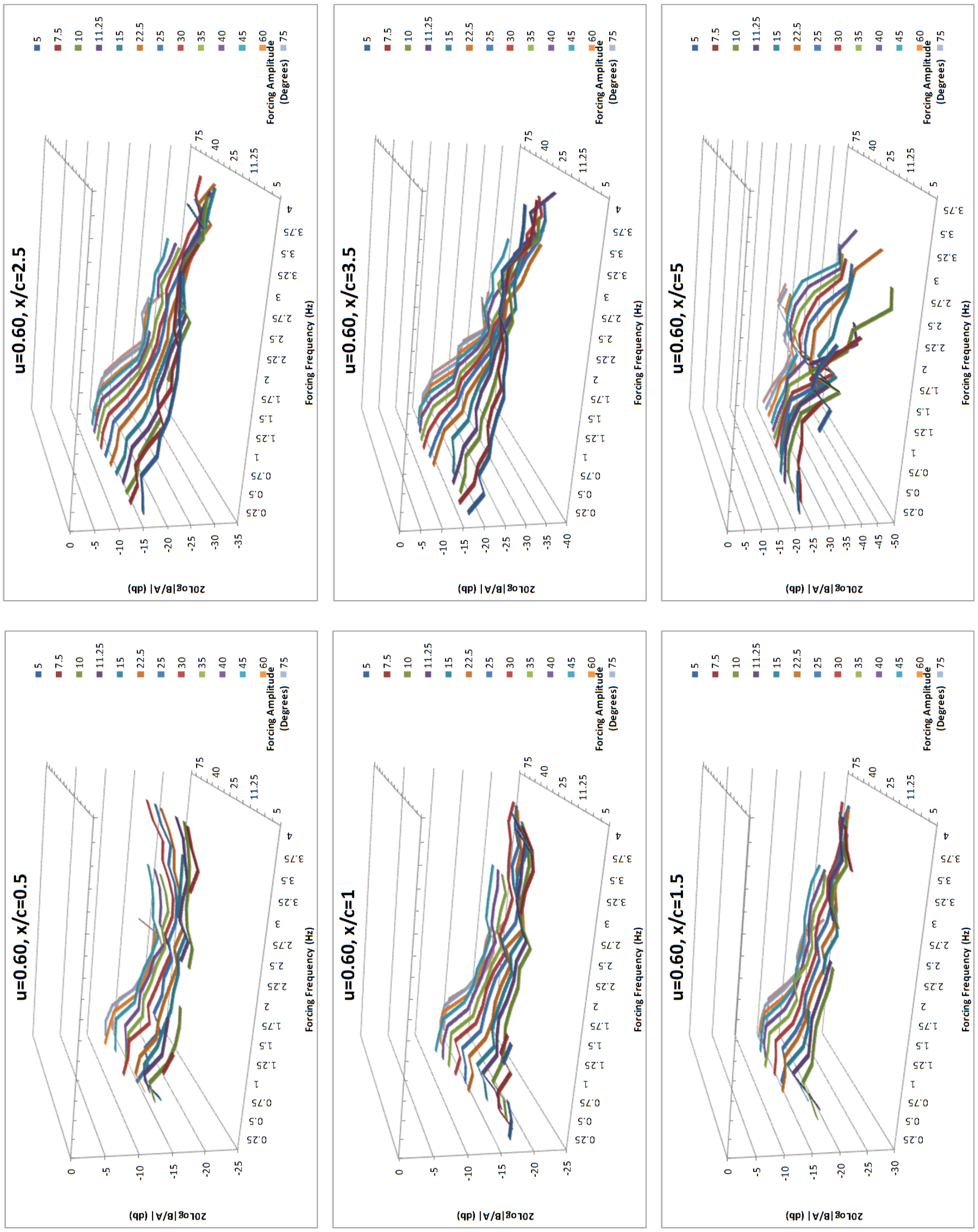

Figure A.4: Frequency response in dB for all x/c at u=0.60m/s.

A.2 Frequency Response Phase Shift

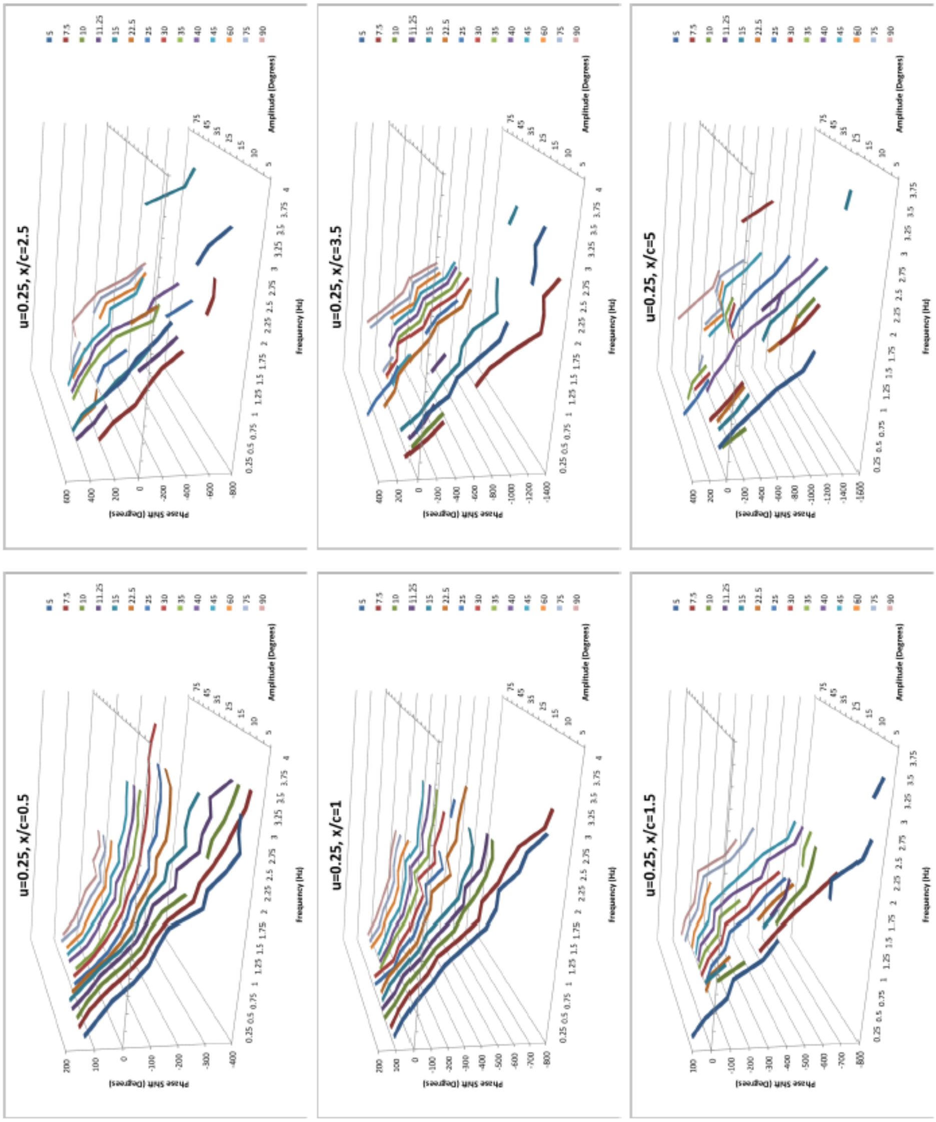

Figure A.6: Absolute phase shift in degrees for all x/c at u=0.25m/s.

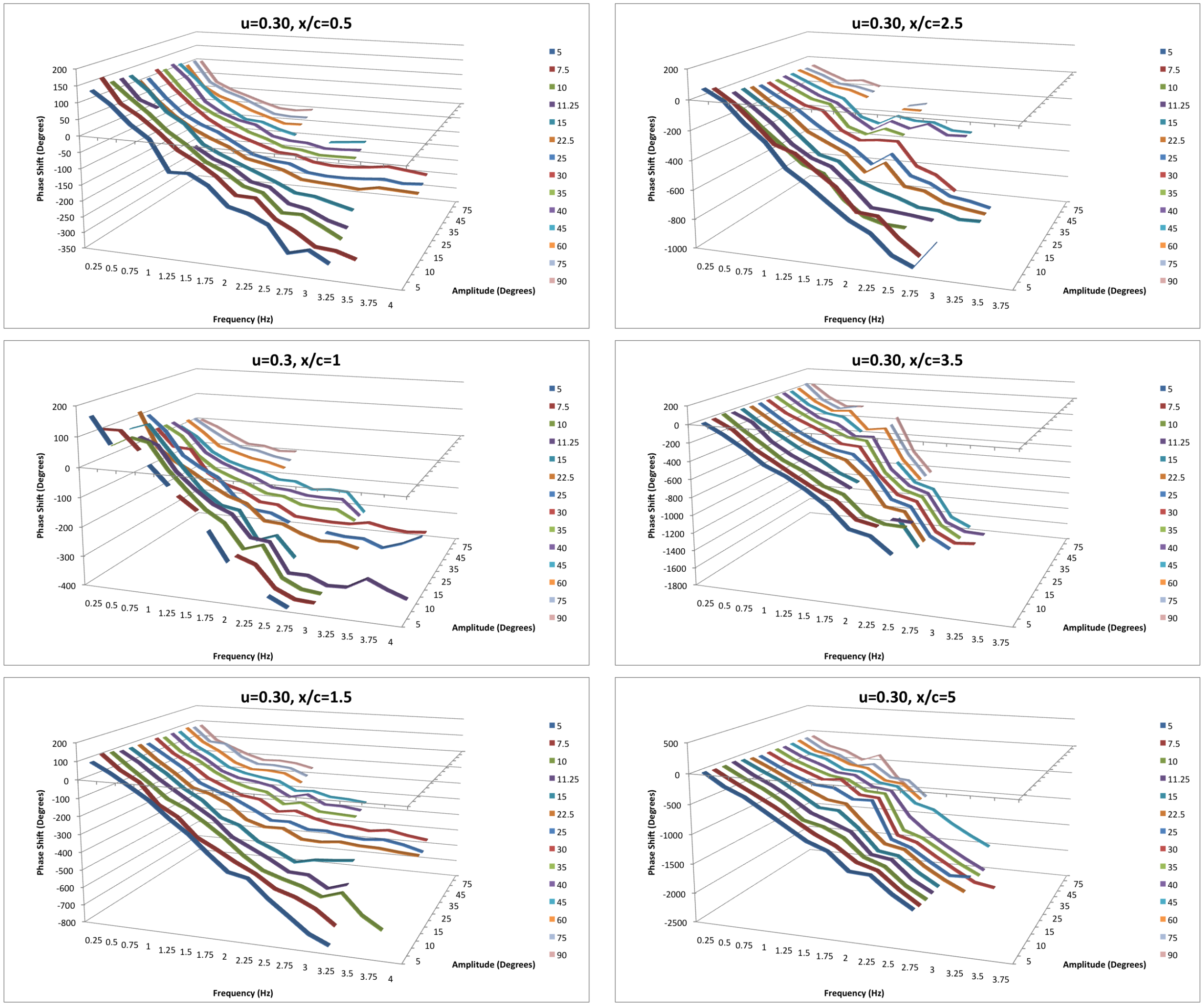

Figure A.5: Absolute phase shift in degrees for all x/c at u=0.30m/s.

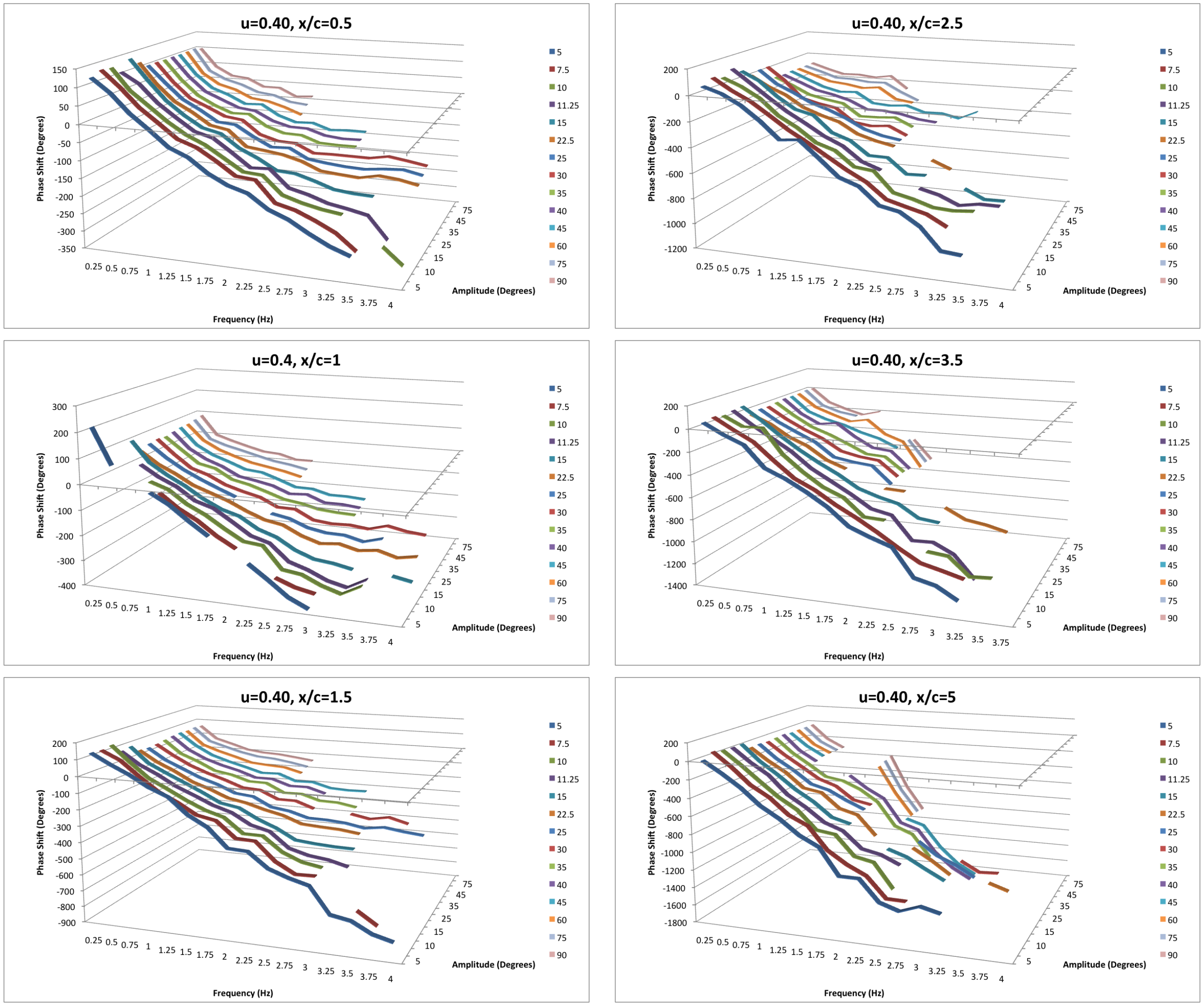

Figure A.6: Absolute phase shift in degrees for all x/c at u=0.40m/s.

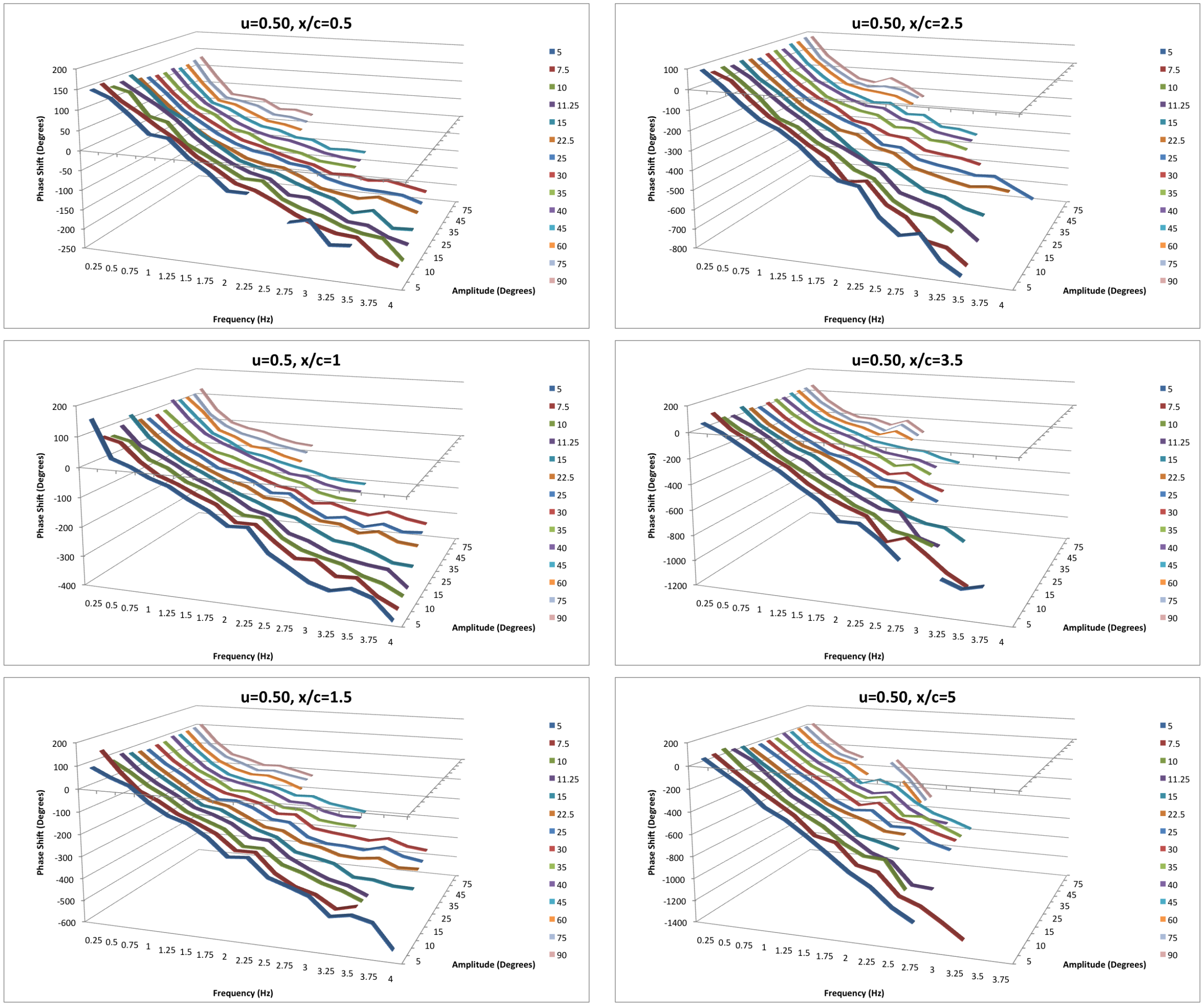

Figure A.7: Absolute phase shift in degrees for all x/c at u=0.50m/s.

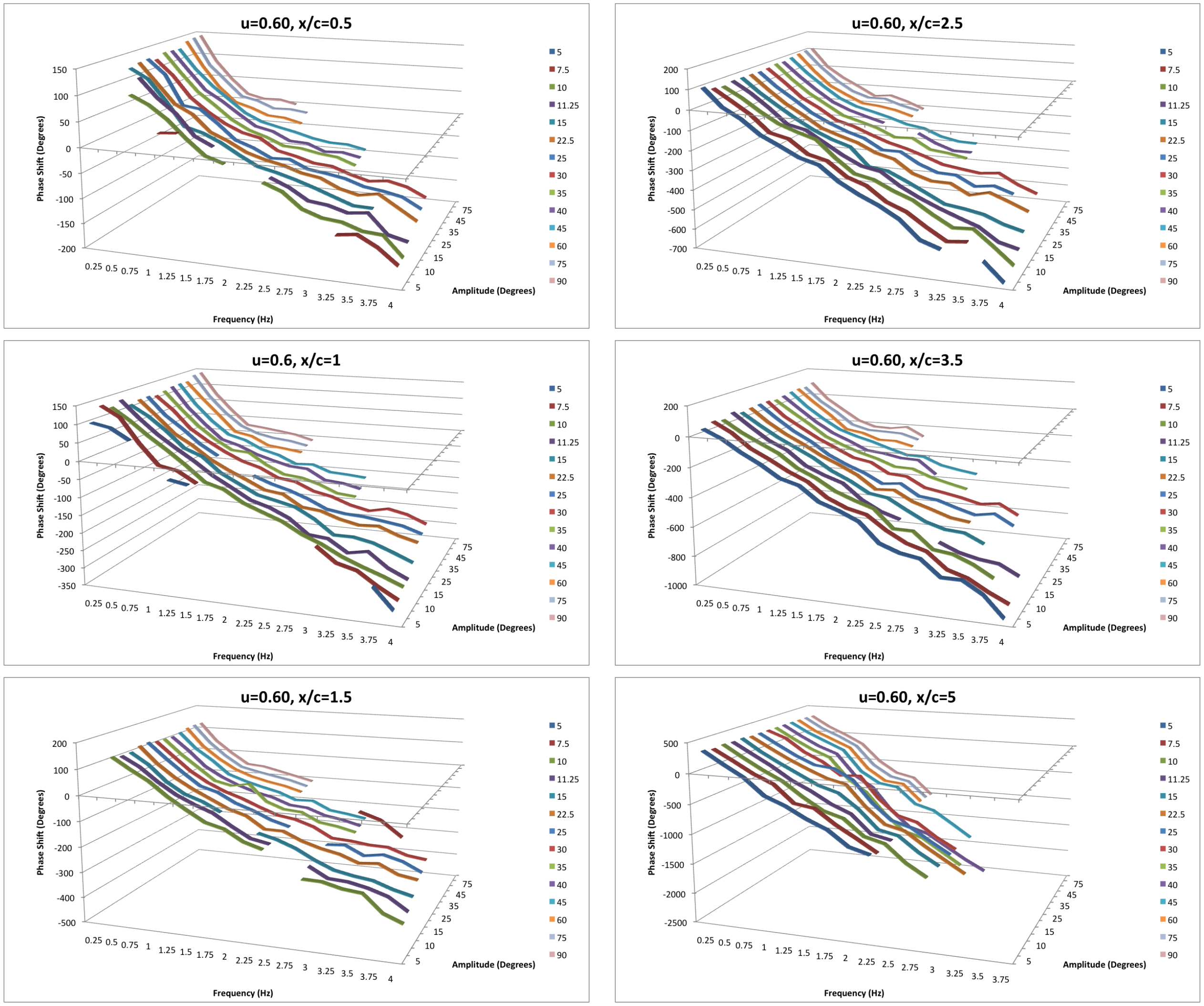

Figure A.8: Absolute phase shift in degrees for all x/c at u=0.60m/s.

APPENDIX B: PROGRAMS AND CODE

B.1 LabView Data Aquisition Program Block

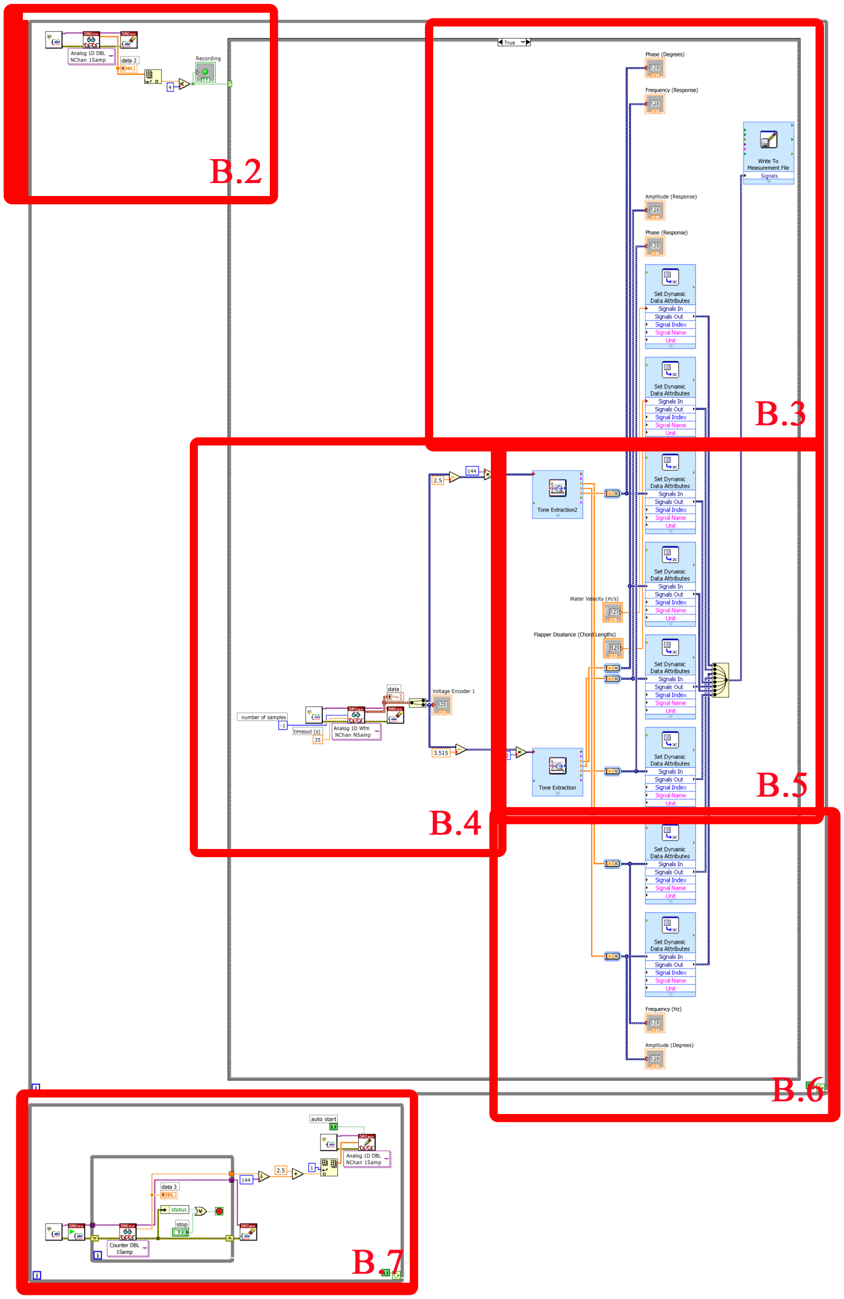

Figure B.1: Block diagram for LabView Virtual Instrument used to acquire encoder data. Detail of the area within each red box is shown in the figure indicated in the bottom right corner of the box.

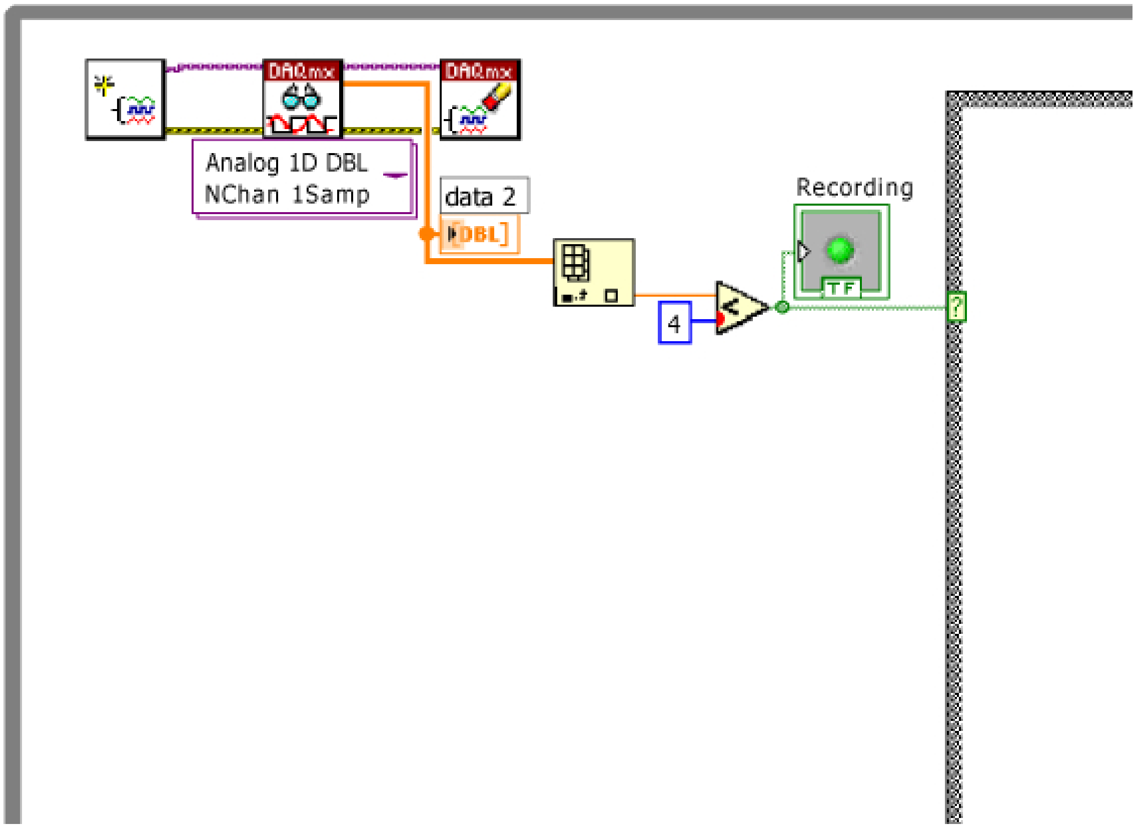

Figure B.2: Detailed view from block diagram in Figure B.1.

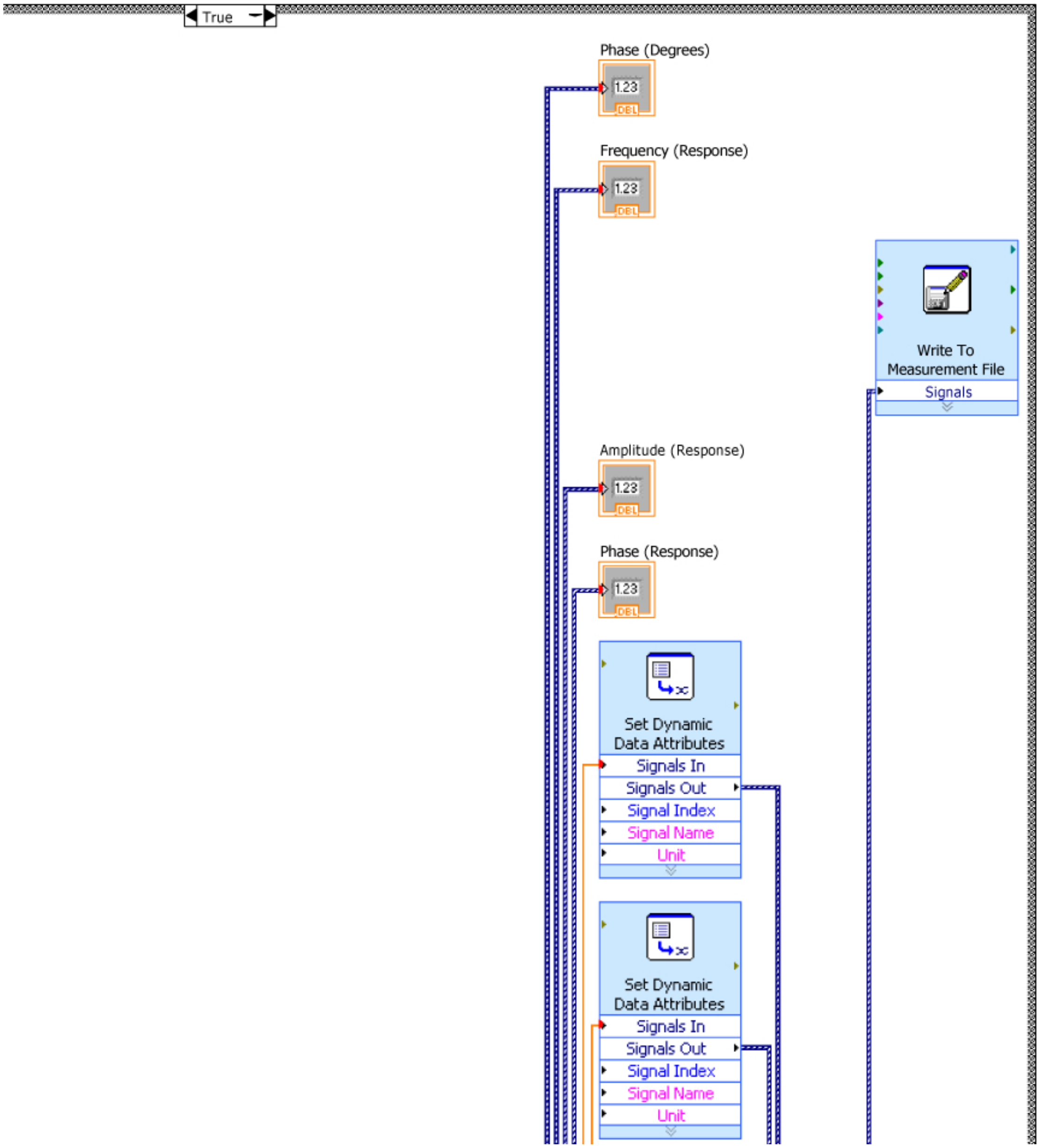

Figure B.3: Detailed view from block diagram in Figure B.1.

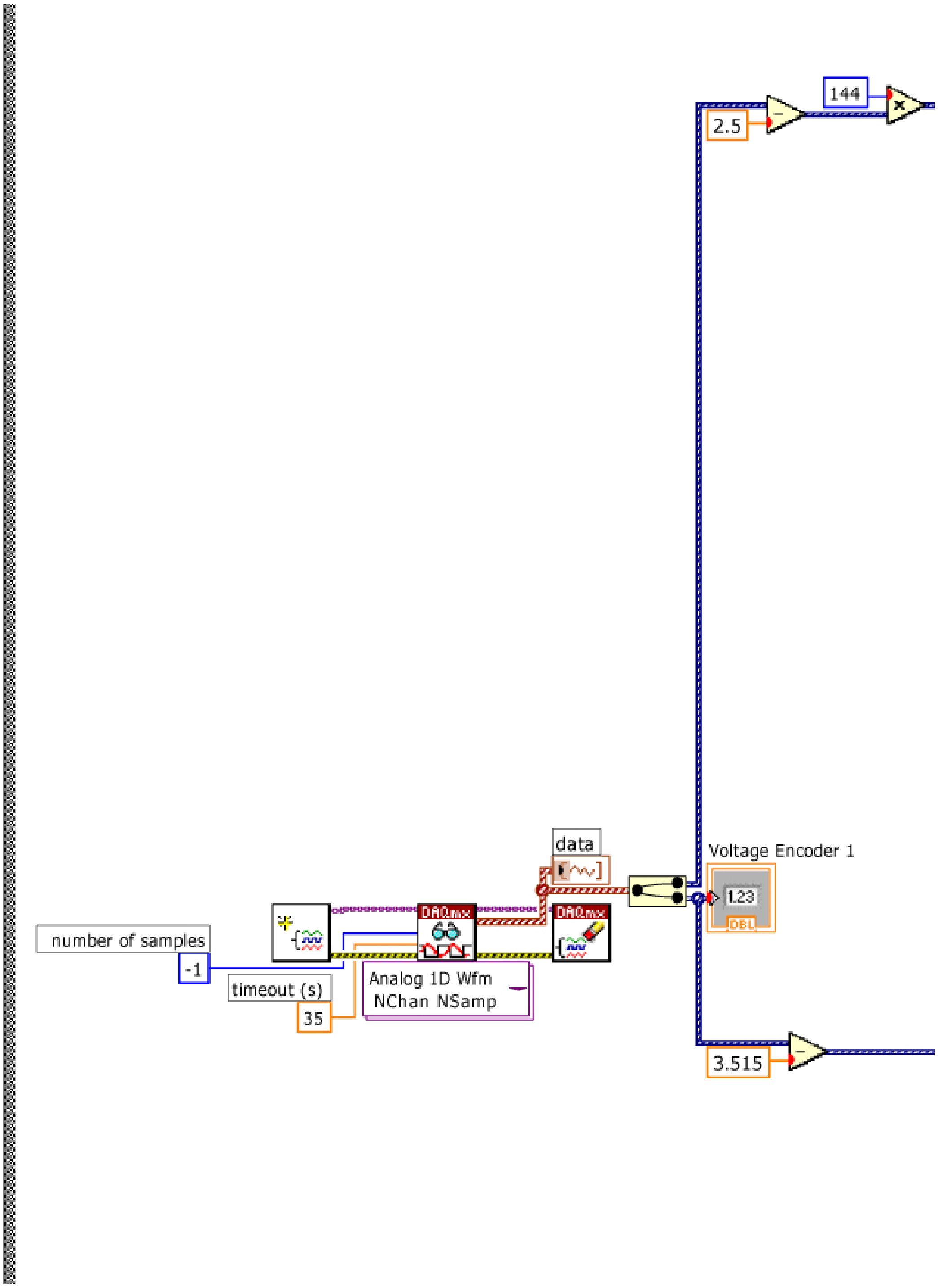

Figure B.4: Detailed view from block diagram in Figure B.1.

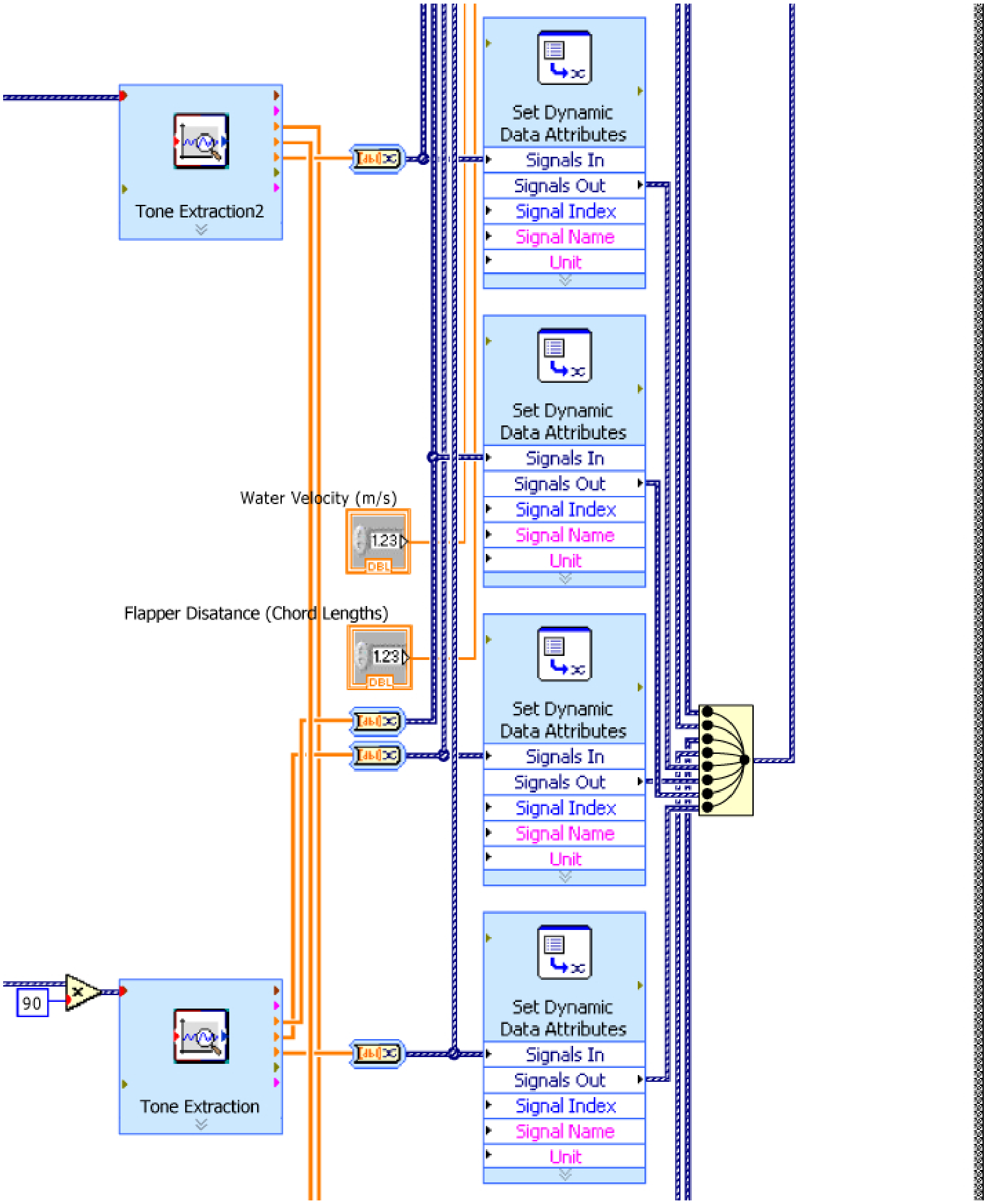

Figure B.5: Detailed view from block diagram in Figure B.1.

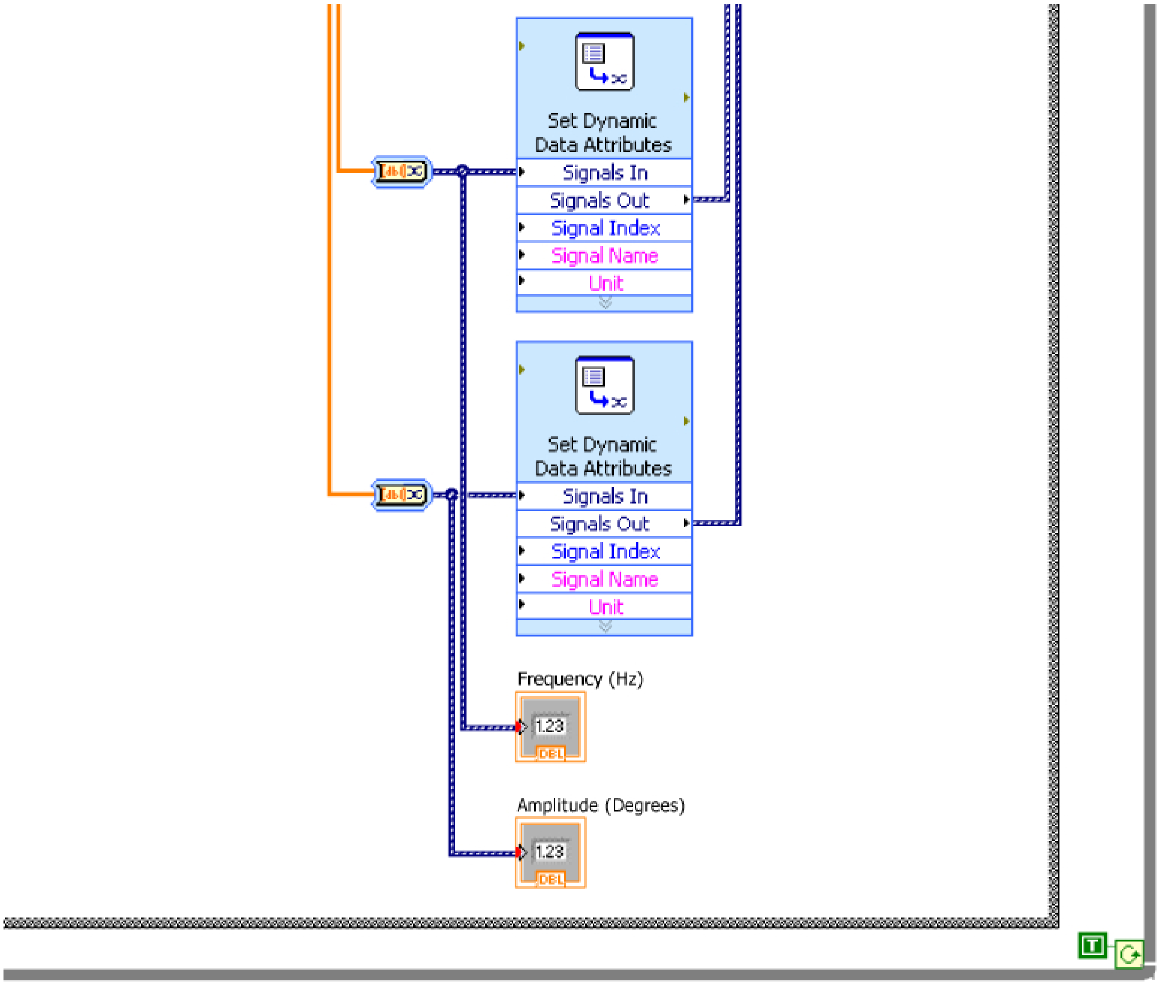

Figure B.6: Detailed view from block diagram in Figure B.1.

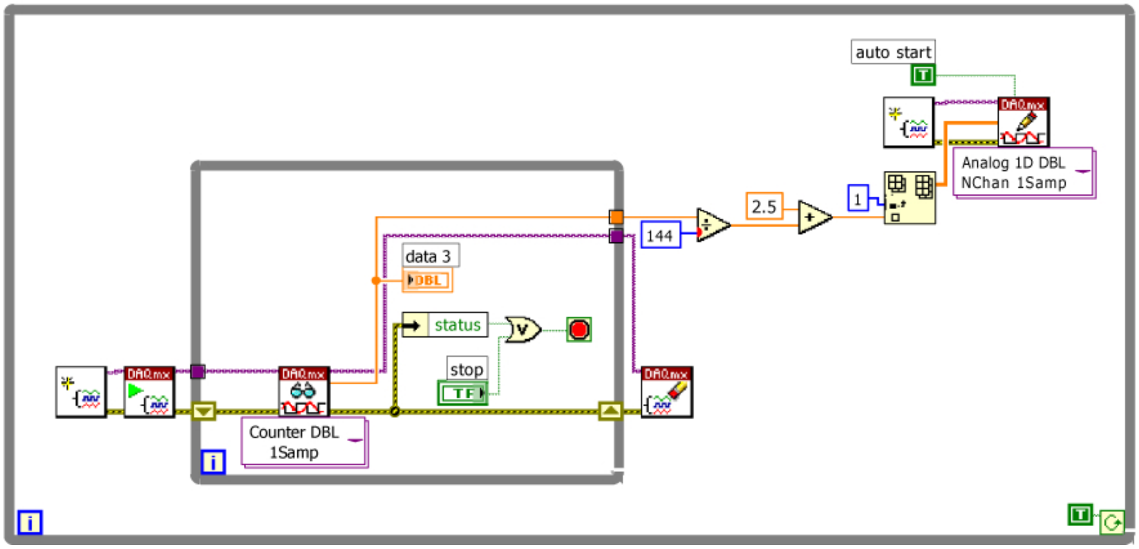

Figure B.7: Detailed view from block diagram in Figure B.1.

B.2 Unwrap Function for Periodic Data

```
function [delshift] = delshift(vel,spacing,freq,phase)
%[f,shift,slope]=delshift(vel,spacing,freq,phase) calculates
%theoretical phase shift at spacing (in chord lengths) for sine wave
%in degrees between 0 and 4 hz and subtract it from measured data
% to get adjusted phase shift. Shift is in degrees. Slope is slope of
% phase line.

h=size(phase)
p=1./freq; %calculates period of wake
t=spacing*0.127/vel; %time for fluid particles (or vortex) to travel
%from tail of front foil to tip of trailing foil
n=t./p; %number of oscillations between foils
periodicshift=-(n-fix(n))*360; %takes remainder of oscillations (after
%integer multiple of complete oscillations) and yields phase
shift=dewrap(periodicshift); %this unwraps the result from a periodic
%sawtooth function to a stright line
for i=1:h
    if isnan(phase(i))==1
        delshift(i)=NaN
    else
        if isnan(phase(1))==1
            delshift1(i)=phase(i)-shift(i);
            delshift(i)=delshift1(i)-delshift1(2);
        else
```

```
            delshift1(i)=phase(i)-shift(i);
            delshift(i)=delshift1(i)-delshift1(1);
        end
    end
end
```

B.3 Frequency Response Function Code

```
%SDOF (or adapt to group of modal systems) Frequency Response Function

wn=input('wn=?')%natural frequency input
%m=input('m=?')%use this and line 8 if wn is not known
k=input('k=?')%stiffness
zeta=input('zeta=?')%damping coefficient
w=linspace(0,2500,10000)%this is frequency range and should contain
%operating range of system
%wn=sqrt(k/m)%natural frequency
r=w./wn


ReFRF=(1/k)*(1-r.^2)/((1-r.^2).^2+(2*zeta.*r).^2);%calculates real
%part of the frequency response function

ImFRF=(1/k)*-(2*zeta*r)/((1-r.^2).^2+(2*zeta.*r).^2);%calculates
%imaginary part of FRF

FRF=sqrt(ReFRF.^2+ImFRF.^2)%yields magnitude of FRF
```

B.4 Frequency Response Function Fitting Code

```
function [frf2] = frffit2(U,spacing,freq,amp,phase)
w=linspace(0,25,1000); %Creates a line space of frequncey values over
%which we will calulate an frf
rw=62.3;%density of water in pounds per cubic foot (units not
%important since ratio of densities is used
ra=167;%density of aluminum in pounds per cubic foot
c=5*.0254; %Chord length in meters
d=0.5*.0254; %Foil width in meters
s=10*0.0254; %Foil span in meters
a=freq;
q2=amp;
```

```
fd=0.2;%damped natural frequency in hertz
wd=fd*2*pi; %damped natural frequency in radians per second
C=3/20 %Constant scalar for spring
k=C*s*rw*U^2; %Spring coeefecient
m=ra*c*s*d;
wn=sqrt(k/m);%undamped natural frequency in radians per second
fn=wn/(2*pi);%undamped natural frequency in hertz
H=2/3;%Zeta coefficient
zeta=sqrt(1-wd^2/wn^2)
%zeta=0
%subplot(2,1,1)

r=w./wn;

frf1=(1/k)./((1-r.^2)+1i*(2*H*zeta*r));
Factor=max(q2)/max(abs(frf1))
frf2=Factor*frf1;%here, q2 is amp ratio (sin(a)/sin(b)) to be fitted
phi=atan2(imag(frf2),real(frf2))*180/pi;
subplot(3,1,1);
plot(w./(2*pi),abs(frf2),'--',a,q2,'ok');
p=delshift(U,spacing,freq,phase);
subplot(3,1,2)
plot(w./(2*pi),phi,'--',freq,p,'ok')
subplot(3,1,3)
plot3(w./(2*pi),real(frf2),imag(frf2));
hold
plot3(a,re1,im1);
 %plot(w./(2*pi),imag(frf2));
```